Physics of the Liquid and Supercritical States of Matter

Cillian Cockrell
Project Supervisor: Professor Kostya Trachenko

Submitted in partial fulfillment of the requirements of the Degree of Doctor of Philosophy

December 7, 2021
School of Physics and Astronomy
Queen Mary, University of London

Statement of Originality

I, Cillian Cockrell, confirm that the research included within this thesis is my own work or that where it has been carried out in collaboration with, or supported by others, that this is duly acknowledged below and my contribution indicated. Previously published material is also acknowledged below.

I attest that I have exercised reasonable care to ensure that the work is original, and does not to the best of my knowledge break any UK law, infringe any third party's copyright or other Intellectual Property Right, or contain any confidential material.

I accept that the College has the right to use plagiarism detection software to check the electronic version of the thesis.

I confirm that this thesis has not been previously submitted for the award of a degree by this or any other university.

The copyright of this thesis rests with the author and no quotation from it or information derived from it may be published without the prior written consent of the author.

Cillian Cockrell
01/10/2021

Details of Collaboration and Publication

- Chapter 4 - C. Cockrell, O. A. Dicks, V. V. Brazhkin, and K. Trachenko, *J. Phys.: Condens. Matter* **32**, 382103 (2020).
- Chapter 5 - C. Cockrell, O. A. Dicks, L. Wang, K. Trachenko, A. K. Soper, V. V. Brazhkin, S. Marinakis *Phys. Rev. E* **101**, 052109 (2020).
- Chapter 6 - C. Cockrell *Phys. Rev. E* **102**, 062206 (2020).
- Chapter 7 - C. Cockrell, V. V. Brazhkin, and K. Trachenko *Phys. Rev. E* **104**, 034108 (2021).

Abstract

The liquid and supercritical states of matter are respectively the least understood and most misunderstood states of ordinary matter, from a theoretical view. The work exposited in this thesis aims to elucidate the nature of the supercritical state and its relationship to the liquid and gas states which flank it on the phase diagram. Contrary to the belief of the supercritical state as lacking transitions, these works present several transitions to be found in this state. This is done with molecular dynamics simulations data.

We begin with structural crossovers discovered in the two most important supercritical fluids from an industrial point of view: water and carbon dioxide. These crossovers coincide with calculations of the dynamical crossover called the Frenkel line, which marks termination of oscillatory molecular motion, giving way to purely diffusive motion. These structural crossovers across the Frenkel line demonstrate the universal applicability of the Frenkel picture of fluids.

I then perform simulations of argon to calculate the dynamical instability of its supercritical state. Using tools from chaos theory, I show that the dynamical instability undergoes a crossover at the Frenkel line, which demonstrates that the supercritical state sports a transition in the fundamental geometry of phase space.

The “c”-transition is presented next. This is a universal interrelation between the dynamics and thermodynamics across the supercritical state and a transition which provides an unambiguous separation of liquidlike and gaslike states in several different supercritical fluids. This discovery was completely unanticipated and is like nothing else ever seen in the supercritical state.

The “c”-transition is suggestive of a phase transition, and the thesis concludes with the beginnings of a search for it. The heat capacity is calculated from molecular dynamics simulations of argon with unprecedented precision, and other methods used to find a phase transition are discussed.

Contents

1 Introduction **11**
- 1.1 The Third State of Matter . . . 11
- 1.2 How Does a Liquid Differ from a Gas? . . . 11
- 1.3 The Supercritical State . . . 13
- 1.4 Thesis Outline . . . 15

2 Theory **18**
- 2.1 Mori-Zwanzig Theory . . . 18
  - 2.1.1 The Generalised Langevin Equation . . . 18
  - 2.1.2 The Memory Function . . . 24
  - 2.1.3 Generalised Hydrodynamics . . . 26
- 2.2 Frenkel Theory . . . 36
  - 2.2.1 The Problem of c_V . . . 36
  - 2.2.2 The Frenkel line and the Supercritical State . . . 40

3 Molecular Dynamics **44**
- 3.1 Integration Algorithms . . . 44
- 3.2 Potentials . . . 45
- 3.3 Gathering Data . . . 48

4 Water **55**
- 4.1 The Most Studied Compound in Science . . . 55
- 4.2 Molecular Dynamics Simulations . . . 56
- 4.3 Results . . . 59
- 4.4 Discussion . . . 66

5 Carbon Dioxide **70**
- 5.1 A Very Versatile Fluid . . . 70
- 5.2 Molecular Dynamics Simulations . . . 71
- 5.3 Results . . . 71
- 5.4 Discussion . . . 79

6 Chaos **83**
- 6.1 Dynamical Instability . . . 83
- 6.2 Molecular Dynamics Simulations . . . 86

6.3 Results . . . 88
6.4 Discussion . . . 91

7 The “c”-transition **98**
7.1 The Nature of the Frenkel Line . . . 98
7.2 Molecular Dynamics Simulations - Argon . . . 99
7.3 Molecular Dynamics Simulations - Carbon Dioxide . . . 110
7.4 Discussion . . . 113

8 The Possibility of a Phase Transition **118**
8.1 What is the nature of the “c”-transition? . . . 118
8.2 Precision Measurements of c_V from Molecular Dynamics Simulations . . . 118
8.3 Derivatives of c_V . . . 124

9 Beyond Super and Subcritical **128**
9.1 Conclusions . . . 128
9.2 Further Work . . . 130

List of Figures

1.1 Isotherms of the van der Waals equation of state, showing the famous “van der Waals loop” which signifies the vapour-liquid phase transition. 13

1.2 The phase diagram of matter in the high-temperature and high-pressure range. The boiling line terminates at the critical point, out of which the Widom line and related lines emerge, representing near-critical anomalies of different thermodynamic quantities. The Frenkel line terminates at the boiling line but extends arbitrarily far into the supercritical state, separating rigid liquid-like and nonrigid gaslike fluids. 14

2.1 The transverse current spectrum $C^{\mathrm{T}}(\omega, k)$ at an arbitrary wavevector, showing non-propagating modes for $\tau^{\mathrm{T}}(k) = \frac{1}{2}$ and propagating modes for $\tau^{\mathrm{T}}(k) = 1$, distinguishable by the clear peak at around $\omega = 0.8$. . . . 33

4.1 (a) Phase diagram of H_2O showing the Frenkel line (reproduced from [72]), together with experimental state points of Katayama [67], Soper [68], and Gorbaty [73] and state points used in molecular dynamics simulations in this work. The Widom line is reproduced from the data of Ref. [57]; (b) Density versus temperature plots for the simulated samples in this study. The Frenkel line (indicated by dotted lines) passes through regions of high density beneath the density fluctuations at the Widom line. 57

4.2 (a)-(c): O-O RDFs of simulated water at different pressures and temperatures. Insets are the same data but with reduced plotting range to highlight the secondary peaks. (d) Simulated and experimental [68] RDFs at ambient and supercritical conditions, offset by 1 for convenience. . . . 60

4.3 (a)-(b): O-O PDFs of simulated water at higher pressures. 61

4.4 O-O RDF peak positions: Squares - second peaks; circles - third peak; triangles - new second peaks. Open triangles imply that the new peak is less prominent than the old peaks, and vice versa for open squares and circles. The dashed vertical lines correspond to temperatures at the Frenkel line. 62

4.5 (a): Mean coordination number n_{c} of water molecules in the supercritical state across Frenkel line. The dashed verticle lines correspond to the temperature at the Frenkel line. n_{c} is not shown at low temperature at 5 kbar because the minimum between the first and second peaks in Fig. 4.2c disappears at those temperatures, causing an ill-defined cut-off. (b): Normalised histogram of molecular coordination calculated from structural snapshots at 1 kbar. (c): Intermolecular angular distribution functions at 1 kbar. The dashed curve shows the distribution at the temperature corresponding to the Frenkel line. 63
4.6 Log–log plot of the RDF first peak heights, showing the crossover of evolution as temperature approaches the FL. The dashed lines correspond to the temperatures at the FL 65
4.7 O-O PDF peak positions from molecular dynamics (MD) data and X-ray scattering data [73]. As before, open triangles imply that the new peak in the MD data is less prominent than its neighbours and vice versa for open squares and circles. 68

5.1 The phase diagram carbon dioxide, showing the Frenkel line with reference to the boiling line and melting line. The star represents the critical point. 71
5.2 Evolution of C-C RDFs of simulated carbon dioxide at different pressures and temperatures. 72
5.3 Evolution of the first peak position of the C-C RDFs with temperature. The dotted lines correspond to the temperatures at the FL. 74
5.4 Evolution of the first peak position of the C-C RDFs with temperature from the second batch of simulations with greater precision. The dotted lines correspond to the temperatures at the FL. 75
5.5 Evolution of the first peak height of the C-C RDFs with temperature. The dotted lines correspond to the temperatures at the FL. 76
5.6 Relationship between the first peak position r and the system's characteristic length $V^{\frac{1}{3}}$. Dashed vertical lines show the fitted crossover volume and the volume at the FL. Insets: Relative trend of the residuals of the linear fit 78
5.7 First peak position $k_{\max}$ of the structure factor $S(k)$ of supercritical CO_2, extracted from neutron scattering experiments [74], as a function of temperature T at (a) 500 bar; (b) 590 bar. 80
5.8 First peak positions of the experimental weighted sum PDF for CO2 at (a) 500 bar and (b) 590 bar as a function of the volume. The liquidlike and gaslike regions meet at the modelling prediction of the FL at (a) 297 K; (b) 303 K. 82

6.1 The evolution of a probability density under chaotic dynamics in a (a)-(b): fine grained phase space; (c)-(d): coarse grained phase space. 84
6.2 The phase diagram argon, showing the Frenkel line with reference to the boiling line and melting line. The star represents the critical point. . . . 87

6.3 Reduced energy per particle $\frac{E^*}{N}$ across the melting line at reduced concentrations of (a) 0.8284 and (b) 1.065. 89

6.4 Maximal Lyapunov exponent Λ across the melting line at reduced concentrations of (a) 0.8284 and (b) 1.065. 90

6.5 Velocity autocorrelation functions as a function of reduced energy per atom and reduced time $Z(t^*)$ at the four different concentrations. 92

6.6 Maximal Lyapunov exponent Λ in the fluid state at reduced concentrations of (a) 0.7107; (b) 0.8284; (c) 1.056. The red lines are fitted power-law relationships $\Lambda = a(E^*)^b$. The fitted values are reported in Tab. 6.4. The energy scale in (c) is curtailed in order for the resolution to allow the deviation from the power law at low energies to be visible. 93

6.7 Summary of our main results: Evolution of dynamical instability in condensed matter, from solids at low temperature to gaslike supercritical fluids at high temperature. The figure shows the dynamical regimes in each state of matter (oscillation, diffusion, collisions) and their relationship to the dynamical instability. Yellow atoms are oscillating, green atoms are diffusing, and cyan atoms are colliding. 96

7.1 Comparison of (a) viscosities η and (b) isochoric specifc heat capacities c_V ($k_\mathrm{B} = 1$) calculated from simulated trajectories with experimental data from NIST [97]; comparison of viscosities η calculated from simulated trajectories along the (c) 10 kbar isobar and (d) 500 K isotherm, with experimental data from Abramson [125]. 102

7.2 Specific heat c_v ($k_\mathrm{B} = 1$) as a function of viscosity η, calculated along three (a) isobars; (b) isotherms; (c) isochores. 103

7.3 Liquid relaxation time τ of molecular dynamics trajectories along three (a) isobars; (b) isotherms; (c) isochores. 105

7.4 Specific heat c_V ($k_\mathrm{B} = 1$) as a function of relaxation time τ, calculated along three (a) isobars ; (b) isotherms; (c) isochores. The solid lines in (c) represent the approach of c_V and τ to their limiting ideal-gas value $c_V = 3/2$ at large temperature and are meant as guides for the eye. . . . 106

7.5 Simulated c_V ($k_\mathrm{B} = 1$) of argon as a function of the dynamical length, $\lambda_\mathrm{d} = c\tau$ across 9 paths spanning the supercritical state up to 330 T_c and 8000 P_c. All these paths collapse onto a single curve and undergo a unified dynamic-thermodynamic transition at the path-independent point $c_V = 1.88$ and $\lambda_\mathrm{d} = 1$ Å 107

7.6 c_V as a function of $c^\mathrm{T}\tau_\mathrm{M}k_\mathrm{D}$ ($k_\mathrm{B} = 1$), where the curves similarly converge in the liquidlike state at the path-independent point close to $c_V = 2$. . . . 109

7.7 Simulated c_V ($k_\mathrm{B} = 1$) of carbon dioxide as a function of the dynamical length, $\lambda_\mathrm{d} = c\tau$ across 5 paths spanning the supercritical state up to 33 T_c and 520 P_c. All these paths collapse onto a single curve and undergo a unified dynamic-thermodynamic transition at the path-independent point $c_V = 2.9$ and $\lambda_\mathrm{d} = 1$Å 112

7.8 (a): Comparison of a near critical isotherm (500 K) in carbon dioxide to the main sequence "c"-transition curve from deeply supercritical state points. (b) Comparison of a near critical isobar and a subcritical isobar in argon to the main sequence. In both figures, the near-critical paths are split according to whether volume is above or below the volume of the critical isochore, V_c. 114
7.9 Phase diagram of argon showing the inversion points of the "c"-transition corresponding to $c_V \approx 1.9k_\mathrm{B}$ in Fig. 7.5, the Frenkel line determined by the VAF criterion [23], the critical point, and the critical isochore. 115

8.1 Standard deviation $\sigma(c_V)$ of the heat capacity calculated, at each temperature along the unit isochore in Lennard-Jones units (1.688 g/ml), using 20 4-million-timestep trajectories ($k_\mathrm{B} = 1$). 121
8.2 Heat capacity c_V calculated along the unit isochore in Lennard-Jones units, using 20 4-million-timestep trajectories ($k_\mathrm{B} = 1$). The gridlines are separated by $0.005k_\mathrm{B}$. 122
8.3 Heat capacity c_V calculated along a section of the unit isochore in Lennard-Jones units, using 20 4-million-timestep trajectories ($k_\mathrm{B} = 1$). The gridlines are separated by $0.001k_\mathrm{B}$. 123
8.4 Heat capacity c_V calculated along the 1.35 g ml^{-1} isochore in the NVT thermostat with a friction constant of $1ps$, using 40 36-million-timestep trajectories ($k_\mathrm{B} = 1$). The gridlines are separated by $0.005k_\mathrm{B}$. 126
8.5 Derivative of the heat capacity $\frac{\partial c_V}{\partial T}$ calculated along the 1.35 g ml^{-1} isochore in the NVT thermostat with a friction constant of $1ps$, using 40 36-million-timestep trajectories ($k_\mathrm{B} = 1$). 127

List of Tables

3.1 Potential parameters used in molecular dynamics simulations of water. ϵ_{OO} and σ_{OO} refer to the Lennard-Jones parameters between the oxygen atoms, as per Eq. 3.2.4. 48
3.2 Potential parameters used in molecular dynamics simulations of carbon dioxide. A_{CO} refers to the Buckingham parameter between the carbon and oxygen atoms, as per Eq. 3.2.6, and so on for A_{CC}, ρ_{CO} and so on. . 49
3.3 Potential parameters for argon used in the molecular dynamics simulations. 49

6.1 Lyapunov times of different dynamical systems [101]. 86
6.2 Definitions of the dimensionless reduced units in the LJ potential. 86
6.3 Thermodynamic data for each system investigated: ρ - density; n concentration; T_{F} - temperature at the Frenkel line; T^*_{F} reduced temperature at the Frenkel line; E_{F}/N - energy per particle at the Frenkel line; E^*_{F}/N - reduced energy per particle at the Frenkel line. The reference energy is $E^*/N = 0$ at $n^* = 0.5917$ and $T^* = 0.5$ (20 K). 88
6.4 Fitted parameters for the power law relationship $\Lambda = a(E^*)^b$ along the three different isochores. 91

Chapter 1

Introduction

1.1 The Third State of Matter

The liquid state is an interesting curiosity, academically speaking. Condensed matter and statistical physics modules for undergraduates and even postgraduates have plenty to say on the gaseous and particularly the solid states, but the liquid state is barely mentioned, save for demonstratively when perhaps discussing the Clausius-Clapeyron equation. In my experience, many physicists in other fields do not even realise their own ignorance of the liquid state, it never having been brought up in their education before they specialise away from condensed matter. One recalls the poignant story by Andrew Granato about his time teaching statistical mechanics at the University of Illinois. He "lived in constant fear that some student might raise his hand and ask: 'How about liquids?'", but also notes that this never once happened across cohorts totalling 10000 students [1]. This anecdote is in line with my own undergraduate experiences, and it is no secret that textbooks on statistical mechanics and even those dedicated to liquids do not have much, or anything, to say at all on the topic of heat capacity in liquids [2, 3, 4, 5, 6, 7, 8, 9].

It is not hard to see why liquids have a pessimistic outlook associated with them. As they saying goes, they have no "small parameter". What is meant by this is that perturbative approaches are unacceptable for the study of liquids. In gases, one can treat the potential energy perturbatively, starting from an ideal gas and expanding in pairs and triplets and so on of particles interacting [6]. On the other hand, in solids, we can rely on atoms having permanent, or at least nearly permanent positions, and can expand each particle's potential energy in harmonic and then anharmonic terms. Liquids are dense, like solids, and they flow, like gases, so they are strongly interracting and their particles do not have equilibrium positions. Neither the interaction nor the displacement is small. This is what is meant by a lack of a "small parameter".

1.2 How Does a Liquid Differ from a Gas?

A coherent notion of the gaseous state is a relatively recent development in physics and chemistry. Antoine Lavoisier was the first to suggest that all gases can be condensed into liquids [10]. In Lavoisier's time vapours were distinct from gases, also called *elastic fluids*, with the former resulting from the evaporation of a liquid and the latter being a distinct state of matter (to which the caloric and aether fluids also belonged). Experiments by Lavoisier, Michael Faraday and Humphry Davy [11, 12], and others in which gases were liquefied showed that gases (caloric, aether, and the electric fluid notwithstanding) are vapours and are therefore states of ordinary matter rather than a different type altogether.

On the theoretical front, the liquid state was a mystery for a long time in part due to the success of theoretical physics to understand the gaseous state. Liquids are apparently much more similar to gases than they are to solids. One of the great achievements of theoretical physics is the Navier Stokes equations to which liquids and gases are both admissible as "fluids". Combining this with the ability of statistical mechanics to recover the thermodynamics of ideal gases, it is clear why the perturbative, "dense gas" treatment of liquids would be attractive to theoretical physicists. The most prominent example of this is the van der Waals ideal fluid, for which Johannes van der Waals won the 1910 Nobel Prize in Physics. This model adds attractive and repulsive interactions to the ideal gas at low order in density. The equation of state of the van der Waals ideal fluid is:

$$\left(P + \frac{aN^2}{V^2}\right)(V - Nb) = Nk_{\mathrm{B}}T, \tag{1.2.1}$$

with N the number of molecules, P the pressure, V the volume, T the temperature, k_{B} the Boltzmann constant, and with a parametrising the attractive forces between molecules and b parametrising the molecules' "size" (such that the volume can never fall below Nb). The addition of the attractive term, indeed the simplest possible way of representing that each molecule is attracted to each other molecule, gives the isotherms of Eq. 1.2.1 interesting behaviour. This can be seen in the low temperature isotherms in Fig. 1.1: after reducing the volume to a certain point, the pressure *decreases* for a while, before increasing again, far more sharply. This region of thermodynamic instability is taken to represent a phase transition, and the high and low volume regions the vapor and liquid phases respectively. The critical isotherm, at $T \approx 0.5$ is also shown in Fig. 1.1, at and above which there is no "loop", therefore terminating the boiling line.

The van der Waals state has a lot going for it. It can be derived using classical statistical mechanics using cluster expansions [6]. These methods suffer from a rather glaring issue, however. The liquid heat capacity is rather high, much closer to that of a solid than a gas. Indeed, a monoatomic liquid close to its melting point has a isochoric specific heat capacity c_V very similar to that of the Dulong and Petit value for solids: $3k_{\mathrm{B}}$. Meanwhile the isochoric heat capacity of the van der Waals fluid is the same as the ideal gas: $\frac{3}{2}k_{\mathrm{B}}$. While the addition of these attractive terms is sufficient for the existence of a phase transition, this cannot correspond to the liquid-vapour transition due to the vast difference in heat capacity between the high-density state of the model and real liquids. The van der Waals model, and other similar models, serve as conceptual guides to the liquid and supercritical states, but they miss key aspects to the liquid state. We must look elsewhere.

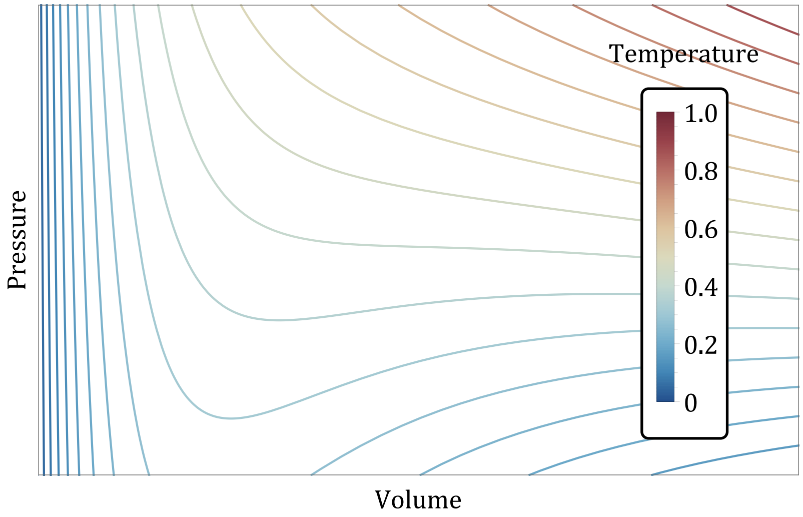

Figure 1.1: Isotherms of the van der Waals equation of state, showing the famous "van der Waals loop" which signifies the vapour-liquid phase transition.

1.3 The Supercritical State

This theoretical basis for the supercritical state, the termination of the boiling line, was a strong argument for the validity of the van der Waals model. The critical point and supercritical state was discovered by Charles Cagniard de la Tour in his experiments on acoustics [13, 14] by heating liquid-vapour mixes to the point where there is no distinction between them. Our view of this *état particulier*, now called the supercritical state (a name given to it by Thomas Andrews, who elucidated much of its nature [15]), has not changed in the 200 years since its discovery. Near critical anomalies behave like extensions to the boiling line, but do not persist deep into the supercritical state which is otherwise seen as homogeneous, unremarkable and lacking in transitions [7, 16, 17]. A phase diagram showing the relationship between the boiling line, melting line, and to-be-introduced "Frenkel line" is shown in Fig. 1.2.

Naturally, there have been several proposals which extend a separation between "liquidlike" and "gaslike" states beyond the critical point, though not far beyond it. For example, maxima of density fluctuations exist in many supercritical fluids in the vicinity of the critical point [18, 19, 20, 21]. The Widom line is the most famous stratification of the supercritical state. It is the line of the maximum of the isobaric heat capacity which extends from the critical point and becomes less prominent as it departs [22]. Similar maxima lines for isothermal compressibility, thermal expansion *etc.* can be defined, which are all close to each other, all emerge from the critical point, and all disappear beyond its vicinity at around two to three times the critical temperature. The Widom line is a very evocative phenomenon - it emerges from the critical point and carries on the legacy of thermodynamic anomalies at the boiling line. It is interesting that these anomalous lines diverge from each other as they go deeper into the supercritical state. This near-critical state with its anomalous properties is like an expansion of the boiling line into a whole region. The anomalies give many supercritical fluids important and

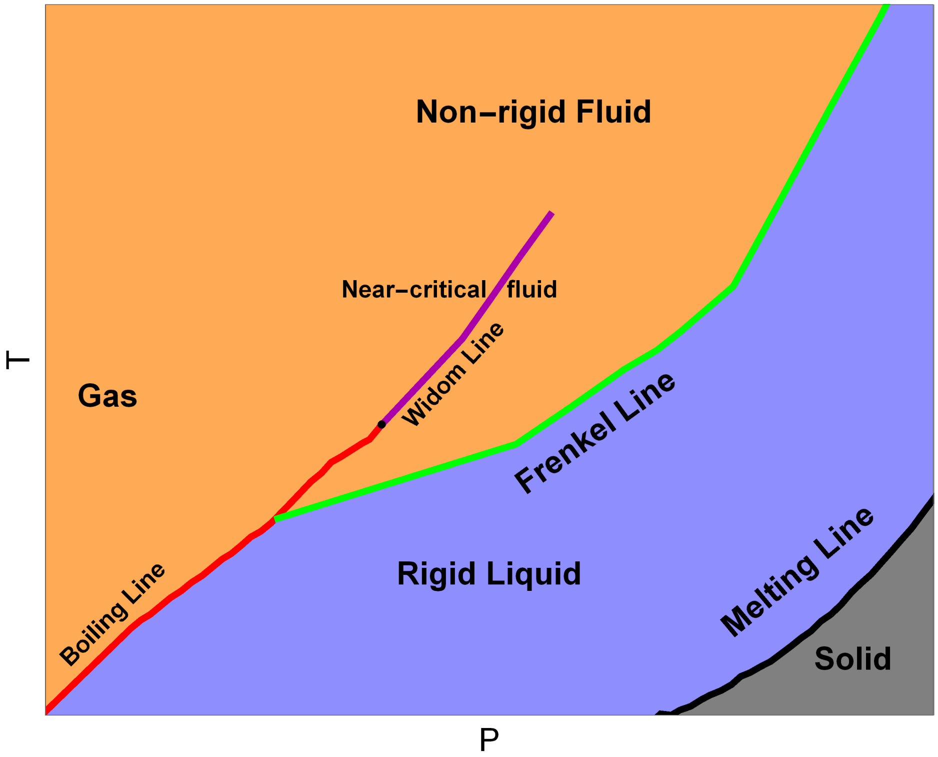
Non−rigid Fluid
Near−critical fluid
Widom Line
Gas
Frenkel Line
Boiling Line
Rigid Liquid
Melting Line
Solid
T
P

Figure 1.2: The phase diagram of matter in the high-temperature and high-pressure range. The boiling line terminates at the critical point, out of which the Widom line and related lines emerge, representing near-critical anomalies of different thermodynamic quantities. The Frenkel line terminates at the boiling line but extends arbitrarily far into the supercritical state, separating rigid liquid-like and nonrigid gaslike fluids.

exploitable properties.

More recently and about ten years ago, the Frenkel line was introduced [23, 24, 25] as a dynamical crossover line in the supercritical state. This crossover is defined on the basis of particle dynamics in fluid states. The key physical distinction between liquids and gases is the qualitative difference between the types of atomic trajectories. In gases, particles move in straight lines between the collisions after which they change course. In liquids, atomic motion consists of two types: quasi-harmonic vibration around equilibrium positions and diffusive jumps between two neighbouring equilibrium positions [2]. Therefore, atomic motion in a liquid combines both elements of small-amplitude vibrations as in a solid and diffusive motion as in a gas. On temperature increase (or pressure decrease), a particle spends less time vibrating and more time diffusing. The (P,T) conditions at which the solid-like oscillating component of motion disappears, leaving only the diffusive motion, correspond to the qualitative change of particle dynamics and to the transition of the liquidlike into the gaslike state [23, 24, 25]. This crossover in dynamics, from combined oscillation and diffusion to pure diffusion, is the theoretical definition of the Frenkel line.

Supercritical fluids are employed in a variety of industrial applications [17, 26, 27, 28, 29] such as chemical extraction, chemical reactions, as solvents, and many many more. The keen extracting and dissolving efficiency of supercritical fluids is due to a combination of factors. Supercritical fluids at high pressures possess high densities, much closer to those of subcritical liquids than gases, but at the same time possess very diffusive motion, sporting diffusion coefficients which are 10-100 times higher than those of of subcritical liquids. The high density promotes interaction between a solute and solvent, and the high diffusion promotes dissolution itself and helps maintain a high reaction rate. In this sense, supercritical fluids combine the best of both worlds.

Despite the extensive industrial use of supercritical fluids, it is well known that their understanding from a fundamental perspective is lacking [17, 26, 27]. Empirical results instead form the basis of the application of supercritical fluids in industrial sectors. The elucidations to the supercritical state such as the Widom line, and the Frenkel line are therefore important for improving fundamental understand of the supercritical state and optimising the use of it in industrial applications [17, 30, 31, 32, 33, 34]. The supercritical state is subject to much the same neglectful treatment as the liquid state in undergraduate physics courses. One is given the famous example of continuously transforming a liquid into a gas or vice versa by taking a path on the phase diagram around the critical point, but little is said about the state itself except that it has “properties intermediate to liquids and gases” and that “no distinctive states can be found” within it.

1.4 Thesis Outline

This project was outlined with one particular goal in mind - to understand the nature of the transition of the Frenkel line. The Frenkel line and the supercritical state has been the sole focus of all the major projects I undertook during this PhD (which are the only ones I describe here). This was to be done by a combination of theory and molecular dynamics simulation, as is the norm for the field of liquid physics.

I begin in Chapter 2, as is right, with Mori-Zwanzig theory, which uses the powerful tool of timescale separation to fully convert a macroscopic description of fluids into a microscopic picture. This will allow us to come up with expression for fluid relaxation properties, namely the viscosity, in terms of microscopic quantities, as well as elucidate the nature of collective modes in the fluid state. This project is all about dynamics and thermodynamics of supercritical fluid, so this formal understanding of collective modes is central to what follows. We then approach the liquid state from a less formal and more goal-oriented point of view - Frenkel theory. Along with providing an unparalleled general explanation for liquid heat capacities, it gives rise to the Frenkel line, the dynamical stratification of the supercritical state which will dominate this thesis.

Having gone to great lengths to understand what fluid states are, microscopically, we then put this work to the test in Chapter 3 by introducing molecular dynamics, our window into the microscopic world. I describe the algorithms used to integrate classical equations of motion, how we model systems, and how the resulting trajectories are used to gather results useful for statistical mechanical analysis.

In Chapter 4 I describe the rather surprising results of the first molecular dynamics project I performed, which was on water. Here we will see the coupling of the Frenkel line to water's striking structural crossover from tetrahedral ordering to disordered close packing, on the basis of molecular coordination statistics. Water's tetrahedral structure, and its loss of that structure in the supercritical state and surrounding topics are subject to much debate. The coincidence of this important transition, and the elucidation of how the different states on either side of it evolve, with the FL, a theory and framework developed entirely independently of water, is a strong vindication for the theory.

Following this, in Chapter 5, we see the results of the second project, this time on the other giant of the supercritical fluids industry - carbon dioxide. In collaboration with neutron scattering experiments, I analyse the relationship between density and intermolecular distances to show a crossover in structural evolution across the Frenkel line. This result is less dramatic than the result found in water, and high quality methods and moderate statistical analysis were required to decisively confirm the result.

In Chapter 6 I change tune slightly and use methods from chaos theory to find new insights into the Frenkel line. I calculate a characteristic measurement of a chaotic system, the maximal Lyapunov exponent, along several deeply supercritical isochores which cross the Frenkel line. A very crisp crossover is observed, which I explain in terms of the different dynamical "events" occurring in the different states and their contribution to chaotic dynamics. These dynamical events are exactly the phenomena used in Frenkel theory, and this work therefore not only extends a study of chaos theory into the supercritical state, but also reveals that the Frenkel picture of fluids is relevant to the study of the properties of phase space itself.

Chapter 7 is a change of timbre, and the *magnum opus* of this PhD. Instead of looking at the consequences of the Frenkel line, we inspect the transition itself. Searching for a way to unambiguously measure the dynamical timescales of a supercritical fluid, I discovered a very special relationship between the "dynamical length" of a system, describing the maximum wavelength of propagating transverse modes below the Frenkel line, and the isochoric specific heat capacity. This relationship is universal, occuring along all supercritical paths except those that pass through near-critical anomalies, and serves as an unambiguous separation between liquidlike and gaslike states, unlike the previous vague or path-dependent definitions of the Frenkel line. This transition between liquidlike and gaslike states is called the “c”-transition, due to the “c”-shaped curve which parametrises the dependence of the heat capacity on the dynamical length, and has been observed in molecular dynamics simulations of argon, nitrogen, and carbon dioxide. The “c”-transition is unprecedented and, I believe, will open a new avenue of research into the supercritical state entirely. This transition is little understood, and its scope and implications are only briefly discussed in this chapter.

The discovering of the “c”-transition introduced many questions, the first of which I attempted to begin answering in Chapter 8, the possibility of a thermodynamic phase transition coupled to the “c”-transition. This was always a possibility considered at the Frenkel line, but the “c”-transition is very suggestive as a path-independent transition with a distinctive inversion point. The precision of my molecular dynamics simulations had to be greatly improved, and this allows me to place an upper limit of around 0.002 k_{B} on the size of a possible discontinuity in heat capacity across the Frenkel line and “c”-transition. A higher order transition would require precision measurements of the derivative of the heat capacity, which would need to be calculated analytically rather than numerically. This venture is started, but the work is ongoing.

Finally in Chapter 9, I draw conclusions of the results holistically and discuss my plans for further work, mostly involving the “c”-transition, much of which is already underway. We’ve been hunting this beast for a long time, and we seem to be closing in. I have no intention of giving up the chase.

Chapter 2

Theory

2.1 Mori-Zwanzig Theory

The power of thermodynamics and the related hydrodynamics is the selection of a few special variables whose evolution is self-contained, despite the microscopic truth of the world. The miracle of entropy and heat is how simply it describes all of these ignored degrees of freedom (I must stop myself here lest I write another 100 pages on entropy and uncertainty). Our starting point is with the Mori-Zwanzig formalism. Pre-requisites of irreversible thermodynamics, advanced classical statistical mechanics, correlation functions, and micoscropic representations of hydrodynamics quantities can be found in several introductory postgraduate texts, *e.g.* Refs [6, 8, 35]. With these microscopic expressions for hydrodynamic quantities, we wonder if we can reformulate our microscopic dynamical equations in a manner which stratifies variables by our interest, with a sort of entropic link between the interesting stratum and the uninteresting stratum.

2.1.1 The Generalised Langevin Equation

We recall now the dynamics of phase space. With our Hamiltonian, $\mathscr{H}$, the dynamical evolution of any phase function A is

$$\frac{\mathrm{d}A}{\mathrm{d}t} = i\mathscr{L}A, \tag{2.1.1}$$

the formal solution of which is given as

$$A(t) = \exp(i\mathscr{L}t)A(0). \tag{2.1.2}$$

From now on I will sometimes use A to represent $A(0)$ *etc.* The Liouvillean, $\mathscr{L}$ is as practically intractable as the Hamiltonian, and Eq. 2.1.2 treats all degrees of freedom on equal grounds.

I introduce the equilibrium inner product to be used for the following analyses:

Definition 2.1.1 (Equilibrium Inner Product) *The equilibrium inner product* $[\cdot,\cdot]$ *maps the space of functions of* phase only *to itself.*

$$[A, B] = \int \mathrm{d}\Gamma \varrho_{\mathrm{eq}}(\Gamma)\; A^*(\Gamma)B(\Gamma) = \langle A^* B\rangle_{\mathrm{eq}}, \tag{2.1.3}$$

where * represents complex conjugation.

We now make a choice of some variables we care about. The variables of choice in hydrodynamics are all macroscopic, slowly and gradually varying compared to microscopic timescales and length-scales predictable from the Hamiltonian $\mathscr{H}$. The stratification of slow and fast variables is very appealing, and is a strong justification to the notion of local thermodynamic equilibrium used when discussing entropy in hydrodynamics. In practice, we do not need to work with *all* possible "slow" variables, because not all slow variables couple to the ones we are interested in. However, in principle, we can choose the set $\{A_i\}$ to include all "slow" variables and see where it takes us. We will take these variables to be linearly independent, because any variable that we might want which is linearly dependent can easily be incorporated. For simplicity we shall say we have orthogonalised our variables:

$$[A_i, A_j] = 0, \quad \text{if } i \neq j, \tag{2.1.4}$$

where $[\cdot,\cdot]$ is the equilibrium inner product, Eq. 2.1.3 in Def. 2.1.1. Finally if $\langle A_i \rangle \neq 0$, we shall replace it with $A_i - \langle A_i \rangle$. This set $\{A_i\}, i = 1, ..., m$ constitutes a subspace of dimension m on the phase space. Its significance shall become clear.

Definition 2.1.2 (Projection Operator) *The projection operator $\mathscr{P}$ associated with the vector subspace $\{A_i\}$ maps elements of the vector space of phase functions to that vector subspace.*

$$\begin{aligned}\mathscr{P} &= [\mathbf{A}, \cdot\ ] \cdot [\mathbf{A}, \mathbf{A}]^{-1} \cdot \mathbf{A} \\ &= \sum_j [A_i, \cdot\ ][\mathbf{A}, \mathbf{A}]^{-1}_{ij} A_j,\end{aligned} \tag{2.1.5}$$

here $\mathbf{A}$ is a column vector with components A_i, $[\cdot, \mathbf{A}]$ is a row vector with components $[A_i, \cdot\ ]$, $[\mathbf{A}, \mathbf{A}]^{-1}$ represents the inverse of the matrix with elements $[\mathbf{A}, \mathbf{A}]_{ij} = [A_i, A_j]$. Since $\{A_i\}$ are orthogonal, we have $[\mathbf{A}, \mathbf{A}]^{-1}_{ij} = \frac{\delta_{ij}}{[A_i, A_j]}$.

With this projection operator, and the identity operator on the vector space, $\mathscr{I}$, we can define the operator $\mathscr{Q} = \mathscr{I} - \mathscr{P}$. This operator is not usually named but, using the Latin etymology, I shall call it the abjection operator. This projects onto the subspace orthogonal to the subspace $\{A_i\}$. Every phase function therefore has components in the subspace and in the orthogonal subspace.

Both the projection and abjection operators are idempotent:

$$\mathscr{P}\mathscr{P} = \mathscr{Q}\mathscr{Q} = \mathscr{I}. \tag{2.1.6}$$

From here we can insert the identity operator into Eq. 2.1.1:

$$\begin{aligned}\frac{\mathrm{d}\mathbf{A}(t)}{\mathrm{d}t} &= \exp(i\mathscr{L}t)(\mathscr{P} + \mathscr{Q})i\mathscr{L}\mathbf{A}(0) \\ &= i\mathbf{\Omega} \cdot \mathbf{A}(t) + \exp(i\mathscr{L}t)i\mathscr{Q}\mathscr{L}\mathbf{A}(0)\end{aligned} \tag{2.1.7}$$

with $\mathscr{L}$ and its derivative operators acting component-wise, and where we have defined the *frequency matrix*

$$i\mathbf{\Omega} = [\mathbf{A}, i\mathscr{L}\mathbf{A}] \cdot [\mathbf{A}, \mathbf{A}]^{-1} \tag{2.1.8}$$

whose components reduce, in the orthogonal case, to

$$i\mathbf{\Omega}_{ij} = \sum_j \frac{[A_j, i\mathscr{L}A_i]}{[A_j, A_j]}. \tag{2.1.9}$$

Due to the symmetry of correlation functions [6], the diagonal elements of the frequency matrix vanish. The frequency matrix therefore projects the time derivative of each of our variables along each other variable. It is called the frequency matrix because, if we omit the second term on the right of Eq. 2.1.7, we recover a system of coupled equations where the time derivative of each variable depends linearly on the others. If there is an oscillatory component to the motion, the frequency matrix is where it will be found, and its elements will represent the frequency in some way.

The second term on the right of Eq. 2.1.7 requires a rather contrived mathematical trick. We first take the Laplace transformation of a propagator of an arbitrary operator $\mathscr{A}$ and express it in fraction form:

$$\begin{aligned}\int_0^\infty \mathrm{d}t \exp(-zt)\exp(-\mathscr{A}t) &= \int_0^\infty \exp(-zt)\sum_{n=0}^\infty \frac{(-1^n)}{n!}(\mathscr{A}t)^n \\ &= \sum_{n=0}^\infty \frac{(-1)^n}{n!}\mathscr{A}^n \int_0^\infty \mathrm{d}t \exp(-zt)t^n \\ &= \sum_{n=0}^\infty \frac{(-1)^n}{z^{n+1}}\mathscr{A}^n \\ &= (z+\mathscr{A})^{-1}, \end{aligned} \tag{2.1.10}$$

where partial integration neatly cancels the $n!$ factorial term. Next, we use Eq. 2.1.10 with the identity

$$(z+\mathscr{A}+\mathscr{B})^{-1} = (z+\mathscr{A})^{-1} + (z+\mathscr{A})^{-1}\mathscr{B}(z+\mathscr{A}+\mathscr{B})^{-1}, \tag{2.1.11}$$

easily proven with some algebra, to obtain:

$$\begin{aligned}&\int_0^\infty \mathrm{d}t \exp(-zt)\exp\big(-(\mathscr{A}+\mathscr{B})t\big) \\ &\quad= \int_0^\infty \exp(-zt)\exp(-\mathscr{A}t) \\ &\qquad - \int_0^\infty \mathrm{d}t \exp(-zt)\exp(-\mathscr{A}t)\mathscr{B}\int_0^\infty \mathrm{d}\tau \exp(-z\tau)\exp\big(-(\mathscr{A}+\mathscr{B})\tau\big).\end{aligned}$$

We consider the second integral, and perform a change of variables: $t \to t_1$, $t+\tau \to t_2$, such that the limits are $t_1 : 0 \to \infty$, $t_2 : t_1 \to \infty$:

$$\begin{aligned}&\int_0^\infty \mathrm{d}t_1 \exp(-\mathscr{A}t_1)\mathscr{B}\int_{t_1}^\infty \mathrm{d}t_2 \exp(-zt_2)\exp\big(-(\mathscr{A}+\mathscr{B})(t_2-t_1)\big)\\ &=\int_0^\infty \mathrm{d}t_2 \exp(-zt_2)\int_0^{t_2}\mathrm{d}t_1 \exp(-\mathscr{A}t_1)\mathscr{B}\exp\big(-(\mathscr{A}+\mathscr{B})(t_2-t_1)\big),\end{aligned}$$

having performed a standard (but careful) change of variables. This leaves us with:

$$\begin{aligned}\int_0^\infty \mathrm{d}t \exp(-zt)\exp\big(-(\mathscr{A}+\mathscr{B})t\big) = \int_0^\infty \mathrm{d}t \exp(-zt)\Bigg(&\exp(-\mathscr{A}t)\\ &-\int_0^t \mathrm{d}\tau \exp(-\mathscr{A}\tau)\mathscr{B}\exp\big(-(\mathscr{A}+\mathscr{B})(t-\tau)\big)\Bigg).\end{aligned} \tag{2.1.12}$$

The integrals are equal over equal limits, which implies equality of the integrands, *i.e.*:

$$\exp\big(-(\mathscr{A}+\mathscr{B})t\big) = \exp(-\mathscr{A}t) - \int_0^t \mathrm{d}\tau \exp(-\mathscr{A}\tau)\mathscr{B}\exp\big(-(\mathscr{A}+\mathscr{B})(t-\tau)\big). \tag{2.1.13}$$

Using Eq. 2.1.13, with $\mathscr{A}+\mathscr{B} = \mathscr{Q}\mathscr{L}$ and therefore $\mathscr{A} = \mathscr{L}$ and $\mathscr{B} = -\mathscr{P}$, we extract the identity we wish to use:

$$\exp(i\mathscr{L}t) = \exp(i\mathscr{Q}\mathscr{L}t) + \int_0^t \mathrm{d}\tau \exp\big(i\mathscr{L}(t-\tau)\big)i\mathscr{P}\mathscr{L}\exp(i\mathscr{Q}\mathscr{L}t). \tag{2.1.14}$$

Inserting this into Eq. 2.1.7 yields:

$$\begin{aligned}\frac{\mathrm{d}\mathbf{A}(t)}{\mathrm{d}t} &= i\mathbf{\Omega}\cdot\mathbf{A}(t) + \exp(i\mathscr{Q}\mathscr{L}t)i\mathscr{Q}\mathscr{L}\mathbf{A}(0)\\ &\quad+\int_0^t \mathrm{d}\tau \exp\big(i\mathscr{L}(t-\tau)\big)i\mathscr{P}\mathscr{L}\exp(i\mathscr{Q}\mathscr{L}t)i\mathscr{Q}\mathscr{L}\mathbf{A}(0).\end{aligned} \tag{2.1.15}$$

Let's examine these parts. The frequency matrix consists of those parts in the evolution of $\mathbf{A}$ which belong to the subspace - how the components of $\mathbf{A}$ affect each other. The other two terms feature the $i\mathscr{Q}\mathscr{L}\mathbf{A}$ term, which is the evolution of $\mathbf{A}$ due to all of the "fast" degrees of freedom. Because this term is always uncorrelated with $\mathbf{A}$ and arises due to microscopic degrees of freedom which we do not "see", we will call it the *random force* $\mathbf{f}$:

$$\begin{aligned}\mathbf{f}(t) &= \exp(i\mathscr{Q}\mathscr{L}t)\mathbf{f}(0),\\ \mathbf{f}(0) &= i\mathscr{Q}\mathscr{L}\mathbf{A}(0).\end{aligned} \tag{2.1.16}$$

Note that this random force evolves according to the anomalous propagator $\exp(i\mathscr{Q}\mathscr{L}t)$. The random force at $t = 0$ is defined as the evolution of $\mathbf{A}$ due the instantaneous influence of the fast degrees of freedom, but the "true" evolution of this quantity would be $\frac{\mathrm{d}\mathbf{f}}{\mathrm{d}t} = i\mathscr{L}\mathbf{f}(0)$, rather than $i\mathscr{Q}\mathscr{L}\mathbf{f}(0)$ as the anomalous propagator implies. This means that we discard any part of the evolution of $\mathbf{f}$ which is not orthogonal to $\mathbf{A}$, and that these parallel components to the evolution of $\mathbf{f}(0)$ are deposited elsewhere, as we shall now discuss.

The integrand in Eq. 2.1.15 has the term

$$\begin{aligned}\mathscr{P}i\mathscr{L}\mathbf{f}(t) &= [\mathbf{A}, i\mathscr{L}\mathbf{f}(t)]\cdot[\mathbf{A},\mathbf{A}]^{-1}\cdot\mathbf{A}\\ &= -[i\mathscr{L}\mathbf{A}, \mathbf{f}(t)]\cdot[\mathbf{A},\mathbf{A}]^{-1}\cdot\mathbf{A}\\ &= -[i\mathscr{Q}\mathscr{L}\mathbf{A}, \mathbf{f}(t)]\cdot[\mathbf{A},\mathbf{A}]^{-1}\cdot\mathbf{A}\\ &= -[\mathbf{f}(0), \mathbf{f}(t)]\cdot[\mathbf{A},\mathbf{A}]^{-1}\cdot\mathbf{A},\end{aligned} \tag{2.1.17}$$

since $i\mathscr{L}$ is anti-self-adjoint [35] and adding $\mathscr{Q}$ to the correlation inner product with $\mathbf{f}$, which is already orthogonal to $\mathbf{A}$, is equivalent to the identity operation. We can now define the *memory matrix* $\mathbf{M}$:

$$\mathbf{M}(t) = [\mathbf{f}(0), \mathbf{f}(t)]\cdot[\mathbf{A},\mathbf{A}]^{-1}, \tag{2.1.18}$$

which is essentially an anomalous time correlation function for the random force. This renders Eq. 2.1.15 in the form

$$\frac{\mathrm{d}\mathbf{A}(t)}{\mathrm{d}t} = i\boldsymbol{\Omega}\cdot\mathbf{A}(t) + \mathbf{f}(t) - \int_0^t \mathrm{d}\tau\ \mathbf{M}(\tau)\cdot\mathbf{A}(t-\tau), \tag{2.1.19}$$

where the propagator $\exp\big(i\mathscr{L}(t-\tau)\big)$ bypasses the memory matrix because the memory matrix is an inner product, and therefore inert to operators. Let's consider this equation under the pretence that our only knowledge is of our chosen variables $\mathbf{A}$. Its evolution is governed by a three terms. The first is deterministic, represent the coupling of the variables to each other with no admission of outside influence. The second is a fluctuating term, caused by the parts of the phase space which are "random" to us, since we only see our stratified phase space. The final term is an integral, involving the random force at all previous times (we are assuming that the dynamics started at $t = 0$ implicitly here), and also the variables themselves. This memory term comes because of the anomalous evolution of the random force, and represents how the evolution of the fast phase variables mix with our slow variables. Equations of this form are *generalised Langevin equations* (GLEs), as they represent the fluctuating, dissipative dynamics of variables with the added joy of a memory kernel, in this case the memory matrix.

We can take the inner product with $\mathbf{A}(0)$ of Eq. 2.1.19 to construct the equivalent equation for correlation functions:

$$\frac{\mathrm{d}\mathbf{C}(t)}{\mathrm{d}t} = i\boldsymbol{\Omega}\cdot\mathbf{C}(t) - \int_0^t \mathrm{d}\tau\ \mathbf{M}(\tau)\cdot\mathbf{C}(t-\tau), \tag{2.1.20}$$

with the correlation matrix $\mathbf{C}_{ij}$ having elements $[A_j(0), A_i(t)]$. This handily removes the term we consider random since it contains only phase averages. We can solve this equation with the introduction of Laplace transformations:

$$\tilde{\mathbf{C}}(z) = \int_0^\infty \mathrm{d}t\,\exp(-zt)\mathbf{C}(t), \tag{2.1.21}$$

$$\tilde{\mathbf{M}}(z) = \int_0^\infty \mathrm{d}t \exp(-zt)\mathbf{M}(t). \tag{2.1.22}$$

Let us take the transformation of Eq. 2.1.20, one term at a time:

$$\int_0^\infty \mathrm{d}t \exp(-zt)\frac{\mathrm{d}\mathbf{C}(t)}{\mathrm{d}t} = -\mathbf{C}(0) + z\tilde{\mathbf{C}}(z), \tag{2.1.23}$$

$$\int_0^\infty \mathrm{d}t \exp(-zt)i\boldsymbol{\Omega}\cdot\mathbf{C}(t) = i\boldsymbol{\Omega}\cdot\tilde{\mathbf{C}}(z), \tag{2.1.24}$$

$$\int_0^\infty \mathrm{d}t \exp(-zt)\int_0^t \mathrm{d}\tau\ \mathbf{M}(\tau)\cdot\mathbf{C}(t-\tau) = \tilde{\mathbf{M}}(z)\cdot\tilde{\mathbf{C}}(z), \tag{2.1.25}$$

having used partial integration in Eq. 2.1.23 and the convlution theorem in Eq. 2.1.25. Our GLE in the Laplace domain therefore reads:

$$\tilde{\mathbf{C}}(z) = \big(z\mathbf{I} - i\boldsymbol{\Omega} + \tilde{\mathbf{M}}(z)\big)^{-1}\cdot\mathbf{C}(0) \tag{2.1.26}$$

with $\mathbf{I}$ the identity matrix. These equations, 2.1.19, 2.1.20, and 2.1.26, are formally exact - no approximations were made in their derivation. They are equivalent to 2.1.2, except the former two are integro-differential equations, far harder to solve. The equation in the Laplace domain has shifted the problem to the calculation of the memory matrix, but since the "correlation functions" of the memory matrix $\mathbf{M}(t)$ evolve according to the anomalous propagator $\exp(i\mathscr{Q}\mathscr{L}t)$, this exercise appears to have been fraught with vanity.

It is now, however, that we brandish our weapon of choice, namely our selection of all the "slow" phase functions. The memory matrix evolves in the fast stratum of phase space, and therefore, insofar as this stratification is cleanly possible, will be by definition characterised by decay times much shorter than those characterising $\mathbf{A}$. And since the anomalous propagator would erase any evolution coupled to the slow variables, we can confidently propose, where such timescale separation is appropriate:

$$\mathbf{M}(t) \approx \boldsymbol{\Gamma}\delta(t), \tag{2.1.27}$$

such that

$$\begin{aligned}\boldsymbol{\Gamma} &= \int_0^\infty \mathrm{d}t\ \mathbf{M}(t)\\ &= \tilde{\mathbf{M}}(0).\end{aligned} \tag{2.1.28}$$

This has the following effect on Eqs. 2.1.19 and 2.1.20:

$$\frac{\mathrm{d}\mathbf{A}(t)}{\mathrm{d}t} = i\boldsymbol{\Omega}\cdot\mathbf{A}(t) - \boldsymbol{\Gamma}\cdot\mathbf{A}(t) + \mathbf{f}(t), \tag{2.1.29}$$

$$\frac{\mathrm{d}\mathbf{C}(t)}{\mathrm{d}t} = (i\boldsymbol{\Omega} - \boldsymbol{\Gamma})\cdot\mathbf{C}(t). \tag{2.1.30}$$

The former represents the memoryless Langevin equation, and the latter, having taken an average, can be solved as:

$$\mathbf{C}(t) = \exp\big((i\boldsymbol{\Omega} - \boldsymbol{\Gamma})t\big)\cdot\mathbf{C}(0). \tag{2.1.31}$$

We see then that the effect of many degrees of freedom, operating on a far faster timescale than our variables of interest, is a damping effect on the natural oscillations that these variables impose on each other. The timescale separation removed the memory kernel in our integral, and for this reason this separation is often called the Markovian approximation. Indeed, in the case that we have an isolated slow variable, uncoupled to any other slow variables, Eq. 2.1.31 becomes:

$$C(t) = \exp(-\Gamma t) C(0). \tag{2.1.32}$$

The frequency of appearance of exponential decays and therefore Lorentzian spectra in irreversible physical phenomena is indicative of our good choice of variables very slow and gradual compared to microscopic dynamics.

2.1.2 The Memory Function

In many cases, we are not interested in the macroscopic functions of thermodynamics and hydrodynamics, but rather extensions of hydrodynamics into the microscopic realm. The defining and troublesome property of dense fluids is the lack of a "small parameter", such as atomic displacements in solids or density in gases, which allows us to write away the complexity of microscopic dynamics. We shall need to see what can be done, therefore, about the memory function when our timescales edge uncomfortably close to those of the Hamiltonian.

The definition, Def. 2.1.2, of the projection and abjection operators guarantee the memory matrix to have all the same symmetries as standard time correlation functions, and indeed the anomalous propagator is just as unitary as the true propagator.

The zero-time value of the memory matrix, $\mathbf{M}(0)$ can be found directly:

$$\begin{aligned}
\mathbf{M}(0) &= [\mathbf{f}, \mathbf{f}] \cdot [\mathbf{A}, \mathbf{A}]^{-1} \\
&= [i\mathscr{Q}\mathscr{L}\mathbf{A}, i\mathscr{Q}\mathscr{L}\mathbf{A}] \cdot [\mathbf{A}, \mathbf{A}]^{-1} \\
&= \Big[\dot{\mathbf{A}} - [\mathbf{A}, \dot{\mathbf{A}}] \cdot [\mathbf{A}, \mathbf{A}]^{-1} \cdot \mathbf{A}, \dot{\mathbf{A}} - [\mathbf{A}, \dot{\mathbf{A}}] \cdot [\mathbf{A}, \mathbf{A}]^{-1} \cdot \mathbf{A}\Big] \cdot [\mathbf{A}, \mathbf{A}]^{-1} \\
&= [\dot{\mathbf{A}}, \dot{\mathbf{A}}] \cdot [\mathbf{A}, \mathbf{A}]^{-1} - \boldsymbol{\Omega} \cdot \boldsymbol{\Omega} \\
&= - \left.\frac{\mathrm{d}^2 \mathbf{C}(t)}{\mathrm{d}t^2}\right|_{t=0} \cdot \mathbf{C}(0)^{-1} - \boldsymbol{\Omega} \cdot \boldsymbol{\Omega},
\end{aligned}$$

where the cross-terms in the larger inner product on the third line cancel out due to the anti-self-adjoint property of $i\mathscr{L}$ in the inner product, and the appearance of the frequency matrices between the third and fourth line requires some careful handling of indices not worth explicating here. We can perform a full series expansion of $\mathbf{M}(t)$ in terms of correlation function derivatives at $t = 0$, but this will only get us so far.

If we examine the anomalous evolution of the fluctuating force in Eq. 2.1.16:

$$\frac{\mathrm{d}\mathbf{f}(t)}{\mathrm{d}t} = i\mathscr{Q}\mathscr{L}\mathbf{f}(t),$$

we can introduce the operator $\mathscr{L}_1$, perhaps called the (first order) reduced Liouvillean, such that

$$\frac{\mathrm{d}\mathbf{f}(t)}{\mathrm{d}t} = i\mathscr{L}_1\mathbf{f}(t). \tag{2.1.33}$$

Having done this, we can define a new projection operator, the (first order) reduced projector

$$\mathscr{P}_1 = [\mathbf{f}, \cdot\,] \cdot [\mathbf{f}, \mathbf{f}]^{-1} \cdot \mathbf{f}, \tag{2.1.34}$$

which, because $\mathscr{P}\mathscr{P}_1 = \mathscr{P}_1\mathscr{P} = \mathbf{0}$, further stratifies phase space into the variables orthogonal to $\mathbf{A}$ but parallel to $\mathbf{f}$ and those orthogonal to both. Note that if we made the fast and slow identification when choosing $\mathbf{A}$, this does *not* mean that the $\mathscr{Q}_1$ defined from $\mathscr{P}_1$ projects onto a yet faster portion of phase space - it's just separate. We can then repeat our manipulations to obtain the GLE for the random force:

$$\frac{\mathrm{d}\mathbf{f}(t)}{\mathrm{d}t} = i\mathbf{\Omega}_1 \cdot \mathbf{f}(t) - \int_0^t \mathrm{d}\tau \mathbf{M}_1(t) \cdot \mathbf{f}(t-\tau) + \mathbf{f}_1(t), \tag{2.1.35}$$

where all symbols with subscript 1 have obvious definitions. We now take the inner product with $\mathbf{f}(0)$

$$\frac{\mathrm{d}\mathbf{M}(t)}{\mathrm{d}t} = i\mathbf{\Omega}_1 \cdot \mathbf{M}(t) - \int_0^t \mathrm{d}\tau \mathbf{M}_1(t) \cdot \mathbf{M}(t-\tau). \tag{2.1.36}$$

We have therefore shifted the formalism to a more abstract level, generating equivalents to Eqs. 2.1.19 and 2.1.20. Laplace transforming to retrieve the equivalent of Eq. 2.1.26, we have

$$\tilde{\mathbf{M}}(t) = (z\mathbf{I} - i\mathbf{\Omega}_1 + \tilde{\mathbf{M}_1}(z))^{-1} \cdot \mathbf{M}(0), \tag{2.1.37}$$

and so

$$\tilde{\mathbf{C}}(z) = \left(z\mathbf{I} - i\mathbf{\Omega} + (z\mathbf{I} - i\mathbf{\Omega}_1 + \tilde{\mathbf{M}}_1(z))^{-1} \cdot \mathbf{M}(0)\right)^{-1} \cdot \mathbf{C}(0). \tag{2.1.38}$$

If we project ever further and further into phase space, we create ever longer and longer continued fraction expressions for $\mathbf{C}$, which involve the zero-time elements of more and more abstract memory matrices:

$$\mathbf{M}_1(0) = -\left.\frac{\mathrm{d}^2\mathbf{M}(t)}{\mathrm{d}t^2}\right|_{t=0} \cdot \mathbf{M}(0)^{-1} - \mathbf{\Omega_1} \cdot \mathbf{\Omega_1}, \tag{2.1.39}$$

$$\mathbf{M}_2(0) = -\left.\frac{\mathrm{d}^2\mathbf{M}_1(t)}{\mathrm{d}t^2}\right|_{t=0} \cdot \mathbf{M}(0)^{-1} - \mathbf{\Omega_2} \cdot \mathbf{\Omega_2}, \tag{2.1.40}$$

and so on. These expressions involve the equal-time correlations of our variables $\mathbf{A}$ and their time derivatives. Such phase means are often amenable to calculations, especially using the various symmetries of correlation functions and their derivatives, but these quantities become increasingly frustrating to calculate as the series grows in terms. The increasingly abstract interpretation of the high order memory matrices also obstructs the insight gained by these analyses.

However, if we're using rather than receiving our physical insight, we can make some well-informed decisions and see the consequences. For example, we can terminate the continued fraction in Eq. 2.1.38, and make some sensible estimates about the functional form of the memory matrices. Having done so, we can make predictions or identifications.

2.1.3 Generalised Hydrodynamics

We shall dive straight into the memory functions by applying them to the variables of hydrodynamics. On can write down equations for microscopic extensions of hydrodynamic variables using the Irving-Kirkwood procedure [35]. Such variables are amenable to the formalism of Mori-Zwanzig theory. We begin, as we have just set out, with a set of variables which are conserved as the wavevector represents macroscopic length scales, $k \to 0$. In this case for each A_i we can define current densities:

$$\frac{\mathrm{d}A_i}{\mathrm{d}t} = i\mathbf{k}\cdot\mathbf{j}_i(t,\mathbf{k}), \tag{2.1.41}$$

where we will have to drop the $\mathbf{A}$ vector notation because it will conflict with the true tensorial nature of the current densities and $\mathbf{k}$. We restrict our attention, for now, to small wavevectors. This has consequences for the GLE:

$$\frac{\mathrm{d}A_i(t,\mathbf{k})}{\mathrm{d}t} = \sum_j \left(i\Omega_{ij}(k)A_j(t,\mathbf{k}) - \int_0^t \mathrm{d}\tau M_{ij}(t,k)A_j(t-\tau,\mathbf{k}) \right) + f_i(t,\mathbf{k}), \tag{2.1.42}$$

where the phase averages in Ω and M depend only on the magnitude of $\mathbf{k}$ due to the supposed isotropy of the fluid. From the definition of the frequency matrix, Eq. 2.1.8, we can see that its components vanish as k in the limit $k \to 0$. Note that the random force can be written:

$$f_i(t,\mathbf{k}) = -\exp(i\mathscr{L}t)(0,\mathbf{k})\mathscr{L}\mathscr{Q}\mathbf{k}\cdot\mathbf{j}_i(t,\mathbf{k}), \tag{2.1.43}$$

giving it a proportionality to k. Using Eq. 2.1.14, we can write the time-evolved random force as:

$$\begin{aligned} f_i(t,\mathbf{k}) &= \exp(i\mathscr{Q}\mathscr{L}t)f_i(0,\mathbf{k}) \\ &= \exp(i\mathscr{L}t)f_i(0,\mathbf{k}) - \sum_j \int_0^t \mathrm{d}\tau \frac{[A_j(0,\mathbf{k}), i\mathscr{L}f_i(t,\mathbf{k})]}{[A_j(\mathbf{k}), A_j(0,\mathbf{k})]} A_j(t-\tau,\mathbf{k}) \\ &= \exp(i\mathscr{L}t)f_i(0,\mathbf{k}) + \sum_j \int_0^t \mathrm{d}\tau \frac{[i\mathscr{L}A_j(0,\mathbf{k}), f_i(t,\mathbf{k})]}{[A_j(\mathbf{k}), A_j(0,\mathbf{k})]} A_j(t-\tau,\mathbf{k}), \end{aligned}$$

having used the anti-self-adjoint property of the Liouvillean between the second and third lines. Combining this with Eqs. 2.1.41 and 2.1.43, we see that the anomalous part of the propagator is proportional to k^2, whereas the "true" evolution of the random force is proportional to k. Since the memory matrix is an anomalous autocorrelation of the force, all of the anomalous parts are proportional to k^3 or k^4. In the small wavevector limit, therefore, the leading terms of M_{ij} are just ordinary time correlation functions. Physically this represents the very small impact our macropscopic variables have on the microscopic evolution of the system - as our functions of choice dwarf the microscopic scales of $\mathscr{H}$, the fast stratum of the phase space becomes nearly the entire phase space. This result will be very useful in applying this analysis.

Transverse Current

We are now ready to name some functions and feed them to the the Mori Zwanzig war engine we've developed. We note that the (mass) density, momentum current density, and energy current density are all coupled [6]. When it comes to choosing slow variables, therefore, we should never choose any one of these without the others. However, since we are working with Fourier components, we can split the momentum current density:

$$\begin{aligned}\mathbf{j}(t,\mathbf{k}) &= \frac{\mathbf{k}\mathbf{k}}{k^2}\cdot\mathbf{j}(t,\mathbf{k}) + \Big(\mathbf{I} - \frac{\mathbf{k}\mathbf{k}}{k^2}\Big)\cdot\mathbf{j}(t,\mathbf{k}) \\ &= \mathbf{j}^{\mathrm{L}}(t,\mathbf{k}) + \mathbf{j}^{\mathrm{T}}(t,\mathbf{k})\end{aligned} \tag{2.1.44}$$

which defines the *longitudinal component*, $\mathbf{j}^{\mathrm{L}}$ of the current density, parallel to the wavevector, and the *transverse component*, $\mathbf{j}^{\mathrm{T}}$, perpendicular to it. In this case, we can see that only the longitudinal component is coupled to the density and energy current density, and the transverse component does not carry such information. If, adopting a Cartesian co-ordinate system, we declare the z-axis to point in the direction of $\mathbf{k}$, then the transverse current density components can be written

$$j_x^{\mathrm{T}}(t,\mathbf{k}) = \frac{1}{V}\sum_{i=1}^{N} v_x^i \exp\big(-i\mathbf{k}\cdot\mathbf{r}_i\big), \tag{2.1.45}$$

and similarly for the y-component, and we have moved the particle index to a superscript to leave space for the co-ordinate subscript. Likewise, in the case of absent streaming velocity, using the microscopic expression for the stress tensor τ_{M} [8], we can write:

$$\begin{aligned}\frac{\mathrm{d}j_x^{\mathrm{T}}}{\mathrm{d}t} &= (i\mathbf{k}\cdot\boldsymbol{\tau}(t,\mathbf{k}))_x \\ &= ik\tau_{zx}(t,\mathbf{k}) \\ &= -\frac{1}{V}\sum_{i=1}^{N} ik\exp\big(-i\mathbf{k}\cdot\mathbf{r}^{ij}\big)\left(m^i v_z^i v_x^i - \frac{1}{2}\sum_{j\neq i}^{N}\frac{r_z^{ij}F_x^{ij}}{i\mathbf{k}\cdot\mathbf{r}^{ij}}\big(\exp\big(i\mathbf{k}\cdot\mathbf{r}^{ij}\big)-1\big)\right),\end{aligned} \tag{2.1.46}$$

and similar for the y-component. The projection operator in this case is simply:

$$\begin{aligned}\mathscr{P} &= \frac{[j_x^{\mathrm{T}}(0,\mathbf{k}),\cdot\,]}{[j_x^{\mathrm{T}}(0,\mathbf{k}),j_x^{\mathrm{T}}(0,\mathbf{k})]}j_x^{\mathrm{T}}(0,\mathbf{k}) \\ &= V\frac{[j_x^{\mathrm{T}}(0,\mathbf{k}),\cdot\,]}{mnk_{\mathrm{B}}T}j_x^{\mathrm{T}}(0,\mathbf{k}),\end{aligned} \tag{2.1.47}$$

where $n = \frac{N}{V}$, we have assumed all atoms have the same mass, and have (finally) chosen an ensemble - the canonical ensemble. The one element of the frequency matrix vanishes, due to correlation function symmetry [6]. In this case, our autocorrelation function:

$$C^{\mathrm{T}}(t,k) = V\frac{[j_x^{\mathrm{T}}(0,\mathbf{k}),j_x^{\mathrm{T}}(t,\mathbf{k})]}{mnk_{\mathrm{B}}T}, \tag{2.1.48}$$

evolves according to the equation:

$$\frac{\mathrm{d}C^{\mathrm{T}}(t,k)}{\mathrm{d}t} = -\int_0^t \mathrm{d}\tau M^{\mathrm{T}}(t,k)C^{\mathrm{T}}(t-\tau,k), \tag{2.1.49}$$

where the memory kernel now takes the form:

$$\begin{aligned} M^{\mathrm{T}}(t,k) &= \left[\frac{\mathrm{d}j_x^{\mathrm{T}}(0,\mathbf{k})}{\mathrm{d}t}, \frac{\mathrm{d}j_x^{\mathrm{T}}(t,\mathbf{k})}{\mathrm{d}t}\right]\frac{V}{mnk_{\mathrm{B}}T} \\ &= -\frac{Vk^2}{mnk_{\mathrm{B}}T}[\tau_{zx}(0,\mathbf{k}),\tau_{zx}(t,\mathbf{k})], \end{aligned}$$

so long as we are taking the $k \to 0$ limit. Here we will employ the Markovian approximation too:

$$\frac{\mathrm{d}C^{\mathrm{T}}(t,k)}{\mathrm{d}t} = -\int_0^\infty \mathrm{d}\tau \frac{Vk^2}{mnk_{\mathrm{B}}T}[\tau_{zx}(0,\mathbf{k}),\tau_{zx}(\tau,\mathbf{k})]\ C^{\mathrm{T}}(t,k). \tag{2.1.50}$$

So, in practice, we fully integrate the stress autocorrelation function, hoping that the evolution of C^{T} is slow enough that ignoring the memory convolution is warranted. We temporarily define the quantity

$$\mu(k) = \int_0^\infty \mathrm{d}\tau[\tau_{zx}(0,\mathbf{k}),\tau_{zx}(\tau,\mathbf{k})], \tag{2.1.51}$$

which simplifies our GLE to

$$\frac{\mathrm{d}C^{\mathrm{T}}(t,k)}{\mathrm{d}t} = -\frac{Vk^2}{mnk_{\mathrm{B}}T}\mu(k)\ C^{\mathrm{T}}(t,k), \tag{2.1.52}$$

which is easily solved, given our normalisation defined in Eq. 2.1.48:

$$C^{\mathrm{T}}(t,k) = \exp\Big(-\frac{Vk^2\mu(k)}{mnk_{\mathrm{B}}T}\ t\Big). \tag{2.1.53}$$

If we have a lot of confidence in our $k \to 0$ limit, we can insert it directly into $\mu(k)$, giving us our approximation for the expression for the stress tensor $\boldsymbol{\tau}$ at macroscopic scales:

$$\tau_{zx} = \frac{1}{V}\sum_{i=1}^{N}\left(m^i v_z^i v_x^i - \frac{1}{2}\sum_{j\neq i}^{N} r_z^{ij}F_x^{ij}\right), \tag{2.1.54}$$

such that we have

$$\mu = \int_0^\infty \mathrm{d}\tau[\tau_{zx}(0),\tau_{zx}(t)], \tag{2.1.55}$$

and the transverse autocorrelation function is

$$C^{\mathrm{T}}(t,k) = \exp\Big(-\frac{Vk^2\mu}{mnk_{\mathrm{B}}T}\ t\Big), \tag{2.1.56}$$

which represents the damping of all collective motion, no matter the wavelength. Its Laplace transform is:

$$\tilde{C}^{\mathrm{T}}(z,k) = \frac{1}{z + \dfrac{Vk^2\mu}{mnk_{\mathrm{B}}T}}, \tag{2.1.57}$$

from which we can retrieve the real spectrum:

$$\begin{aligned} C^{\mathrm{T}}(\omega,k) &= \mathrm{Re}\left[\frac{1}{\pi}\,\tilde{C}^{\mathrm{T}}(i\omega,k)\right] \\ &= \mathrm{Re}\left[\frac{1}{\pi}\,\frac{1}{i\omega + \dfrac{Vk^2\mu}{mnk_{\mathrm{B}}T}}\,C^{\mathrm{T}}(0)\right] \\ &= \frac{1}{\pi}\,\frac{1}{\omega^2 + k^2\frac{V\mu}{mnk_{\mathrm{B}}T}}. \end{aligned} \tag{2.1.58}$$

which is a single Lorentzian peak, centered on zero-frequency at each wavelength, monotonically decaying at higher frequencies. With this, we have recovered a characteristic behaviour of fluids - their inability to support shear waves.

Our final step here is to compare the suggestively defined μ with a hydrodynamic quantity. We begin by splitting the velocity field into two components:

$$\mathbf{v}(t,\mathbf{r}) = \mathbf{v}^{\mathrm{L}}(t,\mathbf{r}) + \mathbf{v}^{\mathrm{T}}(t,\mathbf{r}), \tag{2.1.59}$$

where

$$\boldsymbol{\nabla}\times\mathbf{v}^{\mathrm{L}}(t,\mathbf{r}) = 0, \tag{2.1.60}$$

$$\boldsymbol{\nabla}\cdot\mathbf{v}^{\mathrm{T}}(t,\mathbf{r}) = 0. \tag{2.1.61}$$

Taking Fourier transformations of these two equations, we see that

$$\mathbf{k}\times\mathbf{v}^{\mathrm{L}}(t,\mathbf{k}) = 0, \tag{2.1.62}$$

$$\mathbf{k}\cdot\mathbf{v}^{\mathrm{T}}(t,\mathbf{k}) = 0. \tag{2.1.63}$$

We assume that the fluid is not far from equilibrium, such that both the velocity and its gradients are small, and therefore $\frac{\mathrm{d}\mathbf{v}}{\mathrm{d}t} \approx \frac{\partial\mathbf{v}}{\partial t}$. From there we take the Fourier components of the momentum continuity equations:

$$\begin{aligned} \frac{\partial\mathbf{j}(t,\mathbf{k})}{\partial t} &= -i\mathbf{k}\cdot\boldsymbol{\tau}(t,\mathbf{k}) \\ &= -\eta k^2\mathbf{v}(t,\mathbf{k}) - \Big(\frac{1}{3}\eta + \zeta\Big)\mathbf{k}\,\mathbf{k}\cdot\mathbf{v}(t,\mathbf{k}) + i\mathbf{k}P(t,\mathbf{k}), \end{aligned} \tag{2.1.64}$$

where η is the shear viscosity, ζ is the bulk viscosity, and P is the pressure field. Because $\mathbf{v}^{\mathrm{T}}(t,\mathbf{k})$ is perpendicular to $\mathbf{k}$,

$$\frac{\partial\mathbf{j}^{\mathrm{T}}(t,\mathbf{k})}{\partial t} = -\eta k^2\mathbf{v}^{\mathrm{T}}(t,\mathbf{k}). \tag{2.1.65}$$

Accepting further that density fluctuations are small like velocity fluctuations, we identify

$$\frac{\partial \mathbf{v}^{\mathrm{T}}(t,\mathbf{k})}{\partial t} = \frac{\eta}{mn} k^2 \mathbf{v}^{\mathrm{T}}(t,\mathbf{k}), \tag{2.1.66}$$

with n the mean particle concentration and m the particle mass, as it was in the microscopic current autocorrelation function analysis above. The formal solution to this equation is

$$\mathbf{v}^{\mathrm{T}}(t,\mathbf{k}) = \mathbf{v}^{\mathrm{T}}(0,\mathbf{k}) \exp\left(\frac{k^2 \eta}{mn} t\right). \tag{2.1.67}$$

We now employ the intuitive fact that fluctuations in microscopic phase variables decay according to the same equations which govern their macroscopic equivalents, which can be formally derived using the fluctuation-dissipation theorem [36]. This allows us to make the following identification on the basis of Eqs. 2.1.56 and 2.1.67:

$$\eta = \frac{V}{k_{\mathrm{B}} T} \int_0^\infty \mathrm{d}\tau [\tau_{zx}(0), \tau_{zx}(\tau)], \tag{2.1.68}$$

which is an example of a *Green-Kubo* formula, which relates a transport property to the relaxation of microscopic fluctuations. Should we wish to relax the Markovian approximation, the non-Markovian and microscopic identification for viscosity would naturally be

$$\eta(t,\mathbf{k}) = \frac{V}{k_{\mathrm{B}} T} [\tau_{zx}(0,\mathbf{k}), \tau_{zx}(\tau,\mathbf{k})]. \tag{2.1.69}$$

With this identification, Eq. 2.1.49 becomes:

$$\frac{\mathrm{d}C^{\mathrm{T}}(t,k)}{\mathrm{d}t} = -\frac{k^2}{mn} \int_0^t \mathrm{d}\tau \; \eta(t,k) C^{\mathrm{T}}(t-\tau,k), \tag{2.1.70}$$

the Laplace transform of which gives the solution (using the convolution theorem):

$$\tilde{C}^{\mathrm{T}}(z,k) = \frac{1}{z + k^2 \dfrac{\tilde{\eta}(z,k)}{mn}} \tag{2.1.71}$$

Transverse Collective Modes

The exponential decay of the transverse autocorrelation function was due to our choice of variables. In the single variable case, as we saw, a quantity can only decay. Since the transverse current density does not couple to the mass, energy, or longitudinal current densities, the only other slow variables which it might couple to which come to mind are its derivatives. In this sense, by ignoring a complicated relationship between the transverse current density and its derivatives, we allowed it only to access dissipative dynamics. Our first amendment is therefore to expand our list of slow transverse variables. For our slow variables $\mathbf{A}$, we choose:

$$\mathbf{A} = \begin{bmatrix} j_x^{\mathrm{T}}(t,\mathbf{k}) \\ \tau_{zx}(t,\mathbf{k}) \end{bmatrix}, \tag{2.1.72}$$

such that the correlation matrix is

$$[\mathbf{A},\mathbf{A}] = \frac{k_\mathrm{B}T}{V}\begin{bmatrix} mn & 0 \\ 0 & G_\infty(k)\end{bmatrix}, \tag{2.1.73}$$

where we have defined the *infinite frequency shear modulus*:

$$G_\infty(k) = \frac{V}{k_\mathrm{B}T}[\tau_{zx}(0,\mathbf{k}),\tau_{zx}(0,\mathbf{k})], \tag{2.1.74}$$

which is also the zero-time value of the generalised viscosity, Eq. 2.1.69. The frequency matrix, which will allow for some non-decaying behaviour, is

$$\begin{aligned} i\mathbf{\Omega}(k) &= \frac{V}{k_\mathrm{B}T}\begin{bmatrix} 0 & \left[\tau_{zx}(t,\mathbf{k}), \frac{\mathrm{d}j_x^\mathrm{T}(t,\mathbf{k})}{\mathrm{d}t}\right] \\ \left[j_x^\mathrm{T}(t,\mathbf{k}), \frac{\mathrm{d}\tau_{zx}(t,\mathbf{k})}{\mathrm{d}t}\right] & 0 \end{bmatrix} \cdot \begin{bmatrix} \frac{1}{mn} & 0 \\ 0 & \frac{1}{G_\infty(k)}\end{bmatrix} \\ &= \frac{V}{k_\mathrm{B}T}\begin{bmatrix} 0 & \left[\tau_{zx}(t,\mathbf{k}), \frac{\mathrm{d}j_x^\mathrm{T}(t,\mathbf{k})}{\mathrm{d}t}\right] \\ \left[-\frac{\mathrm{d}j_x^\mathrm{T}(t,\mathbf{k})}{\mathrm{d}t}, \tau_{zx}(t,\mathbf{k})\right] & 0 \end{bmatrix} \cdot \begin{bmatrix} \frac{1}{mn} & 0 \\ 0 & \frac{1}{G_\infty(k)}\end{bmatrix} \\ &= \frac{V}{k_\mathrm{B}T}\begin{bmatrix} 0 & ik \\ ik\,\frac{G_\infty(k)}{mn} & 0\end{bmatrix}. \end{aligned} \tag{2.1.75}$$

We can't write down the memory matrix, unless we make a deal with Laplace's demon, but we can deduce its form. The derivative of j_x^T lies on our slow subspace, therefore its corresponding random force vanishes. We therefore write for the memory matrix:

$$\mathbf{M}(t,\mathbf{k}) = \begin{bmatrix} 0 & 0 \\ 0 & M^\mathrm{T}(t,k)\end{bmatrix}. \tag{2.1.76}$$

We can now write down the Laplace transformation of our GLE in terms of our unknown, the memory function M^T:

$$\begin{aligned} \tilde{\mathbf{C}}(z) &= \begin{bmatrix} z & ik \\ ik\,\frac{G_\infty(k)}{mn} & z+\tilde{M}^\mathrm{T}(z,k)\end{bmatrix}^{-1}\cdot\mathbf{C}(0) \\ &= \frac{1}{z(z+\tilde{M}^\mathrm{T}(z,k))+k^2\frac{G_\infty(k)}{mn}}\begin{bmatrix} z+\tilde{M}^\mathrm{T}(z,k) & -ik \\ -ik\,\frac{G_\infty(k)}{mn} & z\end{bmatrix}\cdot\mathbf{C}(0). \end{aligned} \tag{2.1.77}$$

The quantity of interest, as before, is the transverse current density autocorrelation function, the solution to which, having done some tidying up, is:

$$\tilde{C}^\mathrm{T}(z,k) = \frac{1}{z+\frac{k^2c^\mathrm{T}(k)^2}{z+\tilde{M}^\mathrm{T}(z,k)}}C^\mathrm{T}(0), \tag{2.1.78}$$

such that

$$c^\mathrm{T}(k)^2 = \frac{G_\infty(k)}{mn} \tag{2.1.79}$$

where $c^{\mathrm{T}}(k)$ can be considered a wavevector-dependent speed of sound. Relapsing to our old habits, we invoke the Markovian approximation:

$$M^{\mathrm{T}}(t,k) \approx \frac{1}{\tau^{\mathrm{T}}(k)}\delta(t), \tag{2.1.80}$$

having defined a characteristic transverse relaxation time (as opposed to frequency or decay rate Γ). Now we can extract the Fourier spectrum:

$$\begin{aligned} C^{\mathrm{T}}(\omega,k) &= \mathrm{Re}\left[\frac{1}{\pi}\,\tilde{C}^{\mathrm{T}}(i\omega,k)\right] \\ &= \mathrm{Re}\left[\frac{1}{\pi}\,\frac{1}{i\omega + \dfrac{k^2 c^{\mathrm{T}}(k)^2}{i\omega + \frac{1}{\tau^{\mathrm{T}}(k)}}}\,C^{\mathrm{T}}(0)\right] \\ &= \frac{1}{\pi}\,\frac{k^2 c^{\mathrm{T}}(k)^2 \tau^{\mathrm{T}}(k)}{\omega^2 + \tau^{\mathrm{T}}(k)^2\big((k^2 c^{\mathrm{T}}(k)^2 - \omega^2\big)^2}. \end{aligned} \tag{2.1.81}$$

In order to provide more meaning to the quantities in this equation, we compare Eq. 2.1.78 to Eq. 2.1.71 to make the identification:

$$\tilde{\eta}(z,k) = \frac{G_\infty(k)}{z + \dfrac{1}{\tau^{\mathrm{T}}(k)}} \tag{2.1.82}$$

This implies that the generalised viscosity, related to the memory kernel in the single-variable case, undergoes exponential decay with time:

$$\eta(t,k) = G_\infty \exp\left(-\frac{t}{\tau^{\mathrm{T}}(k)}\right), \tag{2.1.83}$$

which implies that the the addition of a second slow variable coupled to our transverse current density is equivalent to having memory effects, indeed, merely a nonzero decay time, in the single-variable case. As we shall see, the existence of this other dynamical variable, or a not-too-rapid decay of shear stress, allows for propagating transverse elastic waves forbidden under normal hydrodynamics.

The condition for propagating collective modes at a given wavevector is, roughly speaking, the existence of a peak at nonzero frequency in the current density spectrum. Taking the derivative and equating it to zero, we see that this condition is equivalent to

$$\omega^{\mathrm{T}}(k)^2 = k^2 c^{\mathrm{T}}(k)^2 - \frac{1}{2\tau^{\mathrm{T}}(k)^2}, \tag{2.1.84}$$

where $\omega^{\mathrm{T}}(k)$ is the position of the peak, interpreted as the frequency of the transverse collective mode. Below a critical wavevector, k_{g}, this frequency is imaginary and thereore

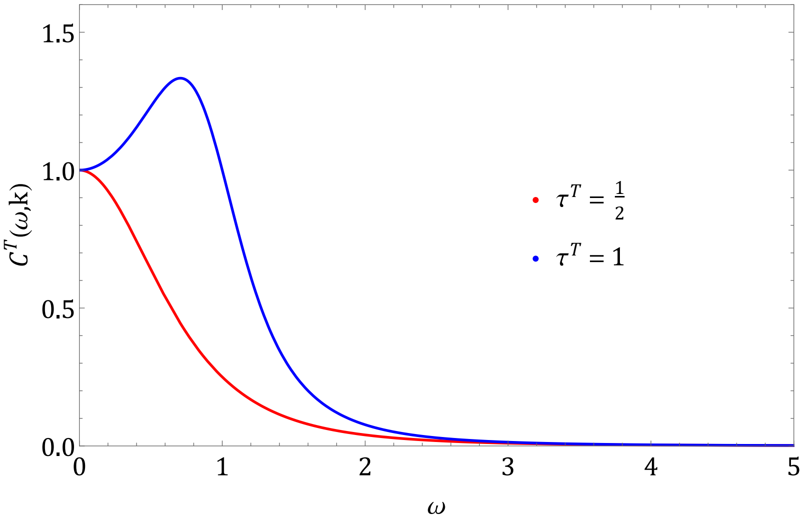

Figure 2.1: The transverse current spectrum $C^{\mathrm{T}}(\omega, k)$ at an arbitrary wavevector, showing non-propagating modes for $\tau^{\mathrm{T}}(k) = \frac{1}{2}$ and propagating modes for $\tau^{\mathrm{T}}(k) = 1$, distinguishable by the clear peak at around $\omega = 0.8$.

does not correspond to propagating modes. The transverse spectrum, unlike the longitudinal spectrum, is therefore *gapped*, existing only at short wavelengths to whom the fluid somehow provides an elastic medium. The minimum, gapped, wavevector, k_{g}, is given by:

$$k_{\mathrm{g}} = \frac{1}{\sqrt{2}} \frac{1}{c^{\mathrm{T}}(k)\tau^{\mathrm{T}}(k)}. \tag{2.1.85}$$

Plots of propagating and non-propagating spectra, separated by different values of $\tau^{\mathrm{T}}(k)$, are shown in Fig. 2.1.

Finally, we can relate $\tau^{\mathrm{T}}(k)$ to other existing quantities. Our non-Markovian viscosity in Eq. 2.1.82 has the following Laplace spectrum:

$$\tilde{\eta}(z, k) = \frac{G_\infty(k)}{z + \dfrac{1}{\tau^{\mathrm{T}}(k)}}, \tag{2.1.86}$$

from which we can see that in the limit of zero frequency:

$$\eta(\omega \to 0, k) = \tau^{\mathrm{T}}(k) G_\infty(k), \tag{2.1.87}$$

meaning that τ^{T} is the ratio of high-frequency and low-frequency responses to gradients in velocity. If we take Eq. 2.1.85 to its zero-wavevector limit (bear in mind that since we took M^{T} to be a standard autocorrelation function with no anomalous evolution, we are already approximating k to be small), we get an approximation for a $k-$independent k_{g} using macroscopic quantities alone:

$$k_{\mathrm{g}} = \frac{1}{\eta}\sqrt{\frac{\rho}{2G_\infty}}, \tag{2.1.88}$$

or

$$k_{\mathrm{g}} = \frac{1}{\sqrt{2}} \frac{G_\infty}{c^{\mathrm{T}} \eta}. \tag{2.1.89}$$

The wavevector k_{g} sets the characteristic length scale of the fluid: at smaller lengths ($k > k_{\mathrm{g}}$), the fluid's structure is rigid enough for elastic transverse waves to exist, at larger lengths, the equations of hydrodynamics should provide a more appropriate description. The quantities in Eqs. 2.1.88 and 2.1.89 are possible to approximate macroscopically, meaning that this key fluid parameter relates microscopic and macroscopic physics.

Continuum Viscoelasticity

The quantity k_{g} and the transverse elastic waves it admits were a consequence of the finite relaxation of stress, one way or the other. The equations of hydrodynamics describe the evolution of transverse motion as uncoupled to all non-viscous forces in the fluid, and the viscosity itself as a time-independent function of the fluid's state. Writing out Eq. 2.1.20 for the shear stress in our two-variable case explicitly and including the Markovian approximation in Eq. 2.1.80, we see (ignoring the random force):

$$\frac{\mathrm{d}\sigma_{zx}(t, \mathbf{k})}{\mathrm{d}t} = ik \left(\frac{V}{k_{\mathrm{B}} T} \right)^2 G_\infty \, j_x^{\mathrm{T}}(t, \mathbf{k}) + \frac{\sigma_{zx}(t, \mathbf{k})}{\tau^{\mathrm{T}}(k)}, \tag{2.1.90}$$

i.e. the rate of stress is not only proportional to the derivative of the velocity gradients (through the second term on the right), but also the velocity gradients themselves (through the first term on the right). Though we cannot simply integrate both sides, this implies that the *instantaneous* stress depends not only on the velocity gradients, but also on the strain, which is elastic behaviour. This is more difficult to see by including the non-Markovian memory kernel in the integro-differential equation in the single variable case, but it does amount to the same effect.

This effect is called *viscoelasticity*, and was quantitatively described first by Maxwell [37]. There are actually several types of viscoelasticity, as there are several possible ways to combine a viscous and elastic response. We describe two here, and thereby decide which is appropriate to our case of fluids:

Definition 2.1.3 (Maxwell Viscoelasticity) *A Maxwell viscoelastic medium experiences both elastic and viscous strain responses to stress:*

$$\frac{\mathrm{d}\epsilon}{\mathrm{d}t} = \frac{1}{G} \frac{\mathrm{d}\sigma}{\mathrm{d}t} + \frac{1}{\eta} \sigma, \tag{2.1.91}$$

where ϵ is the shear strain, σ is the shear stress, G is the shear modulus, and η is the shear viscosity.

Definition 2.1.4 (Kelvin-Voigt Viscoelasticity) *A Kelvin-Voigt viscoelastic medium experiences both elastic and viscous stress responses to strain:*

$$\sigma = G\epsilon + \eta \frac{\mathrm{d}\epsilon}{\mathrm{d}t}, \tag{2.1.92}$$

where ϵ is the shear strain, σ is the shear stress, G is the shear modulus, and η is the shear viscosity.

A Maxwell material put under a constant shear strain will relax until its shear stresses vanish. Under a constant shear stress, the shear strain will grow for as along as the stress is applied. As the stress is applied and removed, an elastic component to the strain instantaneously responds. In this sense, therefore, the material responds in an elastic manner at short time scales to stress, and a viscous manner at long time scales.

A Kelvin-Voigt material put under constant shear strain will experience a constant shear stress. If the stress is removed from a strained Kelvin-Voigt material, the strain will relax until it vanishes. As the stress is applied and removed, the viscous component instantaneously responds. In this sense, therefore, the material responds in a viscous manner at short time scales to stress, and an elastic manner at long time scales.

From these considerations, we see clearly that our fluids are Maxwell materials. The Laplace transformation of Eq. 2.1.91 is:

$$-z\tilde{\epsilon}(z) = \left(\frac{z}{G} + \frac{1}{\eta}\right)\tilde{\sigma}(z) \tag{2.1.93}$$

which we can compare to the purely viscous stress equation:

$$-z\tilde{\epsilon}(z) = \frac{1}{\eta}\tilde{\sigma}(z),$$

so see that this type of viscoelasticity is equivalent to the replacement of the hydrodynamic viscosity with a frequency-dependent viscosity:

$$\tilde{\eta}(z) = \frac{G}{z + \frac{G}{\eta}}. \tag{2.1.94}$$

Here the *Maxwell relaxation time* has entered:

$$\tau_{\mathrm{M}} = \frac{\eta}{G}, \tag{2.1.95}$$

which is also the time constant of the stress relaxation in Eq. 2.1.91 at constant strain. The quantity introduced in Eq. 2.1.80 can therefore be interpreted as a $k-$dependent Maxwell relaxation time, due to its appearance in the generalised viscosity. Implementing it into the viscosity, and taking the Fourier spectrum:

$$\eta(\omega) = \frac{G}{\left(\frac{\tau_{\mathrm{M}}}{\omega}\right)^2 + 1} \tag{2.1.96}$$

This viscosity becomes approximately elastic when $\omega\tau_{\mathrm{M}} \gg 1$, and approximately hydrodynamic when $\omega\tau_{\mathrm{M}} \ll 1$. Taking the inverse Laplace transformation of Eq. 2.1.93, we have:

$$\sigma(t) = -\int_0^t \mathrm{d}\tau\eta(t-\tau)\epsilon(\tau), \tag{2.1.97}$$

with

$$\eta(t) = G\exp\left(-\frac{t}{\tau_{\mathrm{M}}}\right), \tag{2.1.98}$$

which all looks rather familiar. This makes very comprehensive our microscopic description of transverse collective modes in fluids, as the same phenomenon described from a macroscopic perspective provides the same interpretations in the same mathematical form.

2.2 Frenkel Theory

Using the very deep and abstract formalism of memory functions we have shown that liquids have solid-like properties at short wavelength. This result, and many of the implications which follow, were anticipated by Yakov Frenkel [38] before any of the formalism we used to derive it had been developed. In exploring the intuitive physical meaning of the results of generalised hydrodynamics, we shall set out Frenkel's original work and recent developments of it.

At this point we are capable of saying that the existence of transverse elastic waves in a fluid is on account of relaxation of shear stress on time scales comparable to the frequency of the waves themselves. As to why and how shear stress relaxes, we have no answer yet. The time $\tau^{\mathrm{T}}(k)$ does not follow from the Hamiltonian $\mathscr{H}$, and its macroscopic extension τ_{M} provides no new insight - it is already a ratio of the different responses. Phase space does not operate under the same intuitions as we do, and so the memory function formalism will not give us a satisfactory answer - we postulated that a decaying memory function, or a second slow transverse variable, was appropriate, and we will also have to postulate why.

2.2.1 The Problem of c_V

The heat capacities of simple gases and solids can be deduced by pure reason (*i.e.* counting degrees of freedom). The Dulong and Petit law is trivially recovered by assuming harmonic bonds, giving each atom six quadratic degrees of freedom. This is not so easy for a liquid, where displacements are not small and a quadratic expansion is not appropriate. Instead we decompose the system to its normal modes, of which there are 3 per atom, which correspond to the one longitudinal branch and two transverse branches of collective modes in a monoatomic crystal. A liquid's (apparent) inability to support shear stress leads us to declare that such a decomposition leads us with just one longitudinal branch. In this scheme, the kinetic energy of a branch can manifestly never be zero, so we are left with a heat capacity of $2k_{\mathrm{B}}$. Brillouin was first to recognize the significance of $c_V = 2k_{\mathrm{B}}$ corresponding to the loss of the potential energy of the two transverse mode branches [39]. Since this contradicted the experimental $c_V \approx 3k_{\mathrm{B}}$ of liquids at the melting point, a proposition was made that liquids consist of crystallites with easy cleavage directions so that liquids have $c_V = 3k_{\mathrm{B}}$ and can flow at the same time.

Frenkel came up with another approach to tackle this problem, inspired by his work on defects in solids [38]. Indeed, it is not so different an approach from the crystallite model just described. He accused the atoms themselves of the liquid's ability to flow, by describing the dynamics as follows: atoms adopt an impermanent glassy structure, where at any given time most atoms are vibrating about their quasi-equilibrium positions as they do in a glass or a crystal. An atom spends a characteristic time τ_{F} (which is, for example, on the of the order of a few picoseconds in water at 1 bar and 273 K) oscillating before it abruptly "jumps" to a new quasi-equilibrium position. These jumps are typically faciliated through an atom's neighbours moving in a way that presents a brief opening out of the "cage", rather than an atom receiving enough energy to punch out directly. The result is that the environment of any given atom is approximately static and glassy on timescales less than τ_{F}. A consequence of this model is the ability of liquids to locally support shear stress, albeit only at high frequencies. This is the central result of the Frenkel theory of liquids: at time scales faster than the frequency $\omega_{\mathrm{F}} \approx \frac{1}{\tau_{\mathrm{F}}}$ the liquid behaves like a solid, but at time scales slower than ω_{F} it behaves hydrodynamically. Because high-frequency modes dominate the contribution to the energy, the result $c_V \approx 3k_{\mathrm{B}}$ drops out immediately. The key parameter of the liquid is τ_{F}, and its properties are roughly determined by how close ω_{F} is to the oscillation frequency.

We have shown, however, using our formal theoretical analyses, that the collective modes are gapped in wavevector, rather than frequency. The analysis will be changed, therefore, to make k_{g} the fundamental quantity rather than τ_{F}, but the physical meaning is very similar. Frenkel identified his "hopping" time, τ_{F}, in liquids with the Maxwell relaxation time τ_{M}, an identification which has since become the accepted view [40]. This is an important identification, because the time between atomic rearrangements is a vague concept, not experimentally measureable directly and suffering from ambiguity. The Maxwell relaxation time is much crisper, and the appearance of τ_{M} or k_{g} makes Frenkel's theory very powerful indeed.

Specifically, the heat capacity of a liquid in modern Frenkel theory is modelled as follows [41]. The energy of a liquid can be written as a sum of kinetic energy K^{T} and K^{L} and the potential energy Φ^{T} and Φ^{L} of the transverse and longitudinal collective modes respectively:

$$E = K^{\mathrm{T}} + K^{\mathrm{L}} + \Phi^{\mathrm{T}}(k > k_{\mathrm{g}}) + \Phi^{\mathrm{L}}. \tag{2.2.1}$$

The longitudinal terms can be collected into one term, since the full range of wavevectors is accessible to such modes. Meanwhile, because the kinetic energy of transverse modes in liquids and solids is of course the same, we can use the virial theorem to express K^{T} as half the total energy of transverse modes in a harmonic solid system:

$$E = E^{\mathrm{L}} + \frac{E^{\mathrm{T}}_{\mathrm{solid}}}{2} + E^{\mathrm{T}}(k > k_{\mathrm{g}}). \tag{2.2.2}$$

These contributions can be approximated using integrals over wavevectors:

$$E^{\mathrm{L}}(T) = \int_0^{k_{\mathrm{D}}} \mathrm{d}k \; g^{\mathrm{L}}(k) e(k, T), \tag{2.2.3}$$

$$E^{\mathrm{T}}_{\mathrm{solid}}(T) = \int_0^{k_{\mathrm{D}}} \mathrm{d}k \; g^{\mathrm{T}}(k) e(k, T), \tag{2.2.4}$$

$$E^{\mathrm{T}}_{\mathrm{liquid}}(T) = \int_{k_{\mathrm{g}}}^{k_{\mathrm{D}}} \mathrm{d}k \; g^{\mathrm{T}}(k) e(k, T). \tag{2.2.5}$$

We have made the classical Debye approximation, such that $g^{\mathrm{L}}(k) = \frac{3N}{k_{\mathrm{D}}^3}$ and $g^{\mathrm{T}}(k) = \frac{6N}{k_{\mathrm{D}}^3}$, with k_{D} the Debye wavevector, and $e(k,T) = k_{\mathrm{B}}T$. We will assume the Debye wavevector, insofar as it can be defined in a liquid, is identical to that of a solid, *i.e.* [7]:

$$k_{\mathrm{D}} = \left(6\pi^2 n\right)^{\frac{1}{3}} . \tag{2.2.6}$$

Performing and inserting these integrals into Eq. 2.2.2, we arrive at the following expression:

$$E_{\mathrm{liquid}}(T) = Nk_{\mathrm{B}}T\left(3 - \left(\frac{k_{\mathrm{g}}}{k_{\mathrm{D}}}\right)^3\right), \tag{2.2.7}$$

with corresponding heat capacity

$$C_V = Nk_{\mathrm{B}}\left(3 - \left(\frac{k_{\mathrm{g}}}{k_{\mathrm{D}}}\right)^3\right) - \frac{3Nk_{\mathrm{B}}T}{k_{\mathrm{D}}^3}k_{\mathrm{g}}^2\left(\frac{\partial k_{\mathrm{g}}}{\partial T}\right)_V . \tag{2.2.8}$$

In order to make sense of these statements, we must ponder the evolution with temperature of k_{g}, and therefore τ_{F}. Naturally the period between atomic rearrangements will reduce as temperature increases, as increasing the oscillation amplitude will create more frequent opportunities for a cage escape event. With our identification between τ_{M} and τ_{F}, we can consider this as a loose explanation for the decrease of shear viscosity with temperature increase in liquids. Meanwhile k_{g} increases with increasing temperature, meaning that the lower wavelength modes are erased. This explains the behaviour of the heat capacity of liquids very neatly. Just above the melting point when τ_{F} is large, the energy is close to $3Nk_{\mathrm{B}}T$ and the heat capacity will not be far off $3Nk_{\mathrm{B}}$. The limit of applicability of this equation is when k_{g} approaches the maximum meaningful wavevector, k_{D}, which is on the order of the the reciprocal of the interatomic distance as we can see by inspection of Eq. 2.2.6. In other words, the maximum wavelength at which propagating transverse modes exist approaches the interatomic distance. This means that the liquid rearranges itself microscopically so rapidly that there is no meaningful distance over which it behaves elastically. At this point the energy approaches $2Nk_{\mathrm{B}}T$ and the heat capacity approaches $2Nk_{\mathrm{B}}$.

The evolution of the liquid C_V with temperature now has a crisp physical explanation, backed up both by macroscopic viscoelastic considerations and a formal manipulation of Hamilton's equations: the atomic kinetic energy of a liquid is comparable to the potential energy wells of the interatomic interactions. This opens up the phase space to a certain degree (dependent exactly on how much excess energy there is), which causes the decay of correlations in the stress tensor. This causes the attenuation of some transverse collective modes, and causes others to disappear completely from the spectrum. As the energy increases and the phase space opens out more, the stress decorrelates more quickly and the number of excluded modes increases. The potential energy of such modes, representing a network of atoms energetically connected, therefore decreases, thereby decreasing the system's total number of degrees of freedom. For this reason, the heat capacity of a liquid decreases as a function of temperature.

To conclude this section, we will repeat the derivation of the $k-$gap that Frenkel himself very nearly stumbled upon. As mentioned above, Maxwell viscoelasticity amount to replacing the viscosity η with the operator:

$$\frac{1}{\eta} \to \frac{1}{\eta}\left(1 + \tau_{\mathrm{M}}\frac{\mathrm{d}}{\mathrm{d}t}\right). \tag{2.2.9}$$

What Frenkel did was to insert this operator into the Navier-Stokes equations rather than solving the GLE which it implies. The Navier-Stokes equations governing the evolution of the transverse velocity we defined in 2.1.59 are:

$$\boldsymbol{\nabla}^2\mathbf{v}^{\mathrm{T}} = \frac{\rho}{\eta}\frac{\mathrm{d}\mathbf{v}^{\mathrm{T}}}{\mathrm{d}t}, \tag{2.2.10}$$

Noting that the pressure gradient does not appear in this equation because the curl of a scalar gradient vanishes. We will assume again a fluid not far from equilibrium, such that the partial derivative and material derivative to not appreciably differ from each other. We then insert out viscosity operator:

$$\eta\boldsymbol{\nabla}^2\mathbf{v}^{\mathrm{T}} = \rho\frac{\partial\mathbf{v}^{\mathrm{T}}}{\partial t} + \rho\tau_{\mathrm{M}}\frac{\partial^2\mathbf{v}^{\mathrm{T}}}{\partial t^2}. \tag{2.2.11}$$

If we divide through by τ_{M} and ρ we retrieve:

$$(c^{\mathrm{T}})^2\boldsymbol{\nabla}^2\mathbf{v}^{\mathrm{T}} = \frac{1}{\tau_{\mathrm{M}}}\frac{\partial\mathbf{v}^{\mathrm{T}}}{\partial t} + \frac{\partial^2\mathbf{v}^{\mathrm{T}}}{\partial t^2}, \tag{2.2.12}$$

where $c^{\mathrm{T}} = \sqrt{\frac{G}{\rho}}$ corresponds to the transverse speed of sound, both due to its appearance in the wave equation and its form. The plane-wave solution to Eq. 2.2.12 is:

$$\mathbf{v}^{\mathrm{T}}(t, \mathbf{r}) = \mathbf{v}_0 \exp\left(\frac{-t}{\tau_{\mathrm{M}}} - i\left(\omega t - \mathbf{k}\cdot\mathbf{r}\right)\right). \tag{2.2.13}$$

Insertion of this solution into Eq. 2.2.12 gives the condition for a real frequency:

$$(c^{\mathrm{T}})^2k^2 = \omega^2 + \frac{i}{\tau_{\mathrm{M}}}\omega, \tag{2.2.14}$$

the wavevector at which this gives real solutions is:

$$k_{\mathrm{g}} = \frac{1}{2c^{\mathrm{T}}\tau_{\mathrm{M}}}. \tag{2.2.15}$$

Neglecting the missing factor of $\sqrt{2}$, which is unimportant for considerations as qualitative as ours, we see the same physical quantities in the same form governing the propagation of transverse modes.

The $k-$space gap, as we have now seen, has been derived from several different perspectives, both macroscopic and microscopic. Ultimately, however, all of these approaches describe the same physical truth of liquids, which is that theirs is a *mixed dynamical state*. Atoms do not merely diffuse, nor merely oscillate, but combine the two which gives the liquid simultaneously both fluid and elastic properties. Modern Frenkel theory, as summarised in Ref. [41], not only gives a much more accessible explanation to the gapped momentum state compared to the very abstract and involved derivations of Mori-Zwanzig theory, but also uses it to qualitatively explain the trend of heat capacity in many simple liquids, including noble liquids, molecular liquids, and molten metals [42]. Fitting to experimental of simulated data of c_V is a matter of setting G as a fitting parameter using known measurements of η. This application of Frenkel theory, also called the *phonon theory of liquid thermodynamics* has been rigorously examined [43], and proves to be both falsifiable and successful.

2.2.2 The Frenkel line and the Supercritical State

The importance of the value $c_V = 2k_\mathrm{B}$ is now quite clear to us as the point where a liquid loses all of its elastic properties and, we may guess, becomes purely hydrodynamic with no meaningful oscillations in its atomic motion. It is simple enough to call this state a gas, but what do we really know about the heat capacity of gases? When c_V is near $2k_\mathrm{B}$, the van der Waals equation of state, and therefore cluster expansions, are still not adequate. How does c_V behave in this diffusive fluid? What happens if we take a path on the phase diagram around the critical point, avoiding the boiling line? When does our liquid become a gas? And what is the nature of this transition?

As a starting point, we can certainly identify what contributes to c_V between $2k_\mathrm{B}$ and $\frac{3}{2}k_\mathrm{B}$. When the temperature is not too high, the atoms can still form appreciable transitory bonds which represent a non-negligible proportion of the total energy. Since oscillatory motion is gone in this state, the interactions are dominated by repulsive forces, with very weak contributions from long range attraction. The reduction of c_V as temperature increases further is due to these transitory interactions becoming ever more transitory. At $c_V = 2k_\mathrm{B}$, the atomic motion consists of atoms shifting each other around and sliding off of each other - interactions are still strong but there is no caging and oscillation of atoms on account of attraction. This sliding and shifting transforms into brief collisions as anything but the steepest part of the atomic repulsion becomes incapable of appreciably diverting the system's dominating kinetic energy.

This is true and useful, but does not allow easy comparison to the phonon theory of liquid thermodynamics. Towards that end, we shall rephrase the above using collective modes, as was done in Ref. [41]. The system's Hamiltonian can always be diagonalised in principle, so collective modes of some longitudinal sort can be said to exist. And they too must somehow disappear to explain the drop in c_V. So how do the modes disappear? As we just discussed, the meaningful interactions becomes less and less as temperature increases (or as pressure decreases, for that matter). Another way of seeing things is using the *mean free path*, l_FP, from kinetic theory, which is the mean distance a particle travels before experiencing a collision. Collisions, of course, are poorly defined except in the case of elastic hard spheres, but this is no different from the quantitatively vague concept of τ_F. If l_FP represents the distance an atom travels before it interacts with another, then it can be used to set the minimum wavelength at which collective modes can propagate. If we denote by $k_\mathrm{FP} = \frac{2\pi}{l_\mathrm{FP}}$ the mean free wavevector, we can write the energy as:

$$E^{\mathrm{L}}_{\mathrm{gas}}(T) = \int_0^{k_{\mathrm{FP}}} \mathrm{d}k \; g^{\mathrm{L}}(k) e(k,T), \tag{2.2.16}$$

and therefore

$$E_{\mathrm{gas}}(T) = \frac{3}{2} N k_{\mathrm{B}} T + \frac{1}{2} N k_{\mathrm{B}} T \left(\frac{k_{\mathrm{FP}}}{k_{\mathrm{D}}} \right)^3 . \tag{2.2.17}$$

The approach to the ideal gas is therefore described by the mean free path becoming long enough to exclude all but the very lowest energy, macroscopic collective modes.

Though the application of Debye theory to gases is a bit absurd when it comes to quantitative prediction, it gives us important conceptual insight regarding the heat capacity of liquids and gases. In the liquid state, the increasing frequency of atomic dislocations with increasing temperature reduces the effective range at which the liquid is elastic, thereby reducing the maximum wavelengths at which transverse elastic collective modes can propagate. In the gaseous state, the decreasing frequency of atomic collisions with increasing temperature (at constant pressure) increases the effective range at which the gaseous state is at all self-interactive, thereby increasing the minimum wavelengths at which longitudinal collective modes can propagate. We could associate with these processes mathematical models, but it is readily apparent that these two processes will evolve differently in temperature, as they are very different from each other. What this means is that there is a *crossover* in thermodynamics around the point $c_V = 2k_{\mathrm{B}}$. The evolution of c_V with temperature (or pressure) above $2k_{\mathrm{B}}$ is different from that below $2k_{\mathrm{B}}$. The locus of these crossover points, near $c_V = 2k_{\mathrm{B}}$ coincides with the Frenkel line (FL). Recall that FL denotes the crossover between combined oscillatory and diffusive motion of particles and purely diffusive motion. We can now be more specific about this crossover. Crossing this line corresponds to relaxation time τ_{M} approaching the period of molecular oscillation, or equally the gapped wavevector k_{g} approaching the maximum wavevector of the system, the Debye wavector k_{D} as we saw above.

All these criteria correspond to the physical phenomenon of molecular oscillation giving way to purely diffusive motion. As the fluid increases temperature or decreases pressure, particles spend less time oscillating relative to diffusing and therefore the fluid state evolves from a mixed dynamical state where oscillation and diffusion are both present to a pure dynamical state where only diffusive motion remains. Hence there is a line on the (P, T) phase diagram with positive slope across which there is a crossover in dynamics and in thermodynamics. This line exists in the supercritical state because there the boiling line is no more and the transition from a liquidlike to a gaslike state is continuous. Across the boiling line, the same transition in dynamics and thermodynamics occurs, but the FL is absent because the transition is part of the boiling transition.

The thermodynamic criterion for the FL is straightforward, but the basis for the thermodynamic crossover is of course dynamical. The dynamical definition of the FL is constructed using the velocity autocorrelation function (VAF), $Z(t)$. This is the autcorrelation of the single particle velocity, $\mathbf{v}$. The mean can be a phase mean, or a mean over all particles - these means will coincide in the thermodynamic limit. Mathematically:

$$Z(t) = \langle \mathbf{v}(t) \cdot \mathbf{v}(0) \rangle . \tag{2.2.18}$$

Minima and maxima in the VAF represent the tendency of a particle to change the direction of its motion, and therefore are indicative of oscillation. The disappearance of minima from the VAF therefore presents an approximate dynamical functional definition of the FL. These two criteria closely coincide for simple systems which are nearly harmonic [23].

The FL separates fluid states not only on the basis of particle dynamics and thermodynamics, but also structure. The argument for this claim is simple. We introduce the radial distribution function, $g(r)$, which measures the relative probability of a given particle being found at a distance r from another particle. Its definition is:

$$ng(r) = \frac{1}{N}\sum_{i\neq j}\langle\delta(\mathbf{r}-\mathbf{r}_{ij}),\rangle \tag{2.2.19}$$

such that $ng(r)$ is the mean number of particles at a distance r from a given particle. This quantity is related to the the Fourier transformation of the static structure factor, which measures the static periodicity:

$$S(k) = 1 + n\int_0^\infty \mathrm{d}\mathbf{r}\,(g(r)-1)\exp(-i\mathbf{k}\cdot\mathbf{r}). \tag{2.2.20}$$

Here we must use $g(r)-1$ so that the integral converges, and we have left off a factor of $n\delta(\mathbf{k})$ which is experimentally inaccessible anyway. We furthermore see that the number of particles at a distance r from an atom is given by $4\pi r^2 ng(r)$. Using this, we can use $g(r)$ to write down the potential energy of a system with pair interactions $\phi(r)$:

$$\Phi = 4\pi nN\int_0^\infty \mathrm{d}r r^2 g(r)\phi(r). \tag{2.2.21}$$

Since the kinetic contribution to energy is immutable in form, any crossover in the thermodynamics necessitates a crossover in structure too, via the radial distribution function in simple fluids.

The Frenkel line therefore represents a rather extensive transition between liquidlike and gaslike states, and it operates in the supercritical state where such transitions are traditionally supposed to be absent [44]. The nature of the transition across the FL is currently not very well understood. Indeed, the transition across the FL is effectively the same as that across the boiling line except for its abruptness: particle dynamics, density, heat capacity *etc.* all sharply change upon evaporation, but at the FL the transition is apparently smoother as the number of transverse modes smoothly drops to zero. However, the FL doesn't emerge from the critical point, it instead emerges from the boiling line at about 0.8 T_c, where T_c is the critical temperature. The boiling line itself branches away from the melting and sublimation lines at the triple point, so the meeting of the FL with the boiling line below the critical point is an interesting phenomenon that shows how poorly the near-critical and supercritical states are understood. The region between the FL and boiling line is better understood as a dense gas (much like how the supercritical state is often pictured) and the boiling line at these conditions is a 1st order phase transition between two gaslike states [45]. Unlike the boiling line and sublimation lines, and like the melting line, the FL extends to arbitrarily high temperatures and pressures as long as the system remains chemically unaltered. This is in contrast to the Widom line, which does not extend further than about three times the critical temperature. Furthermore, the FL is path independent, whereas the maximum in c_P or other properties depends on the path taken through the phase diagram. The FL therefore presents a definition of and distinction between liquid(like) and gas(like) states at conditions far more extreme than those we experience in everyday life.

One of the early motivations for the FL was the phenomenon called "fast sound", or positive sound dispersion (PSD). PSD is phenomenon where the speed of sound increases beyond its hydrodynamic value at large wavevectors. This is related to the propagation of transverse modes: the mixing of transverse and longitudinal excitations causes an increase of the speed of sound from $\sqrt{B/\rho}$ to $\sqrt{(B+4/3G)/\rho}$ at higher wavevectors. The phenomenon was indeed predicted by Frenkel [2], though on the bases of frequency father than wavevector. Experimental evidence for the structural crossover across the FL has been gathered in supercritical neon [46], dinitrogen [47], methane [48], and subcritical ethane [49]. The thermodynamic crossover has been approached on the basis of modelling [50], but still largely remains a mystery. This work will concentrate heavily on these crossovers at the FL, structural, thermodynamic, and others more subtle.

Chapter 3

Molecular Dynamics

We concluded our discussion of transverse collective modes in liquids with a macroscopic connection, but the fact remains that many key properties of liquids cannot be measured directly by experiments, or even at all. To this date, the gapped momentum spectrum predicted in the liquid transverse sector has not been seen experimentally. Immediately with the advent of computers, physicists realised the potential they had to illuminate the liquid state, with its chaotic dynamics and amorphous structure [51]. Indeed, such simulations are sometimes called “computer experiments”, revealing the crucial revelatory aspect of these simulations. A discussion of the place this “third part” of empirical science occupies is best left for another time, however. There are two primary methods of molecular simulations. *Monte Carlo* simulations involve sampling phase space configurations according to a postulated phase space probability density (usually the isothermal-isochoric or isothermal-isobaric ensembles) in order to generate statistical moments of phase functions. Based on the dynamical picture of liquids I have expounded in the previous sections, it should be clear that this technique leaves much to be desired. On the other hand, *Molecular Dynamics* simulations, deals with both structure and dynamics. These are the simulations which we will focus on here.

3.1 Integration Algorithms

Molecular dynamics is, in a phrase, the numerical solution of a many-body classical mechanical system. A simple statement for a bold proposition. Though computing power has increased a great deal, so too have our ambitions. The evolution of a classical system is governed by the interchange of energy between kinetic and configurational forms. Velocity drives particles through space, and the interparticular interactions make changes to this velocity. The phase space increases in dimensionality by 6 per particle in our system (neglecting constraints), and in order to produce a faithful description of a state of matter one needs to simulate, at the very least, many dozens of particles. This renders Newton’s, Lagrange’s, and Hamilton’s equations of motion insoluable except using an algorithmic finite-difference approach: we evolve the system through phase space in discrete steps for as long as we please. As always in finite difference methods, we must make a choice between optimising speed of execution or accuracy and stability of the solution. The most obvious discretisation of Newton's equations is the *forward Euler method*:

$$\mathbf{r}_i(t+\delta t) = \mathbf{r}_i(t) + \mathbf{v}_i(t)\delta t, \tag{3.1.1}$$

$$\mathbf{v}_i(t+\delta t) = \mathbf{v}_i(t) + \mathbf{a}_i(t)\delta t. \tag{3.1.2}$$

Here $\mathbf{r}_i, \mathbf{v}_i, \mathbf{a}_i$ are the position, velocity, and acceleration of the ith particle. This method is called a first order method, because we have truncated the Taylor series at first order, and the error of our approximation is proportional to terms of order δt^2 and above. In practice, this method is unacceptable for use. It's unstable - no matter how small the δt, it will always diverge from the true solution. Physically, it doesn't conserve energy well and is not symplectic (it doesn't preserve the phase space volume, violating Liouville's theorem). Another method is computationally not too much more expensive, but vastly more accurate and stable. This is the *velocity Verlet* method.

$$\mathbf{r}_i(t+\delta t) = \mathbf{r}_i(t) + \mathbf{v}_i(t)\delta t + \frac{1}{2}\mathbf{a}_i(t)\delta t^2, \tag{3.1.3}$$

$$\mathbf{v}_i(t+\delta t) = \mathbf{v}_i(t) + \frac{1}{2}\left(\mathbf{a}_i(t) + \mathbf{a}_i(t+\delta t)\right). \tag{3.1.4}$$

The trajectories generated with this method are accurate up to order of δt^3, time reversible, and preserve the phase space volume. These equations, or equivalent reformulations, are frequently used in molecular dynamics simulations because of these properties.

3.2 Potentials

The terms $\mathbf{a}_i(t)$ in Eqs. 3.1.3 and 3.1.4 look innocuous but are the source of the most number crunching when it comes to implementation. As per Hamilton's equations, we must know the gradient function of the configurational (potential) energy term, $\Phi\left(\{\mathbf{r}_i\}\right)$, such that

$$m_i\mathbf{a}_i(t) = -\sum_{j\neq i}^{N} \frac{\partial \varphi(\mathbf{r}_{ij})}{\partial \mathbf{r}_{ij}}, \tag{3.2.1}$$

with m_i the particle mass. For computational efficiency, one usually introduces a "cutoff" distance, above which contributions to the sum in Eq. 3.2.1 are ignored. Choosing the potential is not a trivial task. Indeed, how would one even begin to discern how different sorts of atoms should interact with each other microscopically? There are a few things we can know for sure. The first is that there must be a strong repulsive term. This we know effectively *a priori*, as the stability of atomic matter requires such a term to be present. Physically we understand this term to have its origins in the energy cost associated with the Pauli exclusion principle when electron orbitals occupy overlapping space. The second is an attractive term, which is easily inferred from the fact that atomic matter is unerringly cohesive under at least some conditions. The third is the electrostatic term, of which we know the form, but the partial charges of atoms are not so obvious. Finally, we know that bonded interactions must exhibit stronger cohesive forces as separation increases, as opposed to non-bonded interactions, such that the atoms do not spontaneously dissociate.

The simplest potential one can imagine is the *hard sphere potential*:

$$\varphi_{\mathrm{HS}}(r) = \begin{cases} \infty, & r \leq \sigma \\ 0, & r > \sigma, \end{cases} \tag{3.2.2}$$

where σ is the atomic radius. This is a problematic potential, however, due to the discontinuity. We much prefer to use the *soft sphere potential*:

$$\varphi_{\mathrm{SS}}(r) = \epsilon \left(\frac{\sigma}{r}\right)^n, \tag{3.2.3}$$

where ϵ is often called the *interaction* strength, and n is typically an integer. The hard-sphere potential is of course the limit of $n \to \infty$. No thermodynamically stable phases are found for $n \leq 3$. The soft sphere potential might be acceptable from sparse gaseous or supercritical phases, but the lack of an attractive term means that it cannot model any cohesion and is inappropriate for denser states. The most famous interaction which incorporates cohesion is the *Lennard-Jones potential*:

$$\varphi_{\mathrm{LJ}}(r) = 4\epsilon \left(\left(\frac{\sigma}{r}\right)^{12} - \left(\frac{\sigma}{r}\right)^{6}\right). \tag{3.2.4}$$

The Lennard-Jones potential alone can acceptably model noble fluids such as argon ($\epsilon \approx 120 k_{\mathrm{B}}$, $\sigma \approx 3.4\mathring{A}$), but is a popular choice to measure the weak, so-called "van der Waals" forces which exist even between ions. A sometimes superior choice is the *Buckingham potential*:

$$\varphi_{\mathrm{Buck}}(r) = \epsilon \left(\frac{6}{\alpha - 6} \exp\left(\alpha\left(1 - \frac{r}{\sigma}\right)\right) - \frac{\alpha}{\alpha - 6}\left(\frac{\sigma}{r}\right)^{6}\right). \tag{3.2.5}$$

This potential is also formulated as:

$$\varphi_{\mathrm{Buck}}(r) = A \exp\left(-\frac{r}{\rho}\right) - \frac{C}{r^6}. \tag{3.2.6}$$

Although the Buckingham potential may model certain interactions better, it exhibits a strong attraction at small distances. If, when simulating, an atom pair overcomes the barrier, the atoms will accelerate towards each other at an ever-increasing rate and spoil the trajectory.

Electrostatic interactions are tricky, because they are long range. In molecular dynamics, if we want to simulate the bulk of a material, it is much more efficient to use periodic boundary conditions, rather than simulating an enormous isolated system and only gathering data far from its surfaces. In order to do this, the minimum image convention [52] is a popular choice: the simulation cell is repeated on all sides, and each atom only interacts with the nearest "image" (of which there are 6 in three dimensions) of any other given atom. Such a procedue demands that we set the cutoff of interactions (which is a computational convenience we should wish to employ nonetheless) as no larger than half the simulation cell width. However electrostatic forces do not decay quickly, requiring us to be careful with periodic boundary conditions and cutoffs. The

Ewald sum is a technique for dealing with long range periodic electrostatic interactions [53]. To the electrostatic term, a sum of pair energies, one introduces "smeared out" Gaussian distributions of charges, one set with charges equal to physical charges and with opposite charges, such that the physical situation is unchanged. However, if the physical point charges are paired with the fictitious opposite-charge Gaussian distributions, one has split the total electrostatic energy into a short range and long range term, the latter of which is of course short range in reciprocal space. This technique allows for rapid convergence of energy compared to a calculations totally in real space.

Parametrising these potentials can be done in two ways for the most part. The first is comparison to pertinent experimental data, and optimising parameters with a sensible automated scheme. If we're interested in the structural correlations we don't need to fit dielectric permitivitty data, but we should aim to get density and the structure factor right at least somewhat near the target pressure and temperature. Of course there is a certain futility to such a method, because the adequate amount of data needed to fit a certain model for a certain task is the exact data which would make the molecular dynamics study unnecessary. In practice, the extrapolations of such schemes do an admirable job. The other way to parametrise these potentials is using so-called *ab initio* methods, such as density functional theory, which solve the Schrödinger equation of the system of interest in order to characterise its electronic structure. A combination of these methods is often the best approach.

In this thesis, I perform molecular dynamics simulations of water, carbon dioxide, and argon in their liquid, supercritical, and gaseous states. The potential used for water is TIP4P/2005 which is a rigid, four-site potential. This means it consists of four "sites", one for each of the real atom in the molecule, and one fictitious atom between the oxygen and hydrogen atoms. The real atoms are massive, but the oxygen carries no charge, and the fictitious atom is massless but is negatively charged, which represents the discrepancy between the charge and mass distributions in water better than a 3-site module would. The hydrogen atoms only interact via their charge, but the oxygen atoms also have a Lennard-Jones interaction, as in Eq. 3.2.4, amongst themselves. The parameters of this potential are supplied in Tab. 3.1. These atoms are all rigid with respect to each other, meaning that the bond lengths and angles are fixed. Though the H-O-H bond angle is rather floppy at high temperature, the FL is an intermolecular phenomenon, so I was content to use the FL predicted by the rigid potential in order to begin. This potential was parametrised with structure and high pressure and temperatures in mind [54]. This potential is one among many for water, of course, and was assigned the highest score by a detailed review which compared the most popular water potentials to experimental data [55, 56]. This potential was also used in a recent molecular dynamics study of the Widom line in water [57]. Though a rigid-body potential omits many aspects of water's behaviour such as vibrational contributions to structure, the optimisation of the potential against experimental results is designed to compensate for this, such that the properties of the simulated water still closely match those of real water. The rigidity of the TIP4P/2005 potential makes it rather quick to simulate, at least for a system with charges where the necessity of Ewald summation slows things down.

The potential used for carbon dioxide was a rigid body potential, like that of water, with carbon-carbon, oxygen-oxygen, and carbon-oxygen van der Waals forces modelled

Parameter	Value
Oxygen mass (amu)	16.00
Hydrogen mass (amu)	1.00
S (fictitious atom) mass (amu)	0.000
Oxygen charge (e)	0.000
Hydrogen charge (e)	0.5564
S (fictitious atom) charge (e)	-1.113
ϵ_{OO} (eV)	0.008031
σ_{OO} (Å)	3.159
O-H bond distance (Å)	0.9572
O-S bond distance (Å)	0.1546
H-O-H bond angle (deg)	104.5
H-O-S bond angle (deg)	52.25

Table 3.1: Potential parameters used in molecular dynamics simulations of water. ϵ_{OO} and σ_{OO} refer to the Lennard-Jones parameters between the oxygen atoms, as per Eq. 3.2.4.

using the Buckingham potential as seen in Eq. 3.2.5 and with partial charges on the carbon and oxygen atoms calculated from *ab initio* methods and compared to experimental data, including equations of state and phonon dispersion curves [58]. Again, as the FL is an intermolecular phenomenon and carbon dioxide is a compact molecule, using a rigid body potential is an acceptable approximation for a first study. Note that here all three sites carry comparable mass and interact with each other via their electric charges *and* via the Buckingham potential. This is in contrast to water where the molecule is dominated by the oxygen atom with its larger mass and sole participation in van der Waals interactions.

The potential used for argon was simply the Lennard-Jones potential described in Eq. 3.2.4. Argon, as a noble element, has very weak interatomic interactions, which allows it to be modelled just using the Lennard-Jones potential between the single atom sites, considerably speeding up calculations.

3.3 Gathering Data

Once we've decided on our potential, we have our Hamiltonian. We can then integrate it, using our Verlet algorithm, to generate what we call a *trajectory*, a curve through phase space. But a trajectory is not the fundamental quantity of statistical mechanics, rather the probability density. How can we gather a probability density when we can only access solutions to Hamilton's equations one at a time? Boltzmann was the first to address this issue, and more or less postulated that one can access the probability density from a single trajectory. In typical Boltzmann fashion, however, he left this assumption rather implicit and it was Ehrenfest who gave it its name, the *Ergodic Hypothesis*.

Parameter	Value
Carbon mass (amu)	12.00
Oxygen mass (amu)	16.00
Carbon charge (e)	0.6081
Oxygen charge (e)	-0.3040
Hydrogen charge (e)	0.5564
A_{CC} (eV)	1123
A_{CO} (eV)	1979
A_{OO} (eV)	2110
ρ_{CC} (Å)	0.2778
ρ_{CO} (Å)	0.2637
ρ_{OO} (Å)	0.2659
C_{CC} (eV Å^6)	0.000
C_{CO} (eV Å^6)	12.61
C_{OO} (eV Å^6)	22.28
O-C bond distance (Å)	1.156
O-C-O bond angle (deg)	180.0

Table 3.2: Potential parameters used in molecular dynamics simulations of carbon dioxide. A_{CO} refers to the Buckingham parameter between the carbon and oxygen atoms, as per Eq. 3.2.6, and so on for A_{CC}, ρ_{CO} and so on.

Parameter	Value
mass (amu)	39.95
ϵ (eV)	0.01032
ϵ (K)	119.65
σ (Å)	3.4

Table 3.3: Potential parameters for argon used in the molecular dynamics simulations.

Hypothesis 3.3.1 (The Ergodic Hypothesis) *The ergodic hypothesis states that the time average of any phase function over a single trajectory, in the long time limit, is equal to the phase average of that function:*

$$\lim_{\tau\to\infty}\frac{1}{\tau}\int_0^\tau \mathrm{d}t\ A(t) = \int \mathrm{d}\Gamma\ A(\Gamma). \tag{3.3.1}$$

Sometimes the hypothesis is extended further, stating that any given trajectory explores all of phase space in a uniform manner, given enough time. In other words, there is only one trajectory through phase space, covering it completely. A moving thought, I think. This of course certainly brings about Eq. 3.3.1 in the microcanonical case, and it's difficult to imagine another physical justification for this equation, but some authors like to keep the distinction.

Ergodicity, the state of being ergodic, can be motivated with a nice intuitive physical explanation. The evolution through phase space of real systems is nonlinear, and therefore dynamically unstable. In other words, a small perturbation in the positions of momenta of particles will cause a rapid divergence from the unperturbed trajectory, due to the very many terms driving the evolution of each atom. This means that a trajectory is always very quickly decorrelating with its neighbours in phase space. This suggests, firstly, that a uniform phase space probability density will very rapidly extend throughout phase space (though due to Liouville's theorem its total measure will remain unchanged), and, secondly, that any given trajectory will likely visit any given subset of phase space of nonzero measure. It's not that simple, from a rigorous point of view, as dynamical instability is a necessary but not sufficient condition for ergodicity, but it does motivate us to give it a try.

With the ergodic hypothesis in hand, we can now start doing statistical mechanics with our molecular dynamics trajectories. We take means of phase functions over our trajectories, which is performed as follows:

$$\langle A(\Gamma)\rangle = \sum_{i=1}^{m}\frac{1}{m}A(\Gamma(i\times\delta t)), \tag{3.3.2}$$

where m is the total number of timesteps we generate for the trajectory. In order that we may generate good statistics, we must generate long trajectories with very many timesteps. There isn't much more to it, as all we need in statistical mechanics is various statistical moments. A common tactic used to modify Eq. 3.3.2 is to only take every n^{th} timestep when constructing the average, which saves on computational power and storage space. The ergodic hypothesis doesn't guarantee this is possible, though it would be a rather contrived phase space which forbade it. We collect as often as we need to such that the average isn't affected by the reduced sampling, and no more often than that. TCFs are calculated as follows:

$$\langle A(n\times\delta t)B(0)\rangle = \sum_{i=1}^{m-n}\frac{1}{m-n}A((i+n)\times\delta t)B(i\times\delta t). \tag{3.3.3}$$

This is all well and good, but in statistical mechanics we use different ensembles to calculate different quantities conveniently. How can we make our single phase space trajectory correspond to these ensembles? The symplectic equations of motion of the Verlet integrator are very attractive when modelling isolated systems. We know them to be accurate insofar as we have faith in the applicability of Hamiltonian mechanics to our system. While much effort and progress have been recently made in understanding the relationship between open systems and equilibration [59], how exactly we ought to represent such effects in molecular dynamics simulations is not clear.

We typically begin a molecular dynamics simulation, of fluids at least, by seeding a Maxwell velocity distribution at the target temperature in an initial configuration. Such an initial configuration is likely not to be close to an equilibrium configuration at the target temperature, so letting the system evolve for a while until it reaches the "main sequence" of its energy hypersurface is good practice. The temperature (defined using equipartition in Hamiltonian systems [52]) may have drifted unacceptably far from the target temperature by this time, however, so we may wish to reseed the velocities, now with a configuration closer to equilibrium. This process may be repeated a few times. Temperature is hard to control precisely using this method, but if that isn't a problem, it's an acceptable way to gather data at a fixed temperature and density. The ergodic hypothesis states that the resulting trajectory we collect from will give us a *microcanonical mean*, which does not correspond to a typical experimental setup. This is unimportant, however, because in the thermodynamic limit, all ensembles coincide [7] and therefore our small microcanonical simulation will give us valuable data pertaining to an open macroscopic real system, provided we can simulate it at the right energy and volume.

But what if we want to finely control the temperature, pressure, or even apply nonhydrostatic stress? Such things are not really possible to do in microcanonical simulations where the best we can do is set up an initial velocity distribution at a density and let it do its own thing. Are there constraints we can place on the equations of motion, transforming our system into a non-Hamiltonian one, which will change the constants of motion? There are, and such modifications to the equations of motion are called *thermostats* and *barostats*.

The first thermostat we will examine is arguably the simplest, the *Berendsen thermostat*. It is a slightly less jarring form of the velocity reseeding we described above. We introduce a scaling factor, $\chi(t)$, by which we multiply the velocities at each timestep:

$$\chi(t) = \left(1 + \frac{\delta t}{\tau}\left(\frac{\frac{3}{2}Nk_{\mathrm{B}}T}{K(t)} - 1\right)\right)^{\frac{1}{2}}, \tag{3.3.4}$$

where K is the instantaneous kinetic energy, T is the target temperature, and τ is a specified time constant which sets the "strength" of the thermostat. In the case of constrained particles, such as diatomic molecules, the $\frac{3}{2}$ factor will of course have to be modified. The dynamics otherwise proceed as per Hamilton's equations. This thermostat therefore behaves as a universal damping (or augmenting, as it can also increase the velocities) force which drives the system's kinetic energy towards a target. This thermostat suppresses kinetic energy fluctuations and unsurprisingly therefore does not cause the system to sample canonical trajectories, and indeed the thermostat will drain energy from high frequency modes. This violation of equipartition is called the "flying ice cube effect" due to the deposition of energy into low frequency modes such as centre-of-mass translation [60].

There are two thermostats which cause a trajectory to sample canonical dynamics. The first is the *Nosé-Hoover thermostat* [52]. This thermostat makes a modification to the Hamiltonian, adding two new variables, η and its "momentum" p_η:

$$\mathscr{H}' = \mathscr{H} + \frac{p_\eta^2}{2Q} + 3Nk_{\mathrm{B}}T\eta, \tag{3.3.5}$$

where Q is a parameter which again sets the thermostat's strength. Although this is the Hamiltonian preserved under Nosé-Hoover dynamics, these new variables are non canonical, *i.e.* they do not preserve the form of Hamilton's equations. The new equations of motion are:

$$\begin{aligned}
\frac{\mathrm{d}\mathbf{r}_i}{\mathrm{d}t} &= \frac{\mathbf{p}_i}{m_i} \\
\frac{\mathrm{d}\mathbf{p}_i}{\mathrm{d}t} &= \mathbf{F}_i - \frac{p_\eta}{Q}\mathbf{p}_i \\
\frac{\mathrm{d}\eta}{\mathrm{d}t} &= \frac{p_\eta}{Q} \\
\frac{\mathrm{d}p_\eta}{\mathrm{d}t} &= \sum_{i=1}^{N} \frac{\mathbf{p}_i^2}{m_i} - 3Nk_{\mathrm{B}}T.
\end{aligned} \tag{3.3.6}$$

So we see that the new, non-canonical "momentum" p_η, is driven by the discrepancy between the instantaneous temperature and the target temperature, and in turn decides the sign and magnitude of the friction term in the evolution of $\mathbf{p}_i$. The variable η seems spurious in the evolution of the system itself, but is important for analyses of the phase space probability density [52], an interest we can sympathise with.

The second thermostat which creates canonical dynamics is the Langevin thermostat. This thermostat is easily motivated from a physical point of view: the effect of an environment on an open system (whose own microscopic degrees of freedom are inaccessible to us) is inevitably stochastic. And as we have seen, such random variables also produce a damping term. Mathematically, the Fokker-Planck equation corresponding to the (Markovian) Langevin equation has an equilibrium solution which is a Gaussian with width determined by the fluctuation strength. This thermostat therefore couples each particle's momentum to a fictitious dissipative and fluctuating heat source. The equations of motion become [61]:

$$\begin{aligned}
\frac{\mathrm{d}\mathbf{r}_i(t)}{\mathrm{d}t} &= \frac{\mathbf{p}_i(t)}{m_i} \\
\frac{\mathrm{d}\mathbf{p}_i(t)}{\mathrm{d}t} &= \mathbf{F}_i - \gamma\mathbf{p}_i(t) + \boldsymbol{\xi}_i(t) \\
\langle \boldsymbol{\xi}_i(t)\boldsymbol{\xi}_j(\tau)\rangle &= 2\gamma k_{\mathrm{B}}T\delta_{ij}\delta(t-\tau)\mathbf{I}^{(2)}.
\end{aligned} \tag{3.3.7}$$

Here $\boldsymbol{\xi}$ is a random force vector, γ is a friction constant, $\mathbf{I}^{(2)}$ is the second rank isotropic tensor, and δ_{ij} is the Kroncker delta.This themostat drives the system on a local scale - particles receive or release heat to the heat source based on whether they are too "hot" or "cold" compared to the target temperature. It also has the advantage of dispersing numerical instabilities because of the stochastic influence.

Each of these thermostats has an associated barostat which controls drives the system towards the target pressure. The Berendsen barostat works much like the thermostat. We introduce the factor $\eta(t)$, by the cube root of which we scale the system's coordinates:

$$\eta(t) = \left(1 - \frac{\delta t}{\tau}\right)(P - P(t)). \tag{3.3.8}$$

Here $P(t)$ is the instantaneous pressure (calculated from the trace of the stress tensor) and P is the target pressure. Again τ is a relaxation time which sets the strength of the barostat's compression and expansion. The Nosé-Hoover and Langevin barostats work by introducing auxiliary variables and inserting them into the equations of motion for the momenta and positions [62, 63]. These are much more complicated and we have little to gain by explicating them.

Using these thermostats and barostats we can comfortably equilibrate a system at the thermodynamic conditions we please. Furthermore, if we're using Langevin or Nosé-Hoover integration algorithm, we can simply perform our production run with these dynamics and perform analysis on the resultant trajectory. This allows us to control temperature and pressure with very fine precision when we do our calculations, and ensure that our trajectory samples the ensemble of our choice. In this thesis, we use the microcanonical (NVE), canonical (NVT), and Gibbs (NPT) ensembles, where the labels in brackets are commonly used to describe the thermodynamic quantities held constant in such ensembles. We also note that some quantities are more convenient to calculate in a given ensemble. For example, the isochoric heat capacity, ever on our minds, is easy to write in the canonical ensemble:

$$c_V = \frac{\langle E^2\rangle - \langle E\rangle^2}{N k_{\mathrm{B}} T^2}. \tag{3.3.9}$$

There exists a method of calculating quantities in one ensemble when they are known in another. If we wish find an expression relating the mean of the phase variable A in the ensemble where F is held constant and the one where its thermodynamic conjugate f is held constant, we use the following formula:

$$\langle A\rangle_F = \langle A\rangle_f + \frac{1}{2}\frac{\partial}{\partial f}\left(\frac{\partial f}{\partial F}\right)\frac{\partial}{\partial f}\langle A\rangle_f, \tag{3.3.10}$$

where F as a function of f is given by $F = \langle F\rangle_f$. The formula in the case of a covariance is [53]:

$$\begin{aligned}\langle (A - \langle A\rangle_F)(B - \langle B\rangle_F)\rangle_F = {}& \langle (A - \langle A\rangle_f)(B - \langle B\rangle_f)\rangle_f \\ &+ \frac{\partial f}{\partial F}\left(\frac{\partial}{\partial f}\langle A\rangle_f\right)\left(\frac{\partial}{\partial f}\langle B\rangle_f\right).\end{aligned} \tag{3.3.11}$$

In the example of C_V, we can calculate the variance of the kinetic energy K microcanonical ensemble as a function of its analytically calculable form in the canonical ensemble to get the following expression:

$$c_V = \frac{3}{2} k_{\mathrm{B}} \left(1 - \frac{\langle K^2 \rangle_{NVE} - \langle K \rangle_{NVE}^2}{\frac{3}{2} N k_{\mathrm{B}}^2 \langle T \rangle_{NVE}^2} \right)^{-1} . \tag{3.3.12}$$

All molecular dynamics simulations in this work, unless otherwise specified, have been performed with the DL_POLY package [64].

Chapter 4

Water

4.1 The Most Studied Compound in Science

As discussed, crossovers in thermodynamics, intermolecular structure, and intramolecular dynamics have been observed in a variety of different liquids, including noble liquids, molecular liquids, and molten metals. Water, H_2O, is very different from and more interesting than (depending on whom you ask) all of these other liquids, for a variety of reasons. Water is a small molecule, and indeed light, composed of oxygen and hydrogen. Oxygen is one of the most electronegative elements so far discovered or synthesised, which gives water a rather strong dipole. These two properties combine to make water a small, light, strong dipole, making its electrostatic properties very prominent. The hydrogen bonds of water, which are a static representation of the attraction between protons and electronegative sites in polar molecules, are therefore, though not the strongest of any compound, nonetheless very strong. It is this extra energetic contribution which gives water its famous tetrahedral structure. This tetrahedral structure, deviations from it, and the hydrogen bonds which cause it, are the source of many anomalies in the crystalline, glassy, liquid, supercooled, and supercritical states which have inspired research for over a century and continue to do so [65, 66]. On account of these anomalies, however, water is not an ideal system to test fundamental theoretical prediction such as those of the FL - it's entirely possible, wondering *a priori*, that the complicated energetics and anomalies of water would serve to obscure the crossover at the FL.

This having been said, supercritical water in particular is an exciting area of ongoing research. Little is known about the supercritical state, despite its increasing deployment in important industrial and environmental applications [17, 26, 27]. In particular, supercritical water is used for chemical extraction, biomass decomposition, dyeing and chromotography, biodiesel production, as a chemical reaction catalyst and reagent, toxic and hazardous waste processing and environmentally-friendly dissolving and cleaning, among many other applications.

Experiments at high pressures and temperatures are challenging in water, and so compared to subcritical experiments, experiments in supercritical water are rather scarce. Water was studied in x-ray diffraction experiments close to the melting line, therefore below the FL, up to 17 GPa and 850K [67]. Neutron scattering experiments on water in the supercritical state probed states below and above the FL, though these points were rather scattered and sparse [68], precluding a systematic study of the structure of water across the FL. Another x-ray study, before either of the previous experiments were performed, studied the RDFs of water along the 1kbar isobar from below to above the critical temperature. These points, as well as the state points simulated in this work, are plotted in water's phase diagram in Fig. 4.1. At higher temperatures and pressures, water is known to lose its characteristic tetrahedral structure and adopt a more closely packed structure typical of a "simple" liquid such as argon [67, 69, 70, 71]. The loss of the hydrogen-bonded network results in a loss of many of water's unique properties, and this transition is known to occur in the supercritical state [69].

4.2 Molecular Dynamics Simulations

Previous work on the FL in water was performed using molecular dynamics simulations of the TIP4P/2005 potential [72], The work in this chapter [74] was performed following this identification of the FL. The FL in TIP4P/2005 water is shown, as an interpolated curve, in Fig. 4.1, data having been taken from Ref. [72]. Along the six primary isobars on which we will be concentrating, the FL occurs at the following state points: (0.5 kbar, 515 K), (1 kbar, 525 K), (2.5 kbar, 550 K), (5 kbar, 580 K), and (10 kbar, 680 K). The critical point of water is (0.22 kbar, 647K), which is more pressurised and hotter than many other liquids, on account of water's strong energetics. The FL therefore doesn't cross the critical temperature until almost 10 kbar, however 1kbar and 5 kbar are 5 and 25 times the critical pressure, so we do not expect near critical anomalies such as those associated with the Widom line to have a significant impact on water at these conditions. Furthermore, these conditions correspond to temperatures much higher than the melting line and pressures much higher than the boiling line and critical pressure, so we can consider these conditions to be deeply supercritical.

A system of 3350 TIP4P/2005 water molecules was prepared in an unphysical cubic lattice initial configuration. Because of our aspirations of the supercritical state, we have no need to create an initial structure corresponding to any type of ice. This initial configuration is seeded with a Gaussian velocity distribution at the target temperature, and then heated and pressurised to the target temperature and pressure using the Langevin thermostat and barostat, with 1.0 ps relaxation times to both. These equilibration runs lasted for 30,000 timesteps of 1 fs, for 30 ps of equilibration time in total. During the last 15000 timesteps, the system volume was collected and used to generate the mean density at each state point (plotted in Fig. 4.1b). The mean densities were used to create initial conditions at the target volume, again in a cubic lattice. These pressurised systems were then subject to production runs in the NVE ensemble, after using velocity scaling to melt and equilibrate the lattices. These production runs lasted for 170,000 timesteps, or 170 ps. The NVE ensemble is often preferred because it has nice "realistic" dynamics, without any arbitrary choice of thermostat having been made. However, I also took the final configurations of the equilibration runs, and used them as the initial configurations (without any modification) of a second round of production runs, this time again in the NPT ensemble with the Langevin thermostat and barostat. This controlled temperature

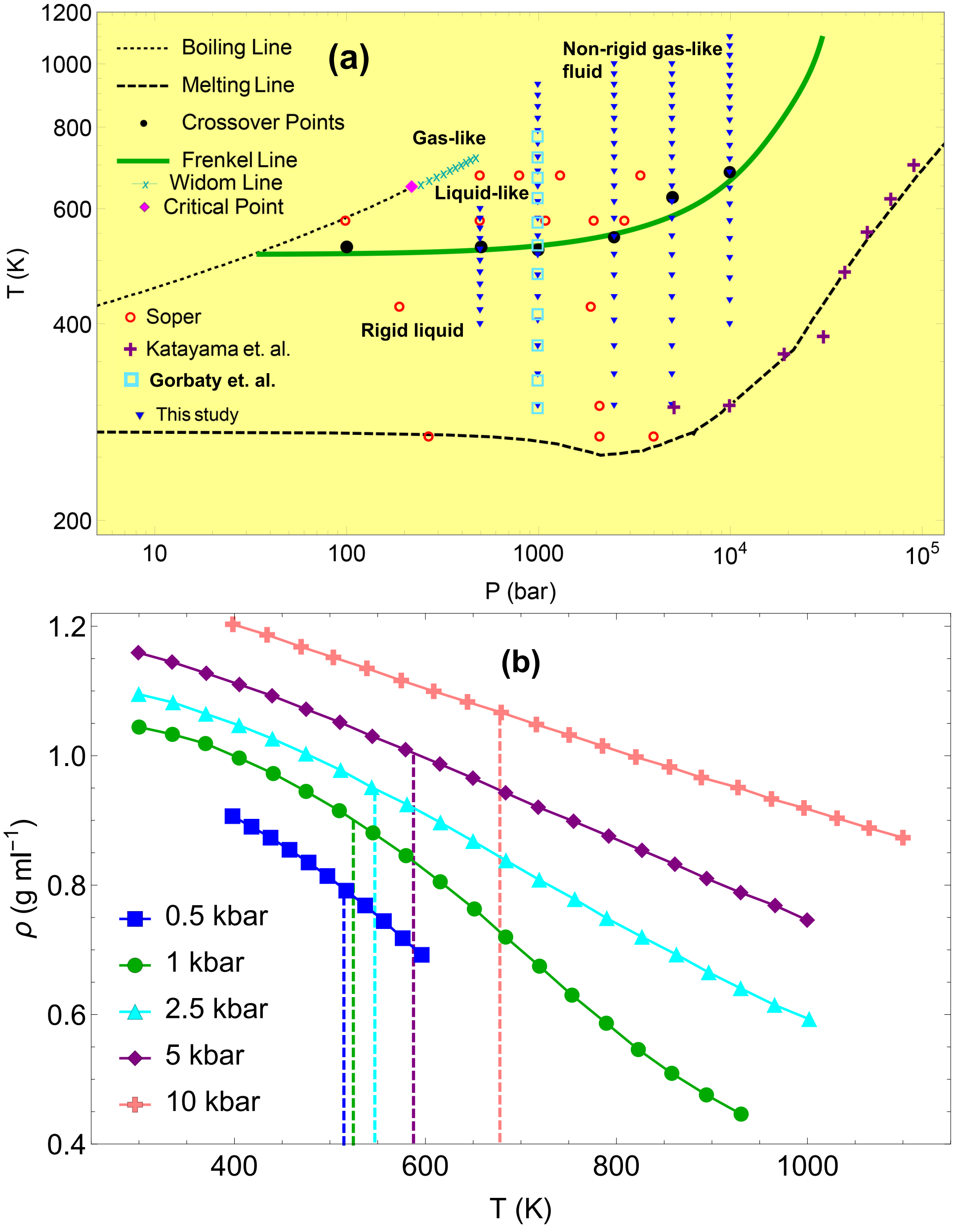

Figure 4.1: (a) Phase diagram of H_2O showing the Frenkel line (reproduced from [72]), together with experimental state points of Katayama [67], Soper [68], and Gorbaty [73] and state points used in molecular dynamics simulations in this work. The Widom line is reproduced from the data of Ref. [57]; (b) Density versus temperature plots for the simulated samples in this study. The Frenkel line (indicated by dotted lines) passes through regions of high density beneath the density fluctuations at the Widom line.

better at the expense of more contrived dynamics. This was done in order to compare the structural data which was to be collected, which, as one would hope, did not end up depending on the ensemble choice. In much the same vein, I also simulated systems of 32768 water molecules in order to make sure that data did not depend on system size, which they did not.

Production runs were used to calculate things like pressure and temperature, of course, but the structural data of interest were the radial distribution functions. Recalling our definition of $g(r)$ in Eq. 2.2.19, we can approximate it from a molecular dynamics trajectory by creating histograms over discrete bins, averaging over both atoms within a sample and timesteps over the trajectory. Conveniently, DL_POLY will perform this counting on the fly, eradicating the need for storing atomic trajectories over an entire run and then processing them. Water is polyatomic, meaning that it will have several different radial distribution functions for each possible pair of atoms. For TIP4P/2005, this results in 6 different radial distribution functions. The O-O function will serve our purposes - as there is only one oxygen atom per water molecule, it represents the translational intermolecular structure without containing information on orientation.

This procedure is not very complicated. Indeed, it's a very simple procedure, but it simply had not been done yet. However a few more calculations were done in order to gather more information on the structure, both of which are dependent on the radial distribution function. The first are distributions of the coordination number. The coordination number is cleanly defined only in perfect crystals, where nearest neighbours, next-nearest neighbours *etc.* are unambiguous. In amorphous materials, the statistical definition of coordination number, n_c, is:

$$n_\mathrm{c} = 4\pi n \int_0^{r_\mathrm{min}} \mathrm{d}r r^2 g(r), \tag{4.2.1}$$

where r_min is the position of the first minimum in $g(r)$. This measure therefore counts the mean number of molecular neighbours in the first peak of the radial distribution function. This allows us to calculate n_c using nothing more than the $g(r)$, r_in, and V which we have already calculated. The distribution of coordination numbers, however, is far more involved. To calculate this quantity, I took final configurations from the first round of production runs as initial configurations for a second round of production runs. During this second round, I recorded atomic positions every 1000 timesteps (1 ps) during the simulation, which lasted for 50 ps. Then, for each molecule in each of these 50 states, the number of neighbours within r_min at the corresponding temperature and pressure was recorded. These data were used to fill histograms, which I then trivially converted into discrete probability distributions.

The second auxiliary structural data I collect are the angular distribution functions. The angles in question are the angles between a given molecular and its neighbours. In a tetrahedral lattice, such as that which exists in water ice, this angle is 109.4°. The molecular configuration "snapshots" created in the second production runs just described were also used to calculate the angular distributions. The neighbour lists created in the coordination number calculations were passed to a separate algorithm which calculated the angle between each pair of neighbours for each molecule. These data were again used to fill histograms and converted into probability distributions.

4.3 Results

The O-O RDFs, showing intermolecular correlations, calculated from the production runs, are shown in Figs. 4.2a-c and 4.3a-b. In Fig. 4.2d I have plotted RDFs from two additional state points, simulated in order to compare to data from Alan Soper's work [68] at ambient conditions and at high temperature and pressure. The TIP4P/2005 model evidently acceptably reproduces the peaks of the RDF (the overestimation of the height of the first peak is a known artefact) at supercritical conditions. We will focus first on the lower pressure isobars, in Fig. 4.2a-c because the features are more interesting there. Upon temperature increase at 0.5 kbar and 1 kbar the second and third peaks diminish in height until they disappear. Simultaneously a new second peak, radially intermediate to the old second and third peaks, emerges as the new ones diminish. At 2.5 kbar, the second peak diminishes and disappears as it did at lower pressures, but the third peak diminishes somewhat before abruptly shifting leftwards (to a lower radial position) and becoming more prominent again. Not any of this pronounced behaviour is visible at 5 kbar and 10 kbar. The second peak is visible, though flat, at the lowest temperature at 5 kbar, and at 10 kbar all the RDFs resemble the high-temperature structure of the lower pressure isobars.

The behaviour of the RDFs is much more easily understood if we plot key features versus temperature. We start with the peak radial position versus temperature in Fig. 4.4. This shows the pronunciation of the crossover at low pressures: the old peaks become less prominent (represented by open symbols) than the new peak at a temperature very close to the FL on that isobar. The position of the RDFs at all pressures were calculated by inspection, since the transitions are rather dramatic. At higher pressures, the third peak instead reduces in radial position with increasing temperature down to a minimum near the FL before increasing again. At 2.5 kbar this minimum occurs not long after the disappearance of the second peak, but at higher temperatures the transition is completely smooth and the second peak disappears at a much lower temperature.

In Fig. 4.5 I show the mean molecular coordination number along four isobars, the distribution of coordination number at 1 kbar, and the angular distribution described above at 1 kbar, all as functions of temperature. The mean coordination shown in Fig. 4.5 is calculated using integration of $g(r)$, though the coordination data collected from the atomic positions produce the same mean. Inspection of the RDF at 300K and 5kbar (in Fig. 4.3a) reveals a problem with our definition of coordination number: the second peak shifts left and becomes a shoulder of the first peak, merging with it. This leaves us bereft of a well-defined first peak. This behaviour is not a problem with the definition, per se, because the behaviour of the RDF implies that there is no typical "first coordination shell" at all. For this reason, the lower temperature water simulations at 5 kbar do not support a meaningful coordination number, as can be seen in Fig. 4.5a. The coordination numbers at 1kbar and 2.5 kbar exhibit unusual behaviour: they increase with temperature, presenting maxima near the FL, before decreasing with temperature as they do at higher pressures. The decrease of coordination with temperature is a generic effect related to decrease of density and clustering as thermal energy increases. An increase of coordination with increasing temperature is indicative of a change in structure, therefore, and the maximum represents the termination of this change into a

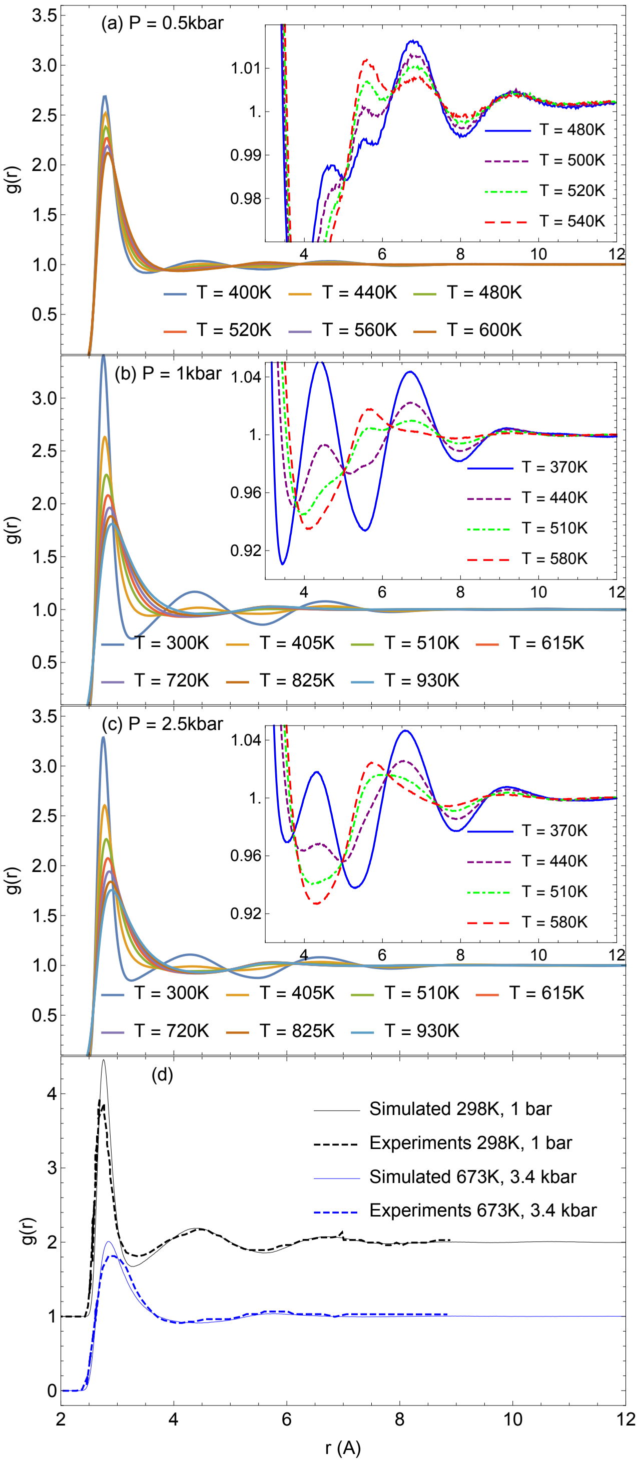

Figure 4.2: (a)-(c): O-O RDFs of simulated water at different pressures and temperatures. Insets are the same data but with reduced plotting range to highlight the secondary peaks. (d) Simulated and experimental [68] RDFs at ambient and supercritical conditions, offset by 1 for convenience.

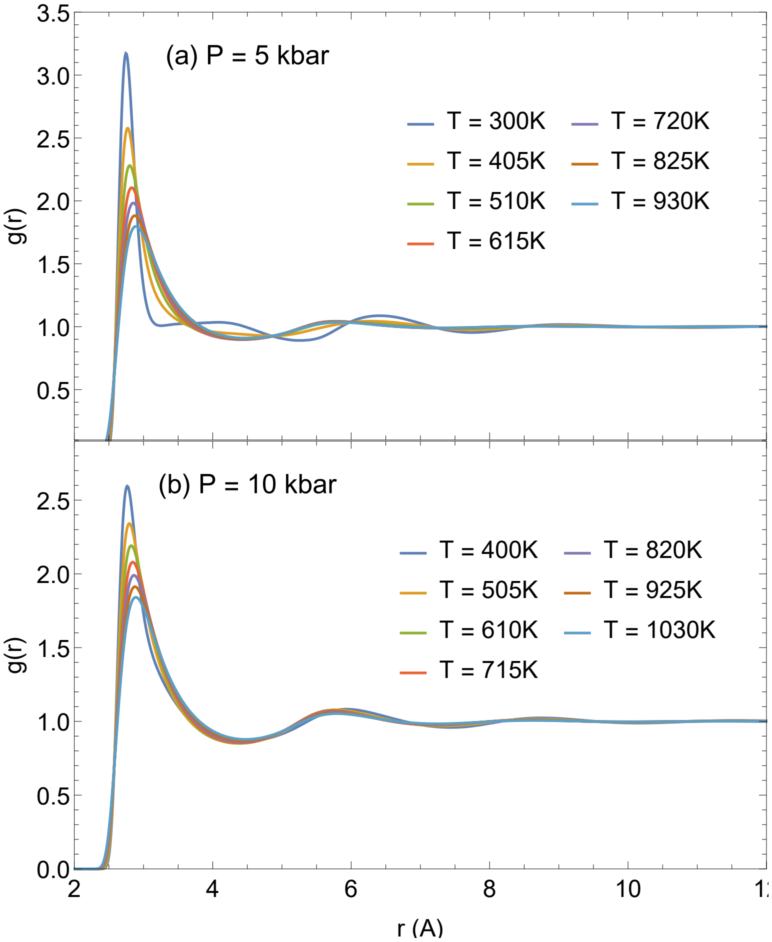

Figure 4.3: (a)-(b): O-O PDFs of simulated water at higher pressures.

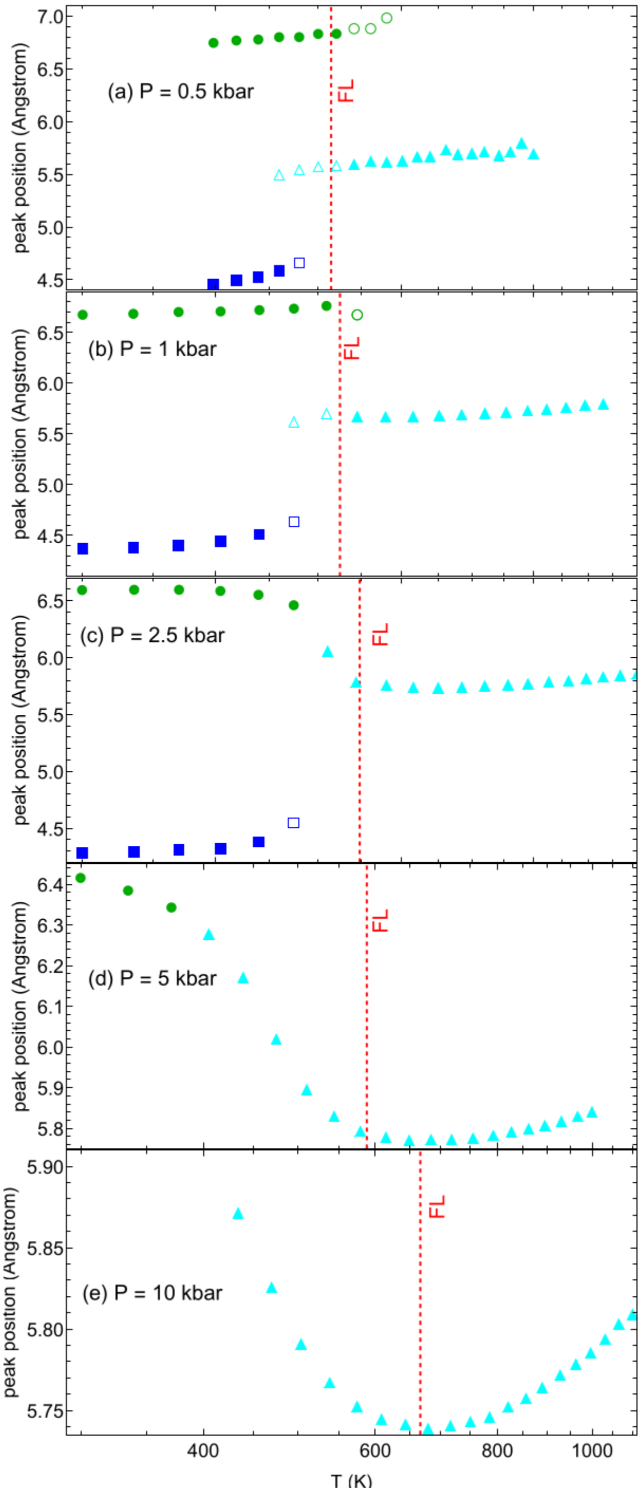

Figure 4.4: O-O RDF peak positions: Squares - second peaks; circles - third peak; triangles - new second peaks. Open triangles imply that the new peak is less prominent than the old peaks, and vice versa for open squares and circles. The dashed vertical lines correspond to temperatures at the Frenkel line.

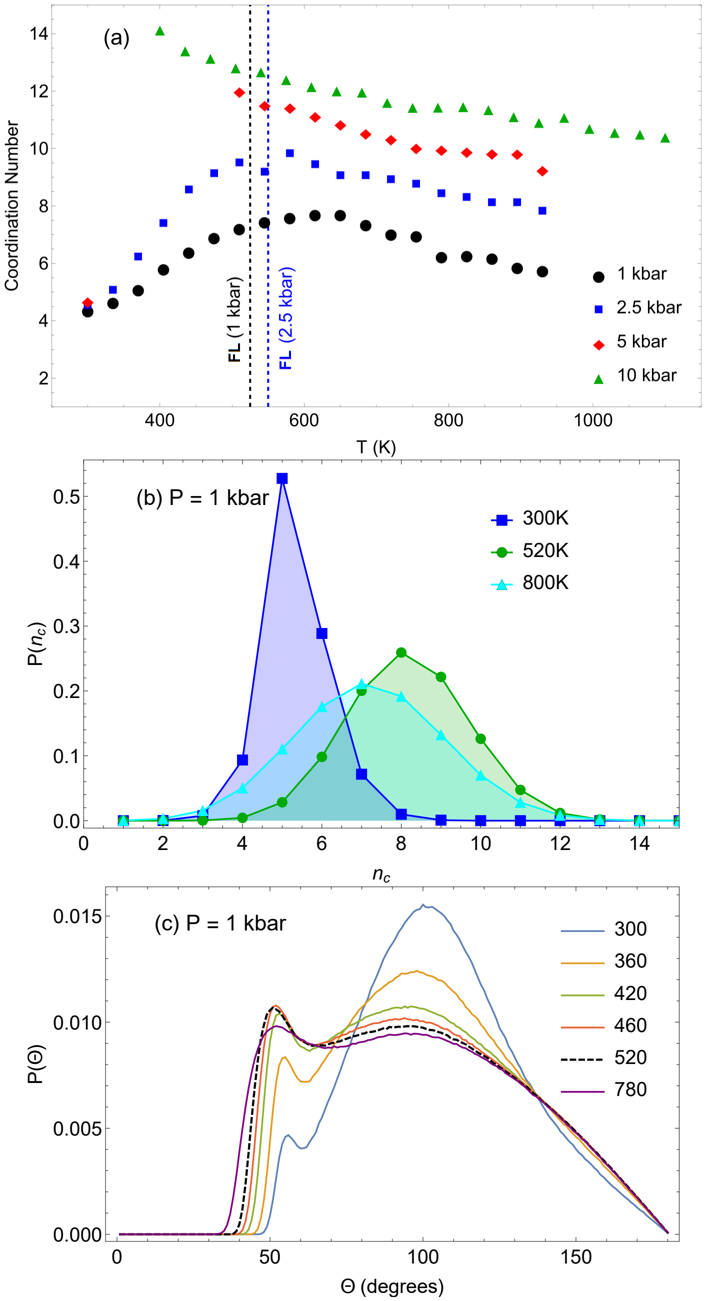

Figure 4.5: (a): Mean coordination number n_c of water molecules in the supercritical state across Frenkel line. The dashed verticle lines correspond to the temperature at the Frenkel line. n_c is not shown at low temperature at 5 kbar because the minimum between the first and second peaks in Fig. 4.2c disappears at those temperatures, causing an ill-defined cut-off. (b): Normalised histogram of molecular coordination calculated from structural snapshots at 1 kbar. (c): Intermolecular angular distribution functions at 1 kbar. The dashed curve shows the distribution at the temperature corresponding to the Frenkel line.

generic simple structure.

The discrete probability distributions in Fig. 4.5b give more details of this behaviour. The distribution at the lowest temperature, 300K, is sharp around 5-fold coordination, representing the prominent transient (nearly) tetrahedral structure in the liquid. As temperature increases the distribution broadens as its mean value increases and decreases, representing the weakening of structure as the tetrahedra are dispersed (as opposed to the adoption if a pronounced new structure).

We finally discuss the angular distribution in Fig. 4.5c, which shows a broad peak around 109.4° at the lowest temperatures, representing the tetrahedral structure. Notably there is a small but prominent peak at between 50 and 60°. 60° is the angle of close packing, so what this means is that there is a degree of close packing in the liquid. This is distinct from the amorphisation of tetrahedral structure, which causes the broadening of the 105° peak. As temperature increases, the degree of close packing increases, indicated by the increasing height of this 50-60° peak, and the tetrahedral structure becomes increasingly amorphous, indicated by the lowering height and broadening of the 105° peak. At the temperature at the FL, the close-packed peak becomes its most prominent along the isobar, and is more prominent than the diminishing tetrahedral peak. Above the temperature at the FL, both peaks further diminish. This behaviour is indicative of the same process as n_{c} - the tetrahedral structure below the FL gives way to a simple close packed structure, and this new structure dominates and evolves as expected above the FL.

The final data to discuss are the also derived directly from the RDFs: the height of the first peak. The overestimation of the first peak height must be noted in these analyses. The behaviour we see is real behaviour in the sense that this simulated system has a FL, and the structural changes we see are still valuable as guides to the behaviour of real water. The peak heights are not as intuitively evocative as peak positions, so here we are guided by theory. The height of a peak, $g(r_{\mathrm{max}}) - 1$, where r_{max} is the radial position of the peak, is predicted in solids to follow a power law with temperature [2, 75]: $g - 1 \propto T^n$. A perfect classical crystal at exactly zero temperature will possess a RDF consisting of delta functions. At a nonzero temperature, atoms can stray from their equilibria. If displacements are small, the potential energy curves they traverse will be approximately quadratic, which means that the spikes in the RDF will broaden into Gaussian peaks with variance proportional to the temperature. The height of a Gaussian peak is proportional to the reciprocal of its standard deviation, thence our power prediction for solid RDF peaks. Liquids possess a transitory solid structure, so we can argue that this relationship will hold for them too, at least below the FL where solidlike oscillation still exists in the dynamics. This prediction was tested and verified in molecular dynamics simulations of supercritical argon by my predecessor, Ling Wang [76]. The deviation from this power-law relationship coincided with the FL in these studies. I plot the peak height versus temperature in a log-log scale in Fig. 4.6, in order that a power law curve appear as a straight line. Here, at all pressures, the deviation from the low-temperature power law is clearly visible, and takes place within 5-15% of the FL predicted by the VAF criterion (shown as a dashed verticle line). This is the width of the crossover seen in structural and thermodynamic properties in experiments and modelling on other fluids [46, 50], including my later work on CO_2.

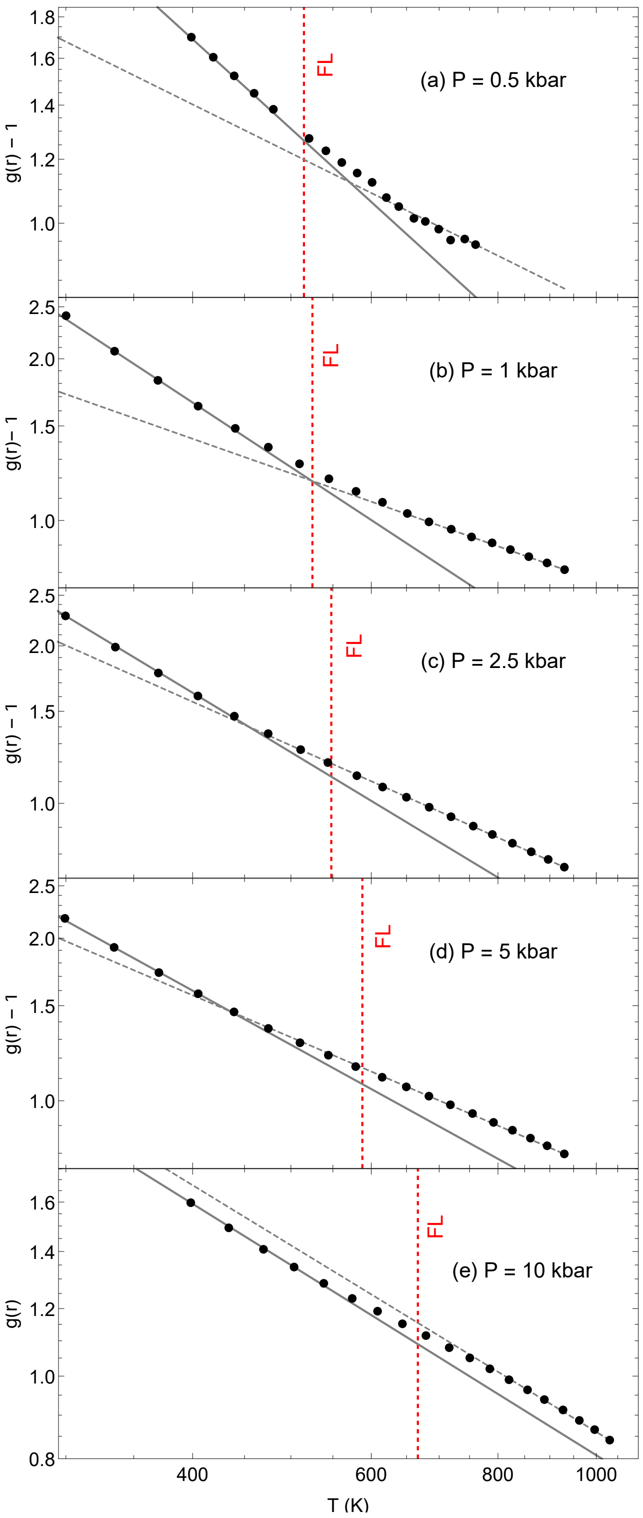

Figure 4.6: Log–log plot of the RDF first peak heights, showing the crossover of evolution as temperature approaches the FL. The dashed lines correspond to the temperatures at the FL

4.4 Discussion

The FL therefore, with a multitude of evidence, stands at the climax of a structural transformation in water. We attribute this transformation in the features of the RDFs to the dynamical crossover at the FL *and* a water-specific structural crossover. The transformation of water from a tetrahedral structure at low pressures and temperatures to a closely packed structure at high pressures and temperatures is well-known. Water's tetrahedral structure is dominated by the electrostatic energetics of hydrogen bonds and is open (in the sense of low coordination), meaning that increasing the kinetic energy of a system or compressing it can can destroy this structure. A structural crossover is therefore an inevitability in water, but there was no guarantee that it would be related to the FL. The data have made this association. The black disks in Fig. 4.1a are what we label the "crossover points". At low pressures, where the crossover is pronounced, the "crossover point" is defined as the temperature at which the new peak becomes more prominent than the old diminishing ones. The appearance of a secondary peak at positions intermediate to the old peaks is indicative of a complete change of structure. We call this change pronounced because the new peak emerges from nothing (and the old peaks diminish into nothing) rather than a continuous transition from one structure to another. At higher pressures (where the old second peak corresponding to tetrahedral coordination has disappeared at temperatures far below the FL), the "crossover point" is defined as the temperature at which the new second peak reaches its radial minimum, above which it moves outwards with temperature again. Along isobars where density can decrease with temperature increase, it is natural for peaks to move outwards as the mean distance between molecules increases. A peak moving inwards is suggestive of a change in structure, therefore, and the radial minimum is a good measure of the apex or completion of a structural crossover. The crossover's apex, by these definitions, as can be seen in Fig. 4.1a, very closely follows the locus of points which defines the FL.

Based on these observations, we propose that the FL is a *facilitator* of the known structural crossover in water from tetrahedral to closely packed, extending from near the critical point (at 500 bar) to the deep supercritical state (up to 2.5 kbar). The method of the facilitation is as follows: as the oscillatory component of molecular motion is lost in the tetrahedral structure, water molecules acquire purely diffusive motion and thence the flexibility to arrange themselves into a denser structure in response to the hydrostatic pressure. It's worth being clear here about what I mean by "close packing". In solids, close packing is one of two structures, hexagonal or face-centered cubic crystals. Each atom has 12 nearest neighbours and the packing fraction is the maximum possible in three dimensions, at about 0.74. In liquids, when I say close packing, I simply mean a simple structure where atoms and molecules are jammed together as close as the external pressure can manage with no short or medium range order to counteract it. A "closely packed" fluid can therefore have a relatively low coordination number which simply represents a low density while the atoms or molecules still lack any short or medium range order. The solid-like oscillatory motion maintains the tetrahedral structure, and its termination at the FL allows the structure to rearrange itself into the simpler "closely-packed" configuration at higher temperature and pressure. The loss of the tetrahedral structure at low temperatures, say 300K, by increasing pressure is achieved by overcoming the hydrogen-bonded energetics by force. Increasing temperature along an isobar, however, does not disperse the structure by giving the molecules enough kinetic energy to overcome the hydrogen bonds. Instead the increase in kinetic energy creates more frequent "escape routes" from the tetrahedral cages, to the point that molecules are diffusive so often that no tetrahedral structure can be sustained at all. At these low pressures, therefore, water transitions from a tetrahedral rigid liquid into a closely packed rigid liquid on approach to the FL, and from a closely packed rigid liquid into a gaslike non-rigid fluid above the FL.

Let me emphasise that the novelty here is not the transformation itself, for that inevitably must occur *somewhere* in the supercritical state. Rather the unexpected discovery is that this pronounced structural crossover, the loss of water's tetrahedral structure which gives it many of its intriguing anomalies, is *coupled* to the FL and operates in the deep supercritical state, far from the melting line and critical point, where such transitions were traditionally thought to be absent. One could have predicted that the FL, with it in mind, would have been the upper limit (in temperature) for this transition, but there was no guarantee that it did not happen below the FL, or indeed in a curve through state space that didn't resemble the FL's shape at all. Thinking about the liquid and supercritical state in terms of dynamics is clearly a powerful tool, as it has elucidated the transition of water from its unique structure to that of a simpler liquid.

There is a single experimental structural study (at least of which I am aware) which crosses the FL in deeply supercritical water in a neat and analysable manner, that of Gorbaty *et. al.* [73], which uses x-ray scattering to extract the O-O RDFs at 1 kbar. A comparison of the peak positions between my simulations and the experimental data is given in Fig. 4.7. The peak positions at low temperature from the X-ray data are very close to those from my simulations, and the second peak disappears at almost the same temperature from both sets of data. The behaviour of the third peak at 1kbar in the X-ray data is more similar to the simulated data at 2.5 kbar: it transition into the new peak continuously rather than giving way to a newly emerged intermediate peak. After it drops down to this minimum at the FL, it moves radially outwards as temperature increases. The structural crossover's proximity to the predicted FL is therefore present in these experimental data, though the crossover itself is somewhat less abrupt.

We now turn to the RDF features at higher pressures. As mentioned, the FL extends to arbitrarily high temperatures and pressures, provided the system remains chemically unaltered. In Fig. 4.4, we see that the second peak disappears far below the FL at these pressures, implying that the transformation from tetrahedral to close packing is nearly complete. The transformation we see is more subtle, but new second peak increasing from a minimum is still seen, suggesting that the FL is still the conclusion of a transformation beyond which the peak shifts outwards as it does at all other pressures. Likewise, the deviation from the solidlike law in the height of the first peak seen in Fig. 4.6 remains unchanged at high pressures. The FL therefore facilitates water's dramatic structural crossover in its tetrahedral state, and creates a more subtle crossover in its simpler high-pressure state.

These observations demonstrate the potential breadth of the implications of the FL. Water is an interesting, complicated, and anomalous system with very many applications in industry. These findings imply that the FL and its theoretical backdrop describe

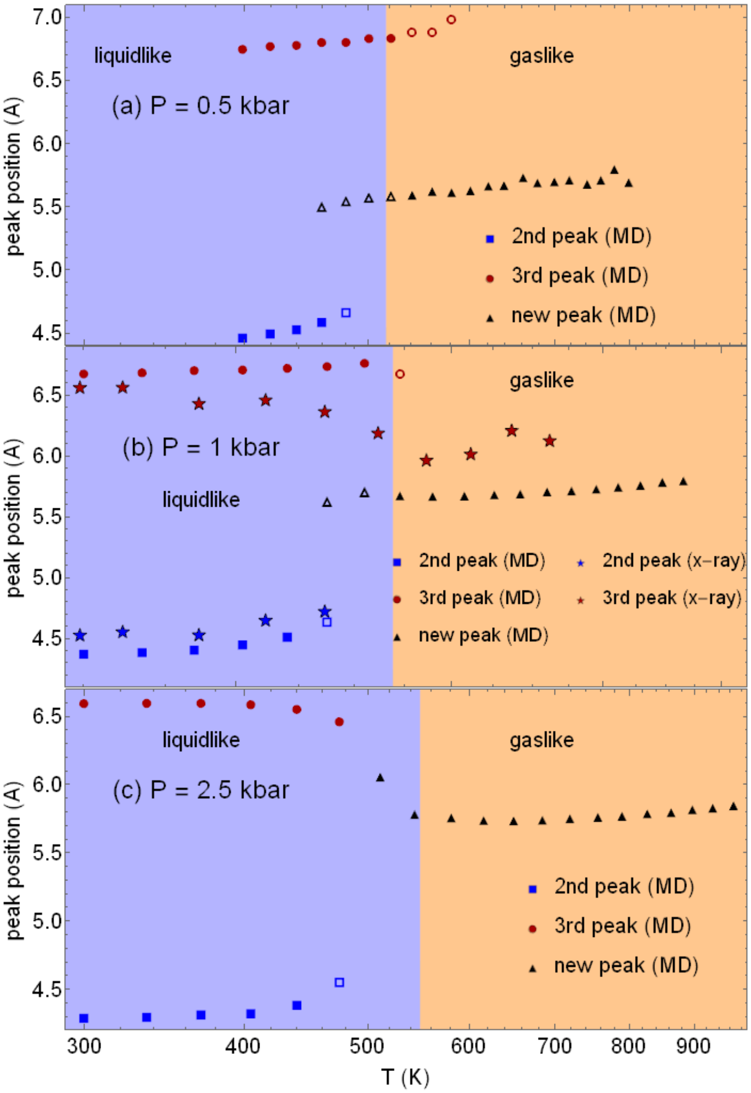

Figure 4.7: O-O PDF peak positions from molecular dynamics (MD) data and X-ray scattering data [73]. As before, open triangles imply that the new peak in the MD data is less prominent than its neighbours and vice versa for open squares and circles.

fundamental mechanisms in fluids, because the effects of the FL are amplified in the anomalous substance of water, rather than diminished. Furthermore, supercritical water is industrially relevant and these results will serve as a stimulus and guide for future experimental and theoretical work into supercritical water.

Chapter 5

Carbon Dioxide

5.1 A Very Versatile Fluid

Carbon dioxide is a rather notorious compound for its role as a greenhouse gas, not only in the terrestrial atmosphere but also the Venerian atmosphere. It's also an interesting compound for its physical properties, as the triple point lies at a pressure exceeding atmospheric pressure, giving us a convenient example of sublimation. Though we may wish to use the FL to redefine what is meant by a liquid and discuss whether such a state exists beyond the critical point, it does us well to remember that it is still terminated before before the zero of temperature or pressure. The mixed dynamical state is not a guaranteed privilege.

Returning to earth, supercritical carbon dioxide is used in a wide variety of applications, more even than water, such as polymer synthesis and processing [77, 78, 79], dissolving and deposition in microdevices [80], solvation, green chemistry, green nanosynthesis and green catalysis [30, 31, 33, 34, 81, 82, 83, 84, 85, 86, 87], extraction [88], chemical reactions [32], and sustainable development including carbon capture and storage [89]. Carbon dioxide's prevalence means there is a lot to be gained from a deeper understand of its supercritical state.

Much like with water, the FL was determined in supercritical carbon dioxide using the VAF criterion by one of my predecessors [72]. The simulations I describe here were performed in collaboration with neutron scattering experiments performed by Sarantos Marinakis and Alan Soper [90]. Carbon dioxide's phase diagram is shown in Fig. 5.1. The critical point of carbon dioxide is 73.8 bar and 304 K, which is exceeded substantially in temperature and pressure by water due to water's stronger configurational energetics. The FL crosses the isobars of 500 and 590 bar along which this study is performed at 297 K and 302 K respectively, such that, though the temperature is not deeply supercritical, the states we probe are still far from the critical point and fairly far above the melting line (around 200 K at these pressures).

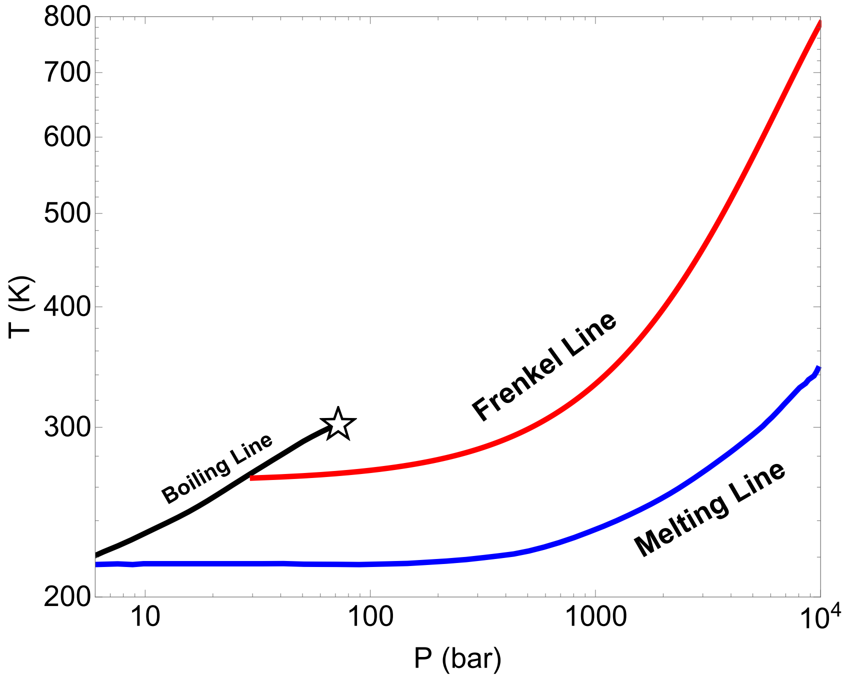

Figure 5.1: The phase diagram carbon dioxide, showing the Frenkel line with reference to the boiling line and melting line. The star represents the critical point.

5.2 Molecular Dynamics Simulations

The potential used here, described in Section 3, was used to locate the FL in carbon dioxide by a predecessor [72], which guided the work here. The potential parameters are listed in Tab. 3.2. Much like with water, permitted by our lack of interest in the crystalline state, an initial configuration of 30752 carbon dioxide molecules was prepared in a square lattice to be melted and pressurised in equilibration runs. With my experience from water and anticipating a less pronounced transition in carbon dioxide, I started with this large number of molecules in order to generate RDFs as sharply as possible. As it happens, it would take more effort than this to gather the required statistics. Equilibration was performed in the NPT ensemble with the Langevin thermostat and barostat for 30 ps (30,000 timesteps) to calculate the required density at each state point. Initial configurations were then remade at the target density and melted and equilibrated with velocity rescaling followed by 100 ps of production runs in the NVE ensemble during which RDFs were collected. Each isobar was traversed from 220 K to 500 K in increments of 10 K.

5.3 Results

The RDFs calculated from MD trajectories are shown in Fig. 5.2. Unlike in water, there are no sharp or dramatic transitions. The first, second, and third peaks all reduce in height and shift radially outwards, as expected as temperature increases on an isobar.

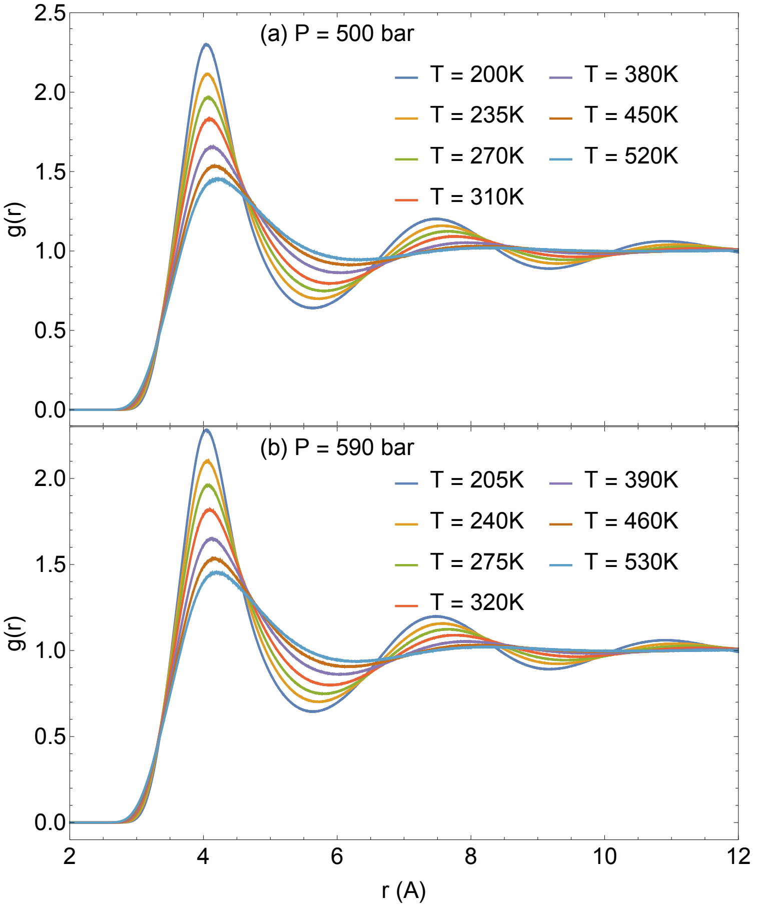

Figure 5.2: Evolution of C-C RDFs of simulated carbon dioxide at different pressures and temperatures.

These RDFs resemble those of water at higher pressure, indicating a lack of pronounced medium-range structure. This is not unexpected, as carbon dioxide lacks the necessary geometry to be polar (the oxygen-carbon-oxygen angle is π), and doesn't contain bonds with high electronegativity differences like the hydrogen-oxygen bond in water.

Since the RDFs do not exhibit any pronounced changes like those of water, I deemed it important to create a more systematic procedure for determining the position of a peak. This procedure was to fit a parabola to the crest of the peak. To reduce ambiguity, this fit would have be reasonably insensitive to the range (in r) of data used to create the fit. Specifically, data from up to 1 Angstrom on either side of the peak were used to fit a parabola, and the uncertainy on the centre and heights of these parabolae were less than 5% of the absolute values at all temperatures and pressures. The mean peaks positions and heights of these parabolae are used in the discussion that follows. The positions of the first peak are plotted in Fig. 5.3, together with fits made from data below and above the FL. These fits are reasonably convincing, as the peak positions appear to remain linear at temperatures far above the FL. The transition, however, is not sharp, and one can doubt whether there is truly much to see here - the RDF peak expands more readily with temperature in the gaslike state above the FL, which is an easy thing to predict, but is rather more weak than I would have hoped. Furthermore, there is enough noise, particularly at low temperatures, to call into question conclusions about a transition so weak to begin with.

I therefore began a new suite of simulations, intending to much improve the quality of the statistics and to decisively arrive at a conclusion. New initial conditions underwent a full 500 ps of equilibration time in order to as accurately as possible generate production initial conditions at the necessary density. The production runs too were extended to 500 ps to remove as much spurious noise from the RDFs as possible thereby reducing ambiguity in peak position determination. Furthermore, I doubled the density of state points in the low temperature region, such that below 300 K I had simulations every 5 K, and increased the maximum temperature of the range to 600 K. The first peak positions extracted from these trajectories are plotted in Fig. 5.4. With reduced noise and an increased temperature range, what formerly appeared to be a bilinear transition now appears to be a continuous curve. My skepticism paid off, it seems.

The transition in the peak heights seen in water in the previous chapter and previously in argon [76] are fully evident here, as seen in Fig. 5.5. This transition seems to be universal across the FL. This makes sense, at it's predicated solely on the small displacements of solid-like oscillations, which are present by definition in any fluid below the FL. However this leaves the peak positions in Limbo. Heights are all well and good, but they don't exactly overflow with intuition. They measure the pronunciation or permanence of coordination shells, which is hard to sink one's teeth into. If a appreciable crossover exists in the intermolecular geometry itself (rather than its statistical prevalence), we must look more closely and think more carefully.

Let us question what the first peak position signifies and why we ought to care. The simplest measure of distance between particles is simply the cube root of volume divided by particle number. Volume divided by particle number is the mean volume occupied by a particle, so its cube root defines a characteristic length, l_V related to this volume. This provides no information about the structure itself, however, as the only structural

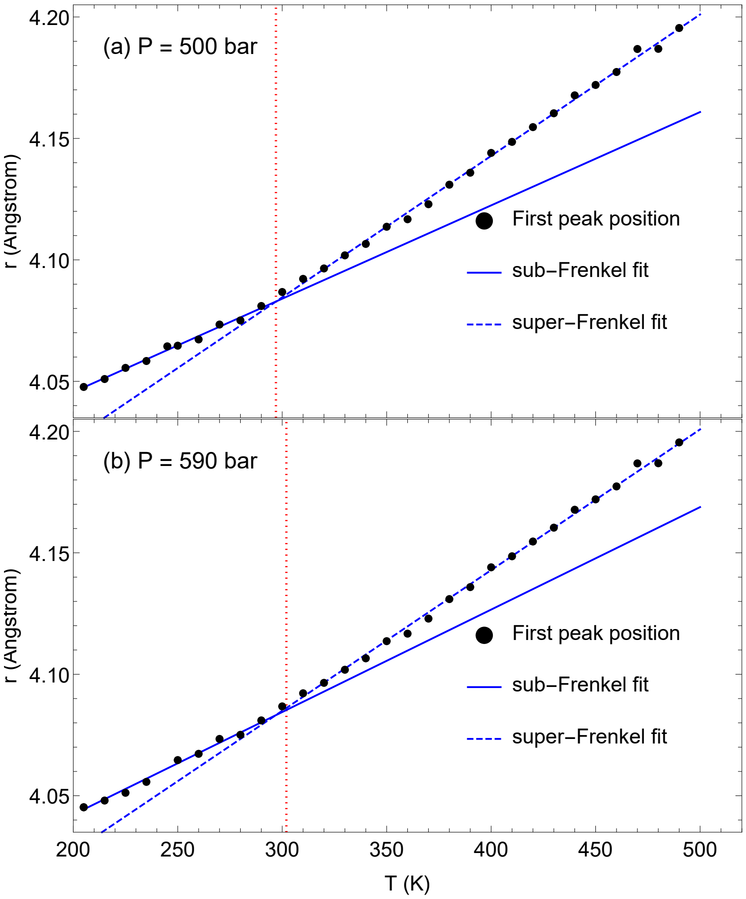

Figure 5.3: Evolution of the first peak position of the C-C RDFs with temperature. The dotted lines correspond to the temperatures at the FL.

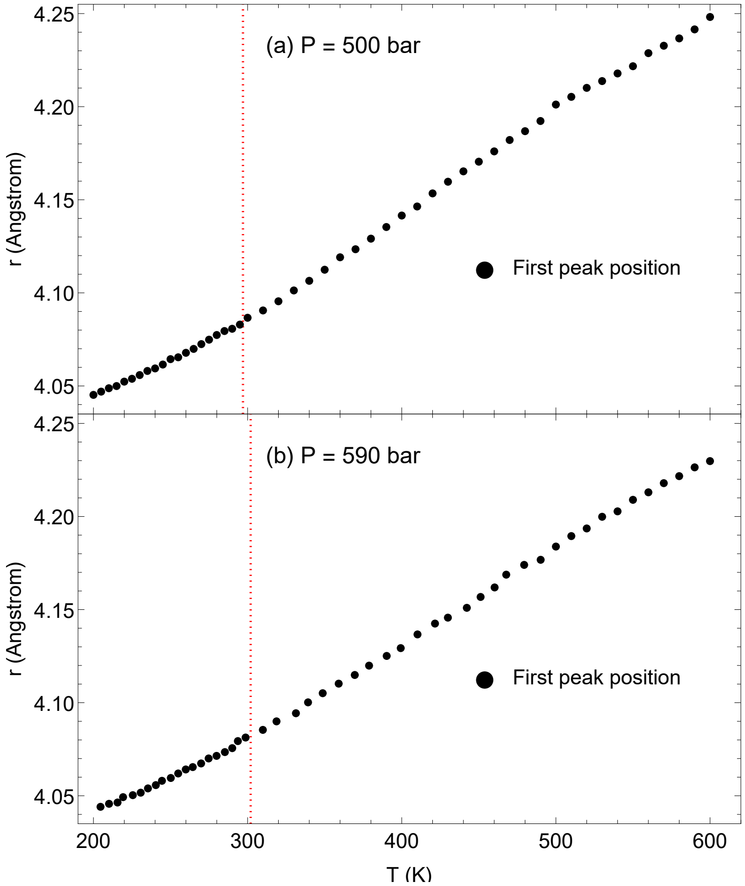

Figure 5.4: Evolution of the first peak position of the C-C RDFs with temperature from the second batch of simulations with greater precision. The dotted lines correspond to the temperatures at the FL.

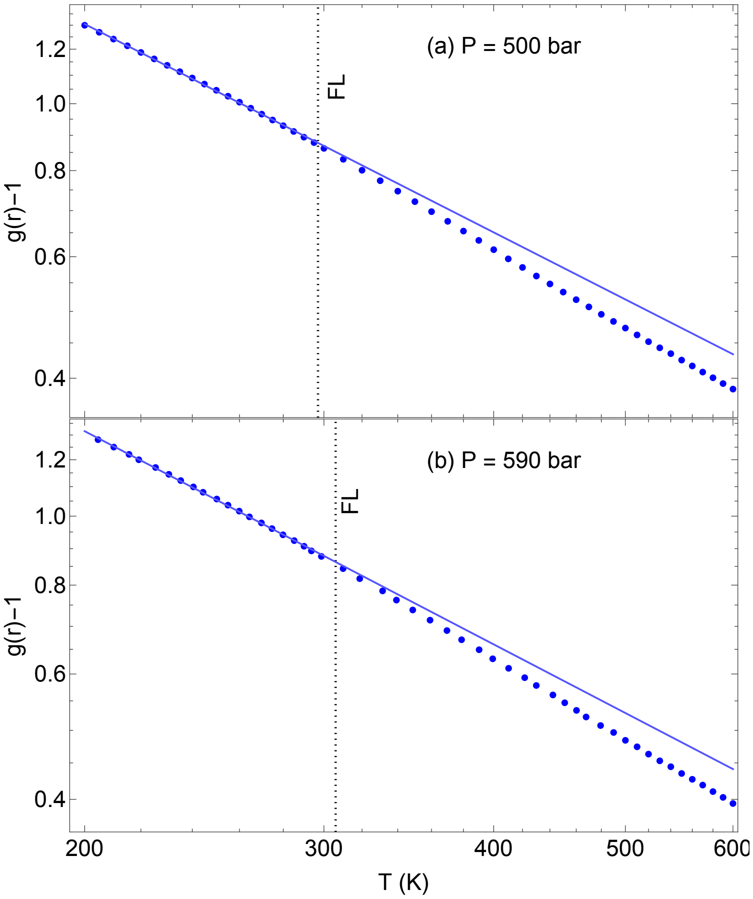

Figure 5.5: Evolution of the first peak height of the C-C RDFs with temperature. The dotted lines correspond to the temperatures at the FL.

information it contains is from the density. The peaks of the RDFs describe patterns of low and high local density surrounding the typical particle. The first peak position, r_{fpp} is the the distance between first nearest neighbours, and its deviation from l_V signifies a degree of clustering and local fluctuations in density from the mean. The density itself undergoes no crossovers in this deep supercritical state (rather famously!) and this distance r_{fpp} itself is the subject of no helpful theoretical predictions in fluids (though the oft-forgotten work by Green in Ref. [91] is worth reading), but the combination of the two parameters is insightful. Simply examining r_{fpp} alone is tricky, in absence of dramatic changes, because the density changes along our isobars which surely affects the peaks. A stronger measure of intrinsic short and medium range structure is performed by accounting for density.

Let me explain what I mean. In a simple cubic lattice, $l_V = r_{\text{fpp}}$. Therefore as you compress and expand the crystal, $l_V = r_{\text{fpp}}$ will always hold. In a body centered cubic lattice, the first nearest neighbour distance is $\frac{\sqrt{3}}{2}a$, where a, the lattice constant, is equal to $\left(\frac{2V}{N}\right)^{\frac{1}{3}}$ as the lattice has two atoms per unit cell. Therefore the body-centred cubic lattice has a different constant of proportionality between l_V and r_{fpp}, about 1.09, but it is still a constant, so long as the structure doesn't change. Using similar considerations, the constant is 1.12 in the face-centred cubic lattice, and 0.833 in a diamond cubic lattice. The physical meaning of this proportionality is *uniform compression.* If the crystal is subject to bulk strain, the structure at all levels is scaled in the same proportion to this strain. Such behaviour is obviously not sustainable as extreme compressions or expansions, and eventually the old structure must give way to a new one, disrupting the original proportionality between l_V and r_{fpp}. In solids, this would usually involve an abrupt phase transition from one crystal structure to another. However we are dealing with fluids, and therefore do not expect a sharp structural change.

In Fig. 5.6, I show the relationship between l_V and r_{fpp}, except I scale each by its value at a reference temperature, the predicted temperature of the FL. These plots contain the same information as l_V *vs.* r_{fpp}, but in a more easily understood manner. At the lower temperatures, the first peak position clearly shares a linear relationship with $V^{\frac{1}{3}}$ at both pressures. This indicates that in this liquidlike state the local structure is not significantly disrupted by the thermal expansion of the fluid. Above the FL, the deviation is stark and consistent. Furthermore, the linear relationship is destroyed completely, rather than the old relationship giving way to a new one. This is expected behaviour, as gases are not condensed systems and the first peak position in a gas is more dependent on the size, geometry, and interaction of the constituent molecules [91] rather than the density. This linearity and deviation from it at higher temperatures has been observed in molten group 1 elements and liquid CS_2 [92, 93, 94]. The low level of noise and close temperature spacing at low pressure make this conclusion already quite strong, however I decided to back it up further with statistical analysis.

To determine whether a crossover is taking place here, I fitted the data to two different sorts of functions. The first was either quadratic, or log plus linear:

$$f_1(V) = \begin{cases} a + bV + c\log(V) \\ a + bV + cV^2 \end{cases} \tag{5.3.1}$$

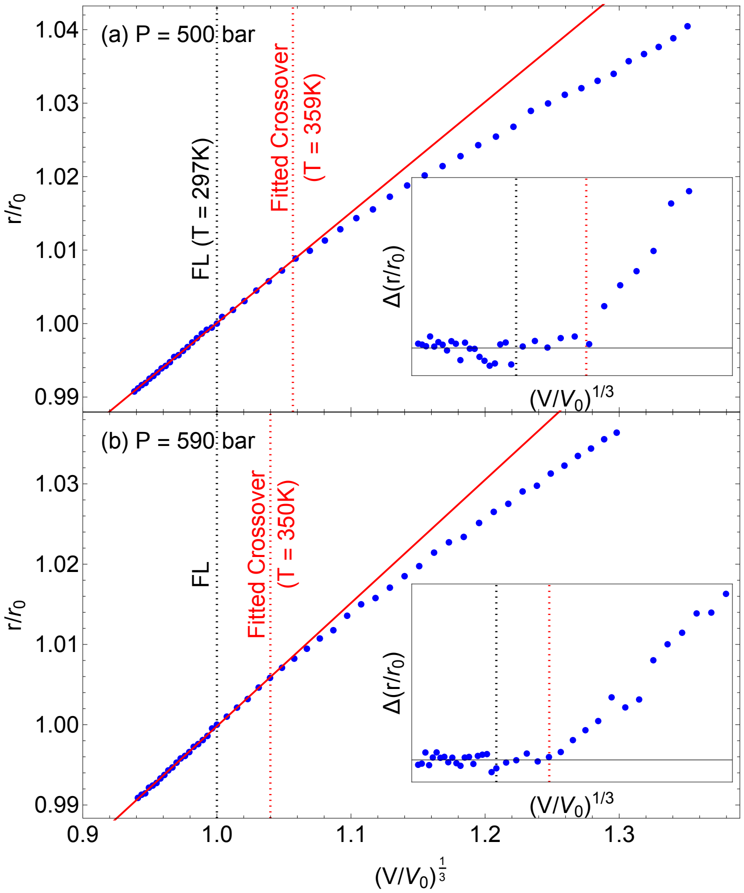

Figure 5.6: Relationship between the first peak position r and the system's characteristic length $V^{\frac{1}{3}}$. Dashed vertical lines show the fitted crossover volume and the volume at the FL. Insets: Relative trend of the residuals of the linear fit

The curves are obviously not cubic, or above, as extrapolating such curves would lead to sharp drops up or down. The quadratic or log plus linear functions fit the shape of the data well and will serve duly for our purposes. The second sort of functions we consider are linear below a certain transition volume, V_c, and either quadratic or log plus linear above this volume:

$$f_2(V) = \begin{cases} (\alpha + \beta V)\,\Theta(V_\mathrm{c} - V) + (a + bV + c\log(V))\,\Theta(V - V_\mathrm{c}) \\ (\alpha + \beta V)\,\Theta(V_\mathrm{c} - V) + (a + bV + cV^2)\,\Theta(V - V_\mathrm{c}) \end{cases} , \tag{5.3.2}$$

where Θ is the Heaviside step function, and $a, b, c, \beta, V_\mathrm{c}$ the fitting parameters (α depends on the other parameters in order to ensure continutity at V_c. The linear fits at low volume in the log plus linear case are also shown in Fig. 5.6. The insets here show the "residuals", the difference between the data and these linear fits. These residuals increase from zero sharply above the transition temperature, suggesting a real change in functional dependence across the transition volumes, corresponding to about 350K and 359K at 500 bar and 590 bar respectively. This is in line with previous observations of the width of the crossover at the FL.

There is one final analysis I performed to justify claims of a crossover. Generally speaking, one improves the numerical quality of a fit by adding more parameters to it. One can, *a priori*, justify a penalty for the number of fitting parameters a fit uses; otherwise one ends up with as many parameters as data and a polynomial of such a degree will pass through them all. There are two closely related quantitative measures of goodness of fit which penalise the number of parameters: the Akaike Information Criterion (AIC) [95] and the Bayesian Information Criterion (BIC) [96]. Such measures are quantitative, but, of course, somewhat arbitrary, but they are also widely used and accepted. Applied to our data, the AIC and BIC, applied to the composite functions in Eq. 5.3.2, were substantially lower than -10 below those for the single functions, which is a decisive preference for two different functional dependencies in the data above and below a certain volume, V_c.

5.4 Discussion

The structural crossover in carbon dioxide was shyer than that in water, and her true colours were not shown without due dedication on my part. The crossover in the peak heights appears to be a universal and reliable effect of the FL. Other effects are system dependent and more interesting. Water, for example, does not show the deviation from uniform compression above the FL, because it doesn't uniformly compress below the FL. This is hardly surprising, as we have seen much evidence that this region below the FL is host to a continuous structural transformation. Carbon dioxide has no such transitions in its liquidlike state, as we have demonstrated, but still loses its short and medium range structure, like water does, due to the decoupling of density with the first nearest-neighbour distance. This is an important finding because the FL is a fundamental and universal phenomenon, and its effects should not be confined to anomalous compounds.

As mentioned, this work was published in collaboration with experimental studies on supercritical carbon dioxide. The result of these neutron scattering experiments was the

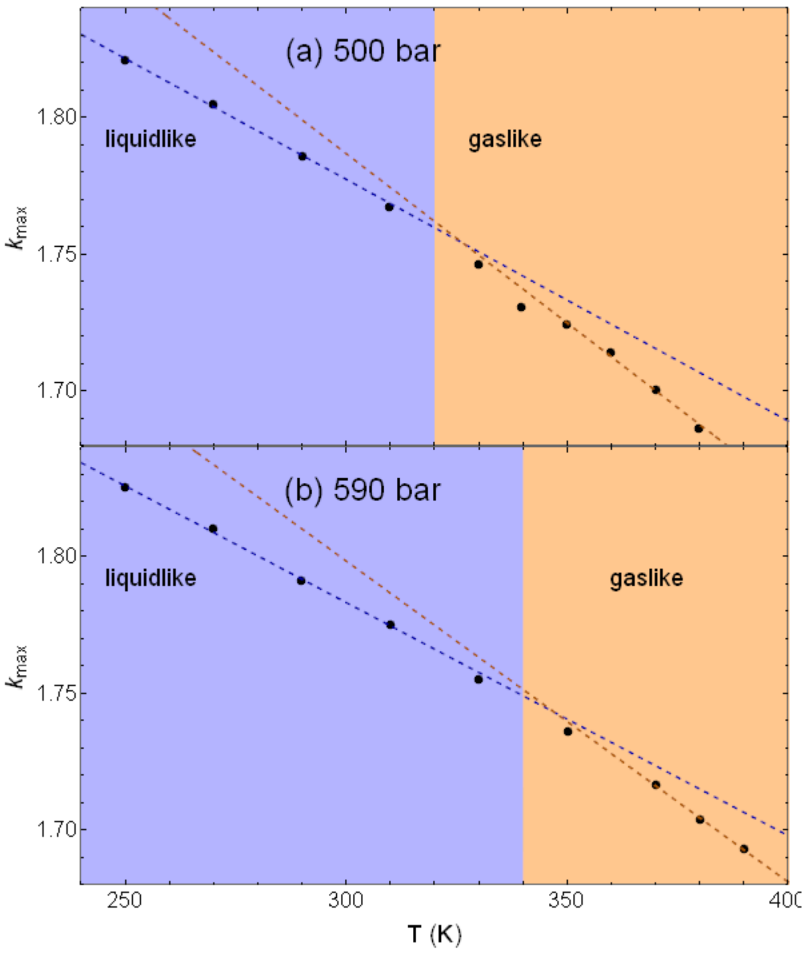

Figure 5.7: First peak position k_{max} of the structure factor $S(k)$ of supercritical CO_2, extracted from neutron scattering experiments [74], as a function of temperature T at (a) 500 bar; (b) 590 bar.

extraction of the total structure factor (which includes contributions from C-C, O-O, and C-O correlations). A subtle crossover in the peak positions of the structure factor is seen here [90], similar to those seen neon [46] and nitrogen [47]. The first peak position of the structure factor is plotted as a function of temperature in Fig. 5.7, where we see the behaviour those who have studied the FL have come to expect: the first peak position changes more readily with temperature above the FL than below. Considering subcritical liquids to subcritical gases, the liquids are more compressed and resistant to changes in structure, whereas gases are easily expanded. The first peak of the structure factor represents the dominant periodicity in the system, so the crossover we see represents the "coordination shells" (which won't be very sharp above the FL) spreading into a larger wavelength more readily at high temperatures. This crossover again happens within 10% of the crossover predicted by the VAF criterion.

Performing a Fourier transformation of the structure factor gives the total RDF, not quite the same as the partial C-C RDF we extracted directly using MD simulations. The first peak of the total RDF is, however, scarcely affected by other contributions, and serves as a respectable comparison. The same analysis was performed on these experimental RDFs as I did on the MD RDFs, using data from NIST [97], the results of which are plotted in Fig. 5.8. The crossover here is harder to discern from inspection, but, noting the worse quality of the experimental data, we can compare to the modelling data and say that the behaviours are in agreement including the temperature of the crossover to within 10% of the predicted crossover from the VAF criterion.

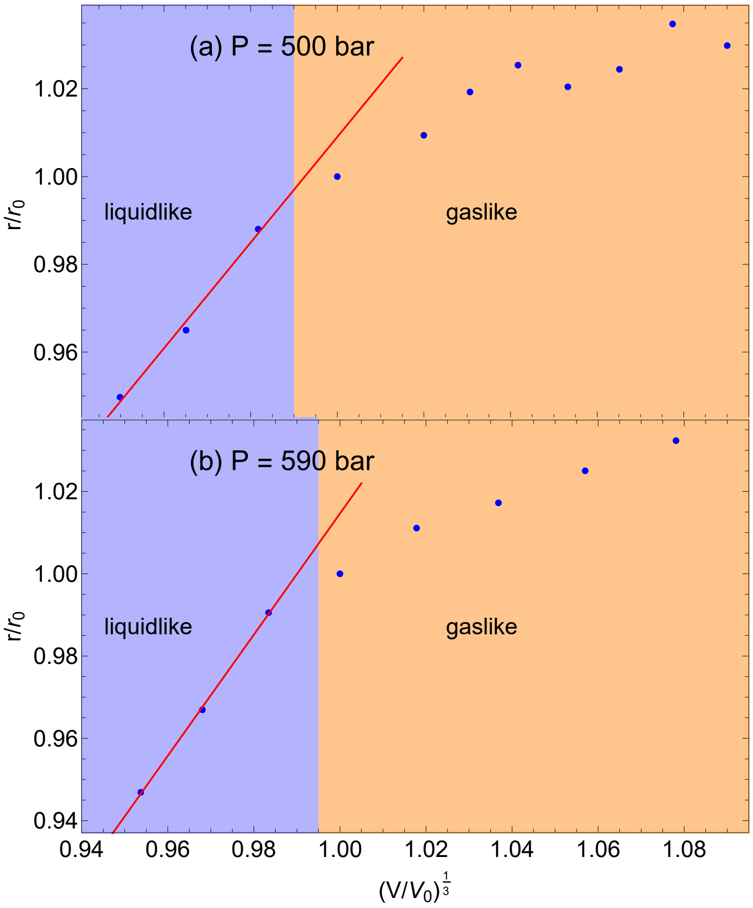

Figure 5.8: First peak positions of the experimental weighted sum PDF for CO2 at (a) 500 bar and (b) 590 bar as a function of the volume. The liquidlike and gaslike regions meet at the modelling prediction of the FL at (a) 297 K; (b) 303 K.

Chapter 6

Chaos

6.1 Dynamical Instability

For this next project we investigate a particular dynamical quality of a system, borrowed from chaos theory - *dynamical instability.* Dynamical instability is the phenomenon in which neighbouring trajectories in phase space diverge from each other under their dynamical evolution. In such systems a small perturbation to a trajectory will cause significantly different evolution, and trajectories have a tendency to spread out all across phase space. Dynamical instability and chaos theory are of interest to the foundations of classical statistical mechanics [98] and have important implications in the ability of digital computers to faithfully recreate Hamiltonian trajectories [99].

The mathematical work which addresses dynamical systems with this property is called Ergodic Theory. Ergodic systems, mathematically, are the lowest rung on the so-called *ergodic hierarchy* which describes dynamical instability [98]. To speak technically, dynamical instability is the phenomenon in which neighbouring points in the phase space of a deterministic dynamical system diverge exponentially under the system's evolution. Verbally: the present determines the future, but the approximate present does not approximately determine the future. Small uncertainties in the state of a system will lead to increasingly poor predictions as the system evolves. Dynamical instability is a necessary but insufficient condition for all categories on the ergodic hierarchy. There are no known general conditions for these categories, but ergodic systems are in some sense the "weakest", the least dynamically unstable. Each rung on the ergodic hierarchy implies the ones below it. The next step up is *mixing systems.*

We define a dynamical system $\mathscr{D} = (\Gamma, \mathscr{O}, \mu, \mathscr{M})$, with phase coordinates Γ over phase space $\mathscr{M}$, time evolution operator T, and measure μ (so far we have used a probability density as a measure and called it ρ). This dynamical system $\mathscr{D}$ has the *mixing* property if, for any $A, B \in \mathscr{M}$ [100]:

$$\lim_{t\to\infty} \frac{\mu(A_t \cup B)}{\mu(A)} = \frac{\mu(B)}{\mu(\mathscr{M})}, \tag{6.1.1}$$

with $A_t = T(t)A$, the time evolution of the initial set A. Verbally, this equation expresses that in mixing systems, the ratio of the "overlap" between a time evolved set and any

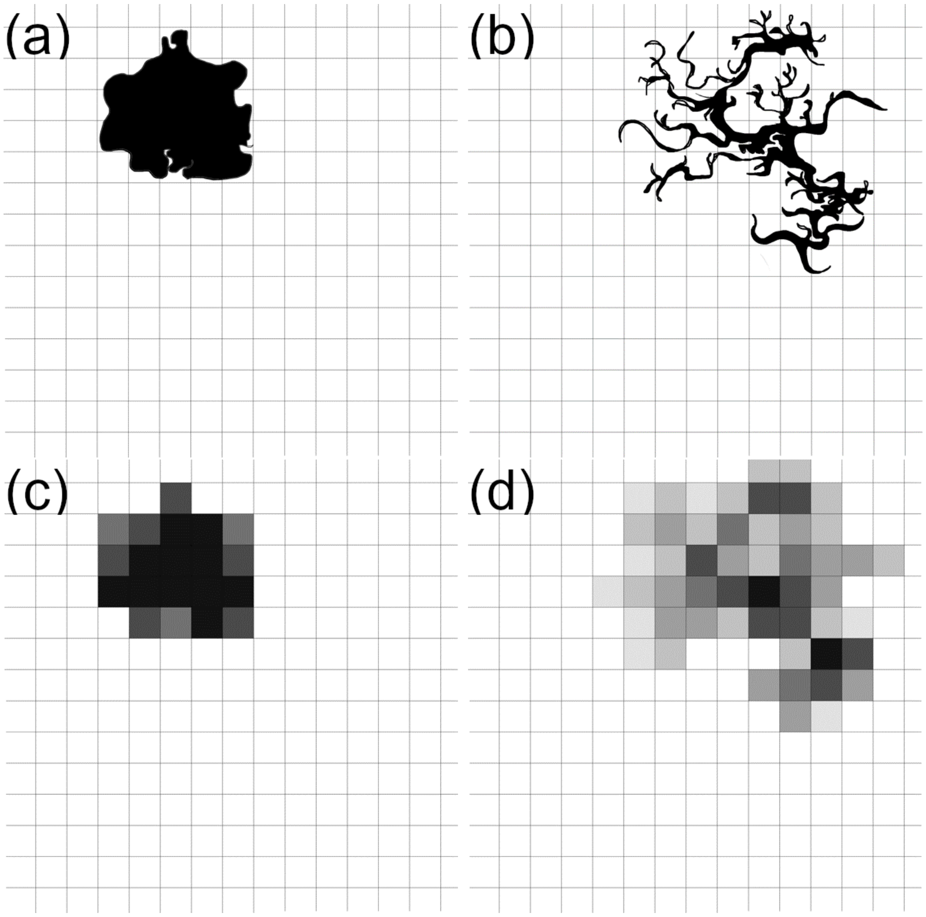

Figure 6.1: The evolution of a probability density under chaotic dynamics in a (a)-(b): fine grained phase space; (c)-(d): coarse grained phase space.

other subset of phase space to the measure of the unevolved set will, with enough time, approach the "overlap" between that subset and phase space itself. In other words, the initial set A will evolve into a set A_t which is distributed completely evenly throughout phase space. This definition requires the dynamics to be measure-preserving, and describes the closest approach to a uniform probability density such systems can muster. The initial set A, in a mixing system, will spread out in fine, filigree-like filaments through phase space, so thin and so far-reaching that all subsets of phase space, no matter how small, contain the same proportion of A. This process is illustrated graphically in Fig. 6.1a-b. In c-d, I have performed coarse-graining, restricting the resolution to the squares and representing the fractional occupation by the initial set within the squares with the shading. In a mixing system, as $t \to \infty$, all of these squares (no matter how big or small they are, so long as they're finite), will become the same shade.

It is obvious that a mixing system is necessarily ergodic. A general condition for ergodicity is unavailable, and it comes as no surprise that mixing systems too have no known general condition. The higher rungs of the ergodic ladder, Kolmogorov systems and Bernoulli systems [101], are not so easily explained intuitively. So I shan't bother.

For our specific purposes, we note that dynamical instability is also related to the FL. The FL is a dynamical transition between states with very different phase space dynamics - below the line the configuration space is full of local minima which temporarily confine particles, whereas above the line the phase space is much more open.

Dynamical instability arises in highly nonlinear systems which are not very amenable to microscopic solutions. There is however a very simple and intuitive way to quantify the dynamical instability of a system, which is the Lyapunov spectrum. Lyapunov spectra measure the rate of divergence of neighbouring trajectories in phase space. Consider a point $\Gamma(0) \in \mathscr{M}$ at time $t = 0$, and a perturbation of it in the ith phase space coordinate: $\Gamma(0) + \delta\Gamma_i(0)$. If the dynamics are unstable, this perturbation will rapidly grow and erase correlations between the two trajectories. The state at time $t = \tau$ can be written $\Gamma(\tau) + \delta\Gamma(\tau)$, where $\Gamma(\tau)$ is the time-evolved unperturbed trajectory, and $\delta\Gamma(\tau)$ will, in general, spread into many or all other phase space dimensions. The assumption of the Lyapunov spectrum is that this perturbation grows exponentially with time:

$$|\delta\Gamma(\tau)| = |\delta\Gamma(0)| \exp(\Lambda\tau). \tag{6.1.2}$$

More specifically, we must define this for each phase space coordinate:

Definition 6.1.1 (Lyapunov Exponents) *The Lyapunov exponents characterise the exponential divergence of a perturbation in each coordinate of phase space:*

$$\lambda_i = \lim_{t\to\infty} \frac{1}{t} \log\left(\frac{|\delta\Gamma_i(t)|}{|\delta\Gamma_i(0)|}\right). \tag{6.1.3}$$

The collection of Lyapunov exponents is called the Lyapunov spectrum.

The Lyapunov spectrum therefore defines the directions in which phase space contracts and expands under time evolution. The sum of Lyapunov exponents is related to the rate of contraction of phase space and thus vanishes for Liouvillean flows [101]. Just one positive Lyapunov exponent will cause dynamical instability, and the nature of exponential growth means that the total perturbation size, $\frac{|\delta\Gamma(t)|}{|\delta\Gamma(0)|}$, will be dominated by the largest positive Lyapunov exponent, Λ say. We can therefore write:

$$\Lambda = \lim_{t\to\infty} \frac{1}{t} \log\left(\frac{|\delta\Gamma(t)|}{|\delta\Gamma(0)|}\right). \tag{6.1.4}$$

This quantity is frequently called the maximal Lyapunov exponent (MLE). There are a few things to be careful with, however. One can immediately spot that if $\delta\Gamma(0)$ lies along the phase velocity tangent the perturbation will never grow. More generally, Λ will depend both on the perturbation $\delta\Gamma(0)$ and the point which is perturbed $\Gamma(0)$. Along a given trajectory, the value of Λ will depend on where the perturbation is taken. In practice we will take the average $\overline{\Lambda}$ over a trajectory. In an ergodic system, this average will be the same as the phase average, but assuming that under this context would be a bit rich. So we'll be taking averages over initial conditions too, to make sure.

The MLE has its most accessible explanation by taking its reciprocal to get the *Lyapunov time.* The Lyapunov time represents the characteristic time period over which

Dynamical System	Lyapunov Time
Solar System	5 million years
Pluto's Orbit	20 million years
Hydrodynamic chaotic oscillations	2 seconds
1 cm^3 of argon at standard conditions	3.7×10^{-11}s
1 cm^3 of argon at its triple point	3.7×10^{-16}s

Table 6.1: Lyapunov times of different dynamical systems [101].

Dimension	Symbol	Reduced form
Length	r	$r^* = r/\sigma$
Time	t	$t^* = t\sqrt{\epsilon/(m\sigma^2)}$
Energy	E	$E^* = E/\epsilon$
Concentration	n	$n^* = n\sigma^3$

Table 6.2: Definitions of the dimensionless reduced units in the LJ potential.

a perturbed trajectory decorrelates with the unperturbed trajectory. It is of practical importance, because it measures the growth rate of errors associated with imperfect measurements. After the Lyapunov time has passed, these errors have grown by a factor of e. The Lyapunov times for several dynamical systems, reported in Ref. [101], are listed in Tab. 6.1.

Dynamical instability is a key feature of chaotic systems. Indeed, chaotic systems are necessarily mixing systems, but there is an understanding that chaotic systems must exhibit additional interesting features, such as dense periodic orbits or strange attractors. Many mixing systems happen to exhibit such features anyway. Chaos theory is a multidisciplinary approach to dynamically unstable systems which appear in physics, climate, computer science, ecology, and many other fields. I use the language of ergodic theory in order to add to this field by investigating dynamical instability in the supercritical state and across the FL [102].

6.2 Molecular Dynamics Simulations

Here I use a much smaller system than before, consisting of 256 atoms under periodic boundary conditions which interact with each other according to the LJ potential 3.2.4 with potential parameters corresponding to argon, listed in Tab. 3.3. I choose argon because it is a system which has been well-characterised over the FL [50, 76, 103]. The critical point of argon is 48.6 bar and 151 K. The phase diagram of argon including the Frenkel line is depicted in Fig. 6.2. In this work, in line with existing work on Lyapunov exponents in MD, I used reduced units for the LJ potential which puts everything in terms of the physical parameters which characterise the model. The definitions of the relevant dimensionless reduced units are given in Tab. 6.2.

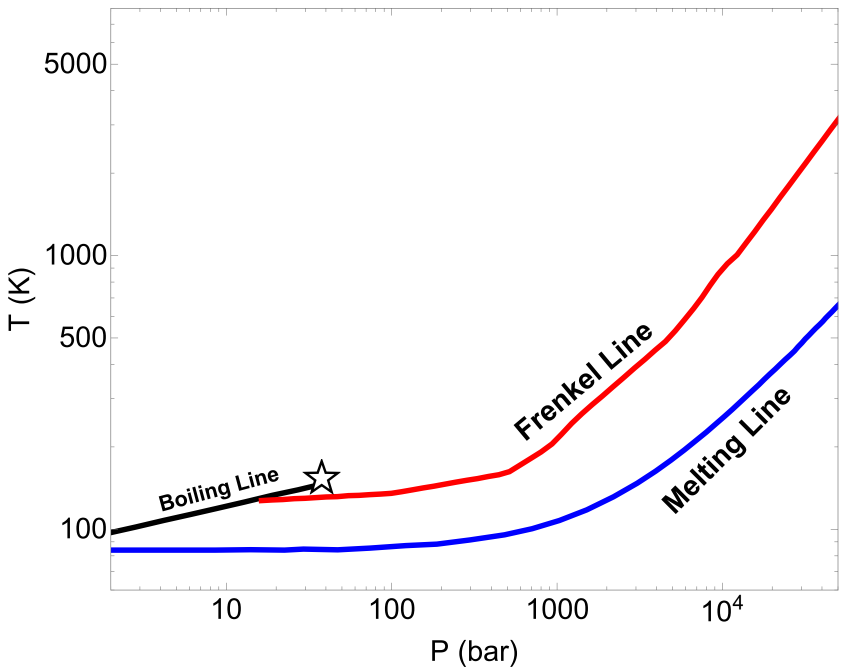

Figure 6.2: The phase diagram argon, showing the Frenkel line with reference to the boiling line and melting line. The star represents the critical point.

This work involves small perturbations and measuring their growth. MD simulations are not exact, and become less so when a larger timestep is employed. Obviously sensitivity of the results that follow to choice of timestep is something which must be watched out for. Timesteps, therefore, between 1 and 0.01 fs were employed, with all results showing no sensitivity to this choice.

I prepared an initial configuration of 256 argon atoms in a cubic cell with FCC crystal structure at four different lattice constants: 6.428, 6.049, 5.747 Å. These correspond to reduced concentrations of 0.7101, 0.8284, and 1.065 respectively. Densities and concentrations of these isochores are given in standard units, alongside the temperatures and energies in reduced and standard units of the FL calculated by the VAF criterion, in Tab. 3.3. Structural equilibration, including melting where applicable, was performed in the NVT ensemble with the Langevin thermostat for 200 ps, at temperatures ranging from 20K in the crystalline state to 10,000K in the deeply supercritical state. Equilibrated configurations were fed into NVE dynamics for a further 200 ps, from which statistical data such as VAFs were collected.

The final configurations of these NVE runs were used as the initial configurations of the production runs in which the MLEs were calculated. The procedure used to calculate the MLE is called the tangent space method [104], and operates as follows. An initial configuration is perturbed by a very small amount in *all* phase space directions. Practically this amounts to shifting the x, y, and z coordinates and velocity components of each particle in as small a manner as is allowed by the numerical precision of DL_POLY. It's crucial that the perturbed and unperturbed trajectories lie on the same phase space

n^*	0.7101	0.8284	1.065
ρ (g/ml)	1.199	1.403	1.798
n (Å^{-3})	0.01807	0.02108	0.02710
T_{F} (K)	295	997	3850
T^*_{F}	2.45	8.33	32.0
E_{F}/N (eV)	-0.00432	0.116	0.650
E^*_{F}/N	5.28	16.9	69.0

Table 6.3: Thermodynamic data for each system investigated: ρ - density; n concentration; T_{F} - temperature at the Frenkel line; T^*_{F} reduced temperature at the Frenkel line; E_{F}/N - energy per particle at the Frenkel line; E^*_{F}/N - reduced energy per particle at the Frenkel line. The reference energy is $E^*/N = 0$ at $n^* = 0.5917$ and $T^* = 0.5$ (20 K).

energy hypersurface, so velocities of the perturbed configuration are rescaled such that the change in energy from the perturbation is eradicated and the states lie on the same hypersurface. The perturbed and unperturbed systems are then evolved according to Hamilton's equations for a certain period of time. This period varied from 0.25ps to 2ps, with no sensitivity in the results to follow on this choice. The MLE is then calculated according to Eq. 6.1.4 and recorded. Next, the perturbation $\delta\Gamma(t)$ is projected along itself with a resulting magnitude equal to $|\delta\Gamma(0)|$. Mathematically:

$$\delta\Gamma_{\mathrm{new}}(0) = \delta\Gamma(t)\frac{|\delta\Gamma_{\mathrm{old}}(0)|}{|\delta\Gamma(t)|}. \tag{6.2.1}$$

The new perturbation and the original trajectory are both evolved, and another MLE is recorded. This procedure was repeated until 100 MLEs were recorded. The MLEs recorded this way are insensitive to initial perturbation size within a reasonable range. The MLEs recorded were averaged to give the time average of the MLE, $\overline{\Lambda}$, for each given trajectory. I calculated the same values of $\overline{\Lambda}$ (within statistical fluctuations) under different initial conditions produced by differently seeded initial velocity distributions. I will therefore comfortably refer to both $\overline{\Lambda}$ and the phase average $\langle\Lambda\rangle$ by the same symbol, Λ, from here on out.

6.3 Results

We begin by investigating the transition at the melting line. We can comfortably agree that this transition is reasonably well-understood, and it can act as a forward base from which we can understand what's happening at the FL. The reduced energy per particle as a function of temperature is plotted in Fig. 6.3. The disconinuity of energy across the melting line due to the latent heat of fusion allows us to discern the location of the melting line when we plot the MLE versus the reduced energy in Fig. 6.4. I prefer to plot the MLE as a function of energy because energy is a microscopically unambiguous quantity about which the phase space is aware. Energy defines a hypersurface, whereas temperature is a statistical quantity best defined for large systems. We see a discontinuity in the MLE

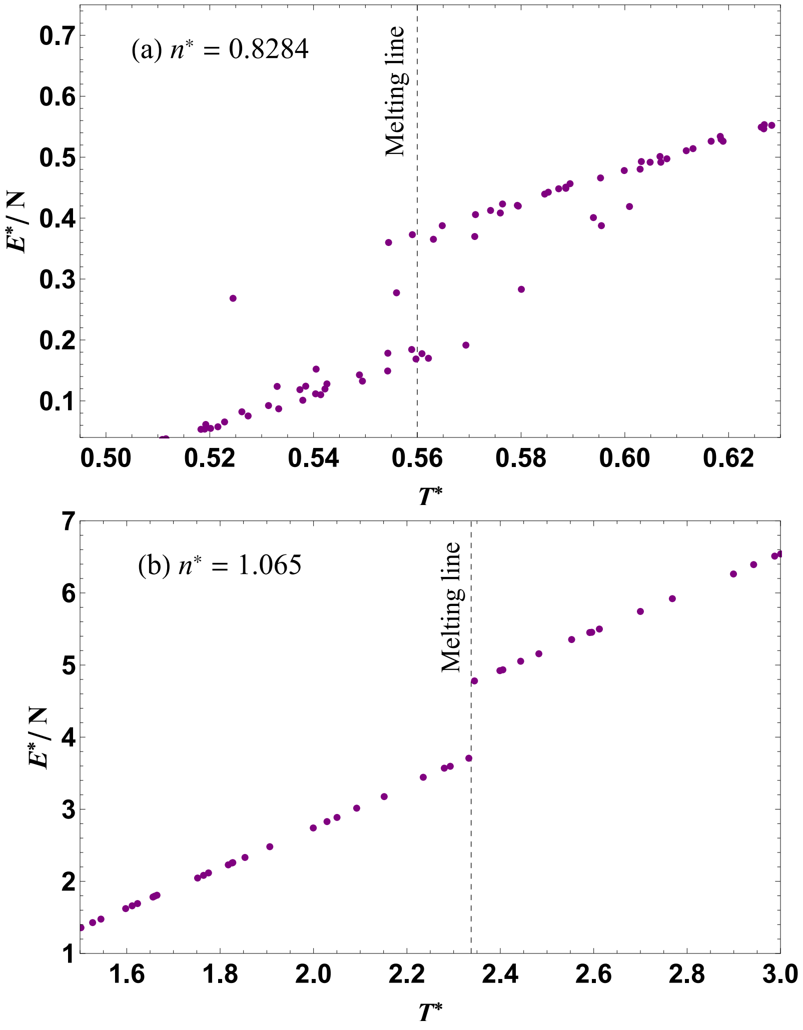

Figure 6.3: Reduced energy per particle $\frac{E^*}{N}$ across the melting line at reduced concentrations of (a) 0.8284 and (b) 1.065.

across the melting line, which has been previously documented [105, 106, 107, 108, 109]. This gives us confidence that my calculations are correct. I note that the transition in energy and MLE is not very clear, particularly at the sparser of the two isochores. This is because I set the energy of each simulation densely across the transition which causes some degree of superheating in the crystalline state or supercooling in the liquid state. This is especially true with a small system size of 256 atoms. Nonetheless the discontinuity is very clear. I further note that the lowest concentration, $n = 1.199$ g/ml ($n^* = 0.7101$), is much below the concentration at the triple point, 1.417 g/ml. This means that at temperatures immediately below the triple point temperature (83.8 K) the state is a solid gas mixture, and the state at temperatures immediately above it is a liquid gas mixture. Though there is some degree of this at the concentration of 1.403 g/ml, at the lowest concentration the transition in the MLE is obfuscated completely. For this reason I omit this plot.

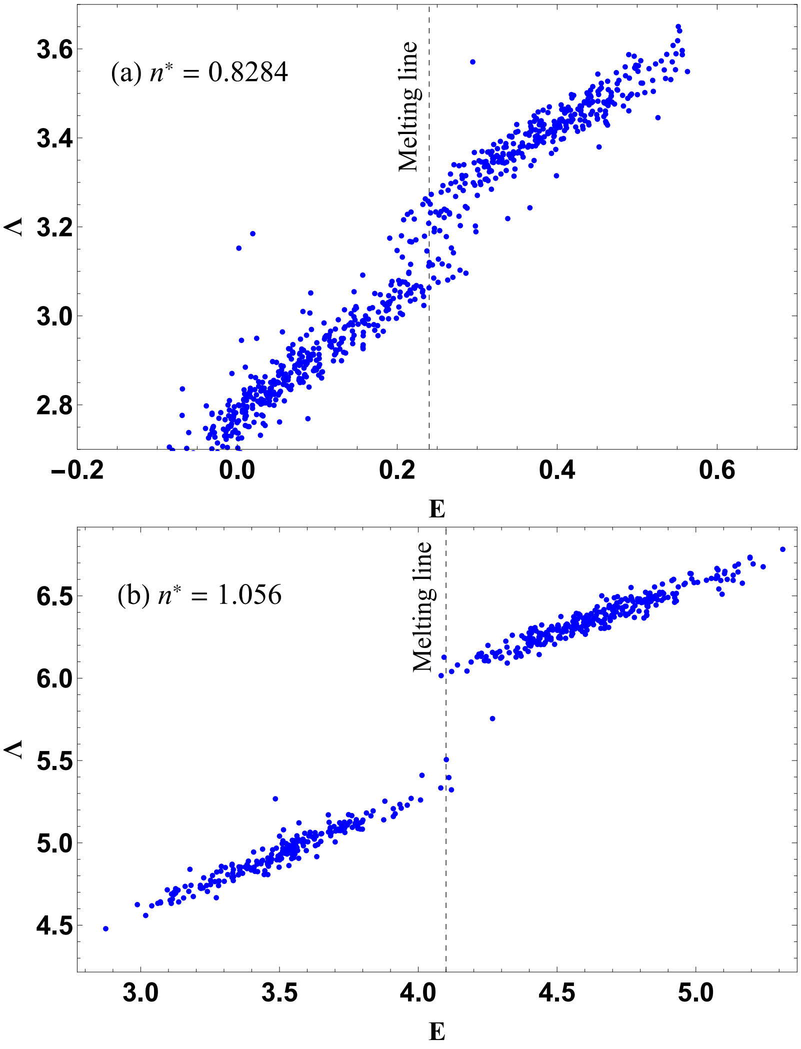

Figure 6.4: Maximal Lyapunov exponent Λ across the melting line at reduced concentrations of (a) 0.8284 and (b) 1.065.

The next matter was to calculate the FL along the isochores. VAFs along the isochores are plotted in Fig. 6.5. As can be seen, the disappearance of the minima happens fairly promptly at lower densities. At the highest density, however, a very slight minimum remains for a temperature range that spans almost 1000 K. The zoomed-in inset of Fig. 6.5c shows the gradual disappearance of this minimum. The VAFs in this inset are almost indistinguishable at the lower resolution of the main figure despite differing significantly in energy. This means that after most atomic oscillation is dispersed, a very slight component disappears far more gradually, which happens because the system density is fixed at a high value. In this sense, the system is almost completely diffusive and "gas-like" far before the disappearance of the minimum, and the last leg of the transformation takes place much more slowly. Energies and temperatures at the FL are listed in Tab. 6.3.

Finally we look at the MLE plots for the three isochores extending deep into the supercritical state. Fig. 6.6 plots the MLE as a function of reduced energy, up to and beyond the FL. We also include the thermodynamic definition of the FL, $c_V = 2k_{\mathrm{B}}$, as an alternative marker of the dynamical crossover. The high-temperature functional dependence of the MLE is clearly visible with the logarithmic axes: $\Lambda = a(E^*)^b$. The data are fitted to this relationship and the fitted parameters are reported in Tab. 6.4. At lower densities, the crossover to this power-law relationship closely coincides with the both the dynamical crossover at the FL and the thermodynamic crossover at $c_V = 2$. At the highest density, the dynamical crossover occurs deep within this power-law regime. However we note, as discussed above, a very small minimum in the VAFs disappears in the energy range of $E^*/N \approx 40$ to $E^*/N \approx 68$ (this is a larger range than that between the melting line and FL at the other densities), which corresponds to a very minor component of molecular oscillation disappearing in this range. For the most part, atomic oscillation gives way to diffusion at much lower energies than the disappearance of the minimum, represented in Fig. 6.6 by the gradual approach to the power-law relationship as oscillatory modes disappear.

n^*	0.7101	0.8284	1.065
a	2.727	2.747	2.798
b	0.4856	0.4944	0.5040

Table 6.4: Fitted parameters for the power law relationship $\Lambda = a(E^*)^b$ along the three different isochores.

6.4 Discussion

Chaotic dynamics have received ample attention in physics beyond theoretical considerations. Lyapunov exponents have been used to calculate transport properties in fluids, such as viscosity [110, 100, 111, 112]. Additionally, the ability of digital computers to faithfully represent the dynamics of chaotic systems is an increasingly important question (for a particularly striking example of a digital computer's failure, see the recent

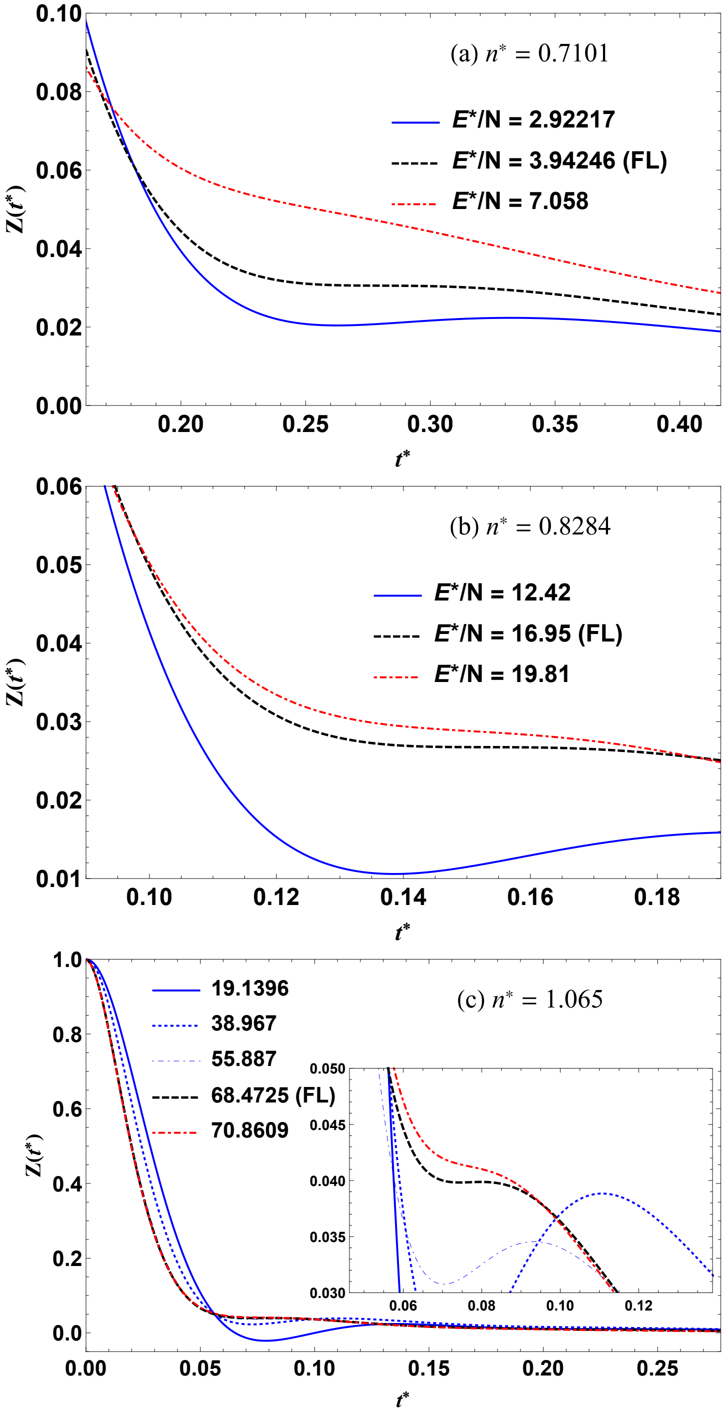

Figure 6.5: Velocity autocorrelation functions as a function of reduced energy per atom and reduced time $Z(t^*)$ at the four different concentrations.

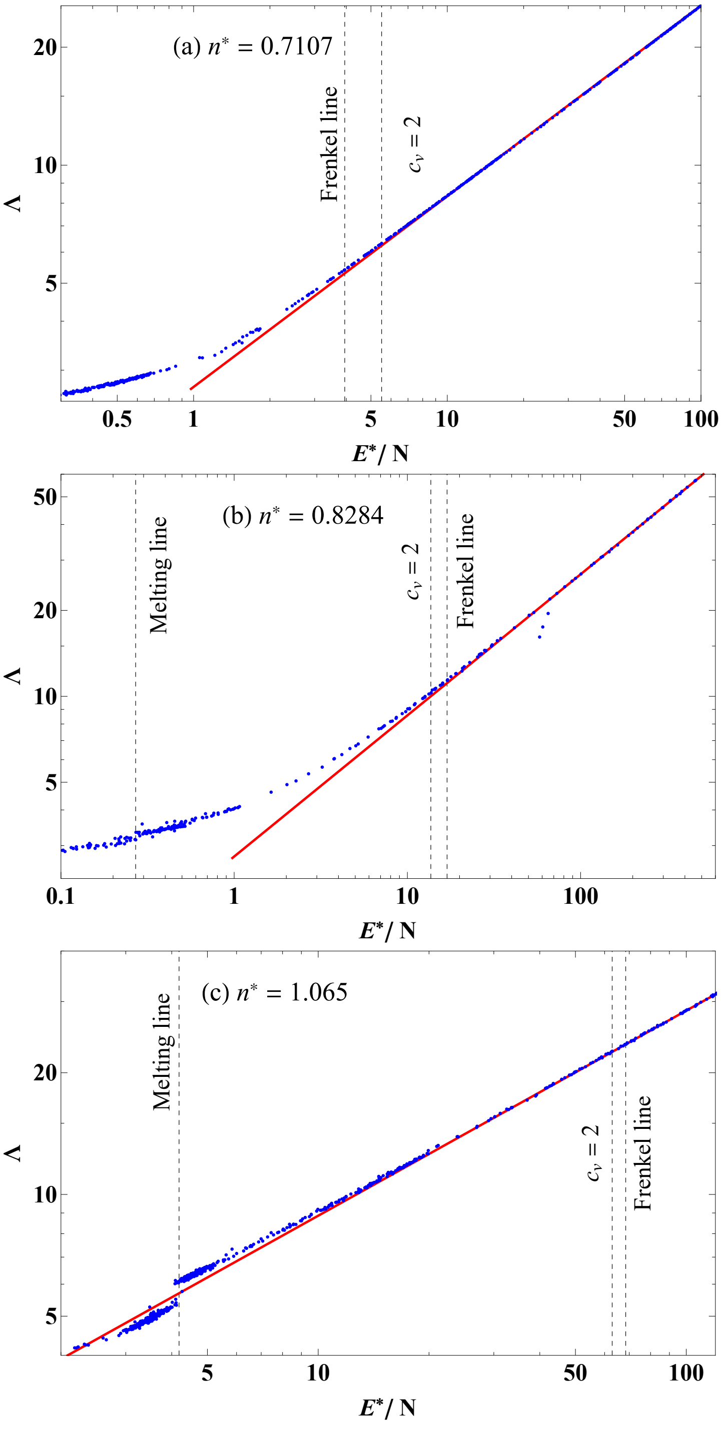

Figure 6.6: Maximal Lyapunov exponent Λ in the fluid state at reduced concentrations of (a) 0.7107; (b) 0.8284; (c) 1.056. The red lines are fitted power-law relationships $\Lambda = a(E^*)^b$. The fitted values are reported in Tab. 6.4. The energy scale in (c) is curtailed in order for the resolution to allow the deviation from the power law at low energies to be visible.

work [99]), and the Lyapunov spectrum has been proposed as a natural measure of the deviation of the calculated trajectory from the "true" one [113].

One of the seminal examples used in chaos theory is the Lorentz gas [114], which models an ideal gas in the dilute limit, and whose Lyapunov exponent is well-known [101]. On the other hand, the Lyapunov spectrum of condensed phases have also been well studied in the condensed phase using MD simulations [115, 105, 106, 107, 108]. The behaviour of Lyapunov spectra across phase transitions has been documented [105, 106, 107, 108, 116, 117, 109, 118], exhibiting discontinuities in the MLE itself or its first derivative with respect to an order parameter. Phases are an ultimately macroscopic notion, but particle dynamics and phase space properties like Lyapunov spectra can both provide a quantitative *microscopic* description of the phases and the transitions between them, motivating our line of inquiry.

The transition of Λ in the supercritical state behaves as one might expect. The discontinuity in Λ across the melting line is due to the discontinuous opening up of phase space upon melting. Opening up here means that trajectories are more able to wander through different parts of phase space, as atoms migrate between quasi-equilibrium positions about which they oscillate. The effect on the momentum subset of phase space offers no discontinuity assuming that equipartition holds or nearly holds. It's difficult to picture this opening up of phase space, but the effect on the Lyapunov exponents is clear. In the crystalline state, where atomic diffusion events are extremely rare, a perturbation in a trajectory will cause particles to bounce off each other in different ways and will result in a slightly different position in the configuration subset of phase space. In a liquid however, where diffusion events are commonplace, a perturbation in a trajectory will cause migrations which would otherwise not have happened, or prevent migrations which otherwise would have. This results in a substantial increase in dynamical instability in the liquid state compared to the solid state, and since the change in dynamics is discontinuous, so too is the discontinuity in Λ. The dynamical transition at the FL is not fully understood, but any discontinuity must be small enough to have gone undetected for two centuries. The gradual transition from one regime into another is therefore in line with our understanding of the changes which take place in phase space across the FL.

A power law with *temperature* for the MLE has been observed in a diverse range of condensed matter systems [119, 120, 121], though at far lower temperatures than those probed in this study. Our understanding of the FL informs our explanation of the power law found in the supercritical state. Between the melting line and the FL, as the relaxation time τ_F decreases, the MLE increases with energy. This increase is caused by the increasing prevalence of diffusion events, which contribute significantly to dynamical instability as explained above. This regime terminates smoothly as τ_F approaches the atomic oscillation period and a local rigid structure can no longer be defined. Above the FL where diffusion is continuous rather than abrupt, the events of chief dynamic sensitivity are now the collisions of kinetic theory - collisions involve sudden changes in velocity, and in turn lead to other collisions. The distinction between collision and diffusion is not sharp at and close above the FL, but the dynamical state is very clearly different from below, with atoms migrating without a continuous impediment, but encountering resistance when they meet other atoms head-on. An altered trajectory will lead to a very different cascade of collisions. Scattering is what makes the Lorentz gas a chaotic dynamical system [114]. These collisions now determine the evolution of the MLE without contribution from diffusion events, which is why it follows a single functional form. The collisions become more frequent with temperature at a fixed density. For a hard-sphere gas, the mean collision rate is [122]

$$w_{\mathrm{coll}} = n\pi\sigma^2\sqrt{\frac{6k_{\mathrm{B}}T}{m}}. \tag{6.4.1}$$

This is a concave function of temperature (and thus energy), which is a property exhibited by the MLE at all densities (the gradient in the log-log plots in Fig. 6.6 is less than unity). At the lower densities, this power-law regime spans more than an order of magnitude of energy above the FL. The fluid at the highest density, even well below the FL, is mostly dominated by diffusion and collisions, but there is a transitory period of oscillation for some molecules. We can interpret that collisions are responsible for the bulk of dynamical instability in these states, but a small fraction of atoms at any given time undergoing oscillation do not contribute to dynamical instability in this way. This crossover period of small deviation from the power law is much smaller at lower densities.

Fig. 6.7 summarises my main interpretations of these results. In the crystalline state motion is only oscillatory and atoms oscillate within effectively permanent cages, which means dynamical instability is relatively low. Dynamical instability increases with temperature simply because mobility increases with temperature and atoms have access to more of configuration space and momentum space. Across the melting line, atomic motion combines oscillation with occasional diffusion events. Diffusion events are another source of dynamical instability, and the evolution of the MLE has contributions from both of these dynamical events. As temperature increases, the relaxation time decreases and diffusion events become more common, accelerating the growth of the MLE. As the FL is approached and diffusion events become very common, a new type of event can be described. Collisions involve rapid accelerations of particles whose kinetic energies dwarf the potential energy of their environment. Therefore between the melting line and the FL, the evolution of dynamical instability is caused by oscillation, diffusion, and collisions, the contributions of each of which will evolve differently with energy. This, the liquid's mixed dynamical state, precludes a simple functional relationship between Λ and E. Above the FL, oscillation is no more and diffusion becomes commonplace. Indeed, all atoms are always diffusing and the evolution of dynamical instability is no longer fed by the increasing frequency of diffusion events. Instead, what becomes more prevalent is high-velocity collisions between atoms which cause rapid changes in position and momentum, which in turn cause an increase in dynamical instability. Since there is no longer any oscillation or diffusion, the dynamical instability evolves only according to these simple gaslike dynamics, and it turns out that this evolution is a power law with energy. This is much akin to the justification for a thermodynamic crossover at the FL - below the line the evolution of energy is defined by the disappearance of oscillation and the increasing frequency of diffusion, above the line diffusion is ubiquitous and energy changes based on how far atoms go between collisions.

Thinking of liquids as mixed dynamical states has provided much insight [41] in recent years, and crossovers in thermodynamics and structure have been predicted and

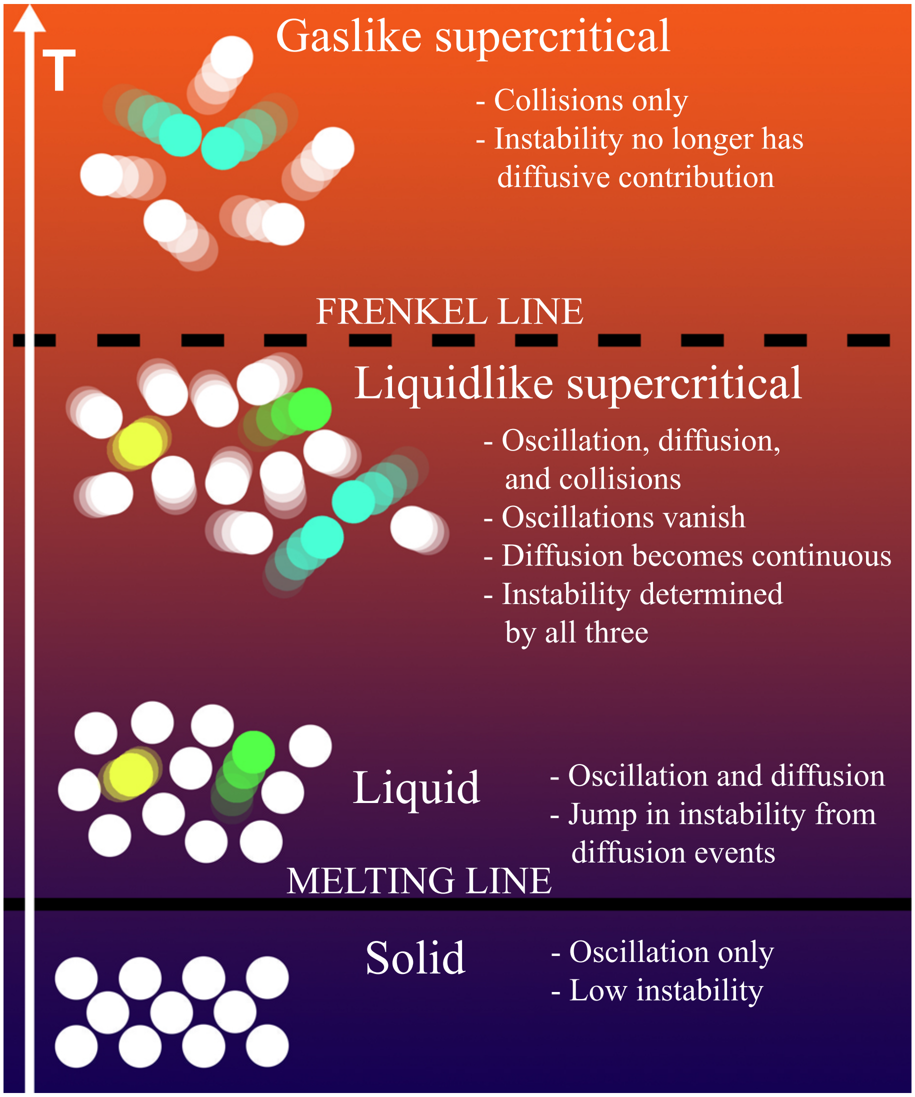
T
Gaslike supercritical
- Collisions only
- Instability no longer has diffusive contribution
FRENKEL LINE
Liquidlike supercritical
- Oscillation, diffusion, and collisions
- Oscillations vanish
- Diffusion becomes continuous
- Instability determined by all three
Liquid
- Oscillation and diffusion
- Jump in instability from diffusion events
MELTING LINE
Solid
- Oscillation only
- Low instability

Figure 6.7: Summary of our main results: Evolution of dynamical instability in condensed matter, from solids at low temperature to gaslike supercritical fluids at high temperature. The figure shows the dynamical regimes in each state of matter (oscillation, diffusion, collisions) and their relationship to the dynamical instability. Yellow atoms are oscillating, green atoms are diffusing, and cyan atoms are colliding.

discovered (including in this thesis, at least for simulations!) on the basis of these considerations. The Lyapunov spectrum is very sensitively linked to dynamics, much moreso than thermodynamics or structure, and has been used in the past to indicate changes of phase [105, 106, 107, 108, 116, 109, 118]. Our results therefore do not only help to understand microscopic chaos in the supercritical fluid state, but also show that this depiction of liquids as dynamically mixed states and the idea of the FL which separates regions in the supercritical part of the phase diagram are very deep and fundamental physical ideas which are supported directly by properties of the classical phase space itself.

Chapter 7

The “c”-transition

7.1 The Nature of the Frenkel Line

From the very beginning of this project, a key topic for exploration was the nature of the transition at the FL, in order that we might discern whether a sort of phase transition was operating in the supercritical state. A phase transition, should one take place, is likely to manifest in the isochoric heat capacity, c_V. The heat capacity is one of a system’s most fundamental thermodynamic properties because it measures the change in entropy and degrees of freedom under increase of thermodynamic temperature. As described, the transition at the FL is all about the evolution of degrees of freedom: below the FL the phase is defined by the disappearance of long wavelength transverse collective modes via the domination of oscillation by diffusion; above the FL the phase is defined by the disappearance of short wavelength longitudinal modes (the only type remaining) due to the increasing distance atoms travel unperturbed. How exactly the phase evolves between these extremes, however, is unknown. It is likely smooth, but then the higher order derivatives of c_V could still contain anomalies, and accessing the theoretical description of these derivatives in terms of the Frenkel picture is troublesome.

On the other hand, the transition might be better understood if the parameters which characterise c_V itself were themselves better understood close to the FL. Towards this end, we explored a multitude of ideas related to order parameters and characterising τ_F in the vicinity of the FL where it becomes ill-defined. The idea that something related to the shear modulus G or the number of propagating transverse modes could be an order parameters was something we considered for a long time. All our approaches suffered from the inability of our theoretical models to accurately characterise a fluid near the FL. The collisions of the gaslike state and the diffusive jumps of the liquidlike state, which define the mean free path l_FP of kinetic theory and the relaxation time τ_F of Frenkel theory respectively, are both unclear in the states around the FL where the liquid is so mobile that atoms spend as much, or more, time diffusing as they do oscillating or where the gas is so dense that atoms spend no significant time without being perturbed significantly by another atom. It was while trying to find an unambiguous operational definition of τ_F and comparing it to τ_M that I discovered what we have called the “c”-transition.

This transition operates in the deep supercritical state, far from the critical point. As mentioned, transitions in this state of matter are traditionally thought not to exist so far from any other known phase transition. In this work, we conduct the widest and most detailed survey of the supercritical state heretofore undertaken. We investigate states up to 330 times the critical temperature and 8000 times the critical pressure, scanning the phase diagram along isobars, isotherms, and isochores.

This is a story I want to tell chronologically, so I shall drive straight into simulation details and discuss motivation concurrently.

7.2 Molecular Dynamics Simulations - Argon

As is traditional in the field of liquid physics, we perform our fundamental probings into a conceptually and practically simple system, in this case argon, just as I did in the work on chaos [102]. Argon is pleasing theoretically and practically due to its simple energetics. The only potential energy is the Lennard-Jones pair potential, with no need to worry about charges or internal degrees of freedom. Furthermore, the weakness of the LJ potential at long range means that argon becomes very close to an ideal gas at accessible temperatures and pressures, suiting our analysis.

As in the previous chapter, initial configurations of argon were prepared in an FCC crystal structure. In this study, I have used systems of 500, 4000, 27000, and 108000 atoms, finding no significant dependence of any results on system size. These systems were subject to equilibration along three different isobars, isotherms, and isochores. Pre-equilibration was performed, as I did in water and carbon dioxide, in the NPT ensemble in order to produce equilibrium densities for the isobars and isotherms. After that, the NVT ensemble produced equilibrium structures which served as the initial conditions for the production runs, which took place in the NVE ensemble.

While working on definitions of τ_{F} accessible to molecular dynamics, I compared it to the Maxwell relaxation time τ_{M} which provides the macroscopic link to Frenkel theory, as seen in our discussion of generalised hydrodynamics. Calculating this quantity is non-trivial, even if the equations involved seem simple. For convenience, I repeat relevant equations here:

$$\eta(\omega \to 0, k) = \tau^{\mathrm{T}}(k) G_{\infty}(k) \tag{2.1.87}$$

$$G_{\infty}(k) = \frac{V}{k_{\mathrm{B}}T}[\tau_{zx}(0, \mathbf{k}), \tau_{zx}(0, \mathbf{k})], \tag{2.1.74}$$

$$\eta = \frac{V}{k_{\mathrm{B}}T}\int_0^{\infty} \mathrm{d}\tau [\tau_{zx}(0), \tau_{zx}(\tau)], \tag{2.1.68}$$

$$\tau_{\mathrm{M}} = \frac{\eta}{G}. \tag{2.1.95}$$

The path, then, seems clear. Using molecular dynamics we can calculate the Maxwell relaxation time as follows:

$$\tau_{\mathrm{M}} = \int_0^{\infty} \mathrm{d}\tau \frac{[\tau_{zx}(0), \tau_{zx}(\tau)]}{[\tau_{zx}(0), \tau_{zx}(0)]}, \tag{7.2.1}$$

having omitted the $k-$dependence of G_∞ to get its "macroscopic" form. This reiterates the meaning of the Maxwell time in a microscopic manner - it measures the normalised autocorrelation of fluctuations in shear stress.

Actualising Eq. 7.2.1 is slightly problematic, however, in an MD simulation due to the integral. We can calculate the autocorrelation function easily enough using Eq. 3.3.3 from the $k \to 0$ limit of the instantaneous stress tensor [8] which we periodically record from the trajectory into a time series, but integrating such a function is dangerous. The reason for this is that at long times, an autocorrelation function becomes very noisy around zero as correlations truly have decayed to insignificance. If the integral is performed into this region of noise around zero, what we are effectively doing is performing a random walk. The expectation of a random walk is zero displacement, of course, but the variance of the walk grows linearly with integration time. This means that integrating just one trajectory will cause the viscosity, and thus τ_M, to wander, rather than settle, if the tail of the autocorrelation function is integrated over too long a time. Better statistics acquired by averaging over a longer MD trajectory does not solve this problem, as there is a minimum to fluctuations [7] and integrating these fluctuations will always cause wandering. This is a known problem, and there are a few ways that people deal with it [123]. One method is simply to terminate the integral as soon as it first hits zero. This is a better strategy than it sounds, at least for fairly inviscid fluids where shear stress decorrelates very quickly and the initial drop captures most of the integral. However it's a bit presumptive, best used once a better method has verified it to be possible. Another option is to take the autocorrelation function and fit it to something analytic which can be integrated analytically. This is again presumptive, forcing an outcome by our choice of fitting function.

The approach I took, and to be sure, that many others have taken, was to simulate multiple trajectories at the target conditions with different initial conditions, calculating the stress autocorrelation function for each of them. The integral of each autocorrelation function is tantamount to performing a random walk, but averaging over such walks will eliminate the drift and retrieve the true steady state value. Using different initial conditions in this way much more efficiently reduces noise than a single long trajectory because all the states in the new time series are completely uncorrelated, rather than simply adding more states onto the end of an existing time series. Viscosities calculated in this way were insensitive to system size, from 500 to 108000 atoms, consistent with earlier findings [124].

Values of viscosity and isochoric specific heat capacity (in units of k_B) across several different phase diagram paths are plotted with experimental values in Fig. 7.1. Viscosities and heat capacities plotted this way were calculated from NVE production runs of 1000000 timesteps (1 ns) and averaged over 20 different initial conditions. Heat capacity was calculated using Eq. 3.3.12. Values of viscosity and the shear modulus were averaged over the three independent off-diagonal components of the stress tensor. Experimental values of c_V and η at lower pressures come from NIST, and higher pressures come from Ref. [125]. The agreement here is good at both high and low pressures, demonstrating that the calculations of viscosity here are adequate. The agreement with NIST diminishes at higher pressures, but given the good agreement with the data from Ref. [125] it seems likely that this discrepancy is due to the lessened reliability of NIST data at higher pressure on account of extrapolation.

Viscosity is an informative quantity when considering the dynamics of liquids and gases, and in order to tell our story it is helpful to plot $c_V(\eta)$. Along isobars and isochores, $c_V(\eta)$ has clear turning points due to corresponding minima in η, whereas no such minima exist along our isothermal paths. We observe strong path dependence in the interrelation between c_V and η, and will return to the issue of path dependence below. Here we note the earlier work [126] relating viscosity to excess entropy calculated from the virial expansion at low density. This relation was discussed on empirical grounds and is unrelated to excitations in the system considered by Frenkel theory.

Next we examine the dependence of c_V on τ_{M}. This is the key physical property in the Frenkel picture of liquids and its relationship with c_V should contain information on the nature of the crossover. We begin with the evolution of τ_{M} along the nine phase diagram paths, all of which cross the FL. This evolution is plotted in Fig. 7.3. We note that despite all paths crossing the FL, τ_{M} experiences rather extreme path dependence in that it has minima aong isobars and isotherms but not along isochores. We recall that Frenkel's theory relates τ_{M} to the average time between molecular rearrangements in the liquid [2]. Backed by experiments and modelling [127, 128], this relation has since become an accepted view [40].

In the liquidlike regime, τ_{M} decreases with temperature. In the gaslike regime, shear momentum transfer takes place via the collisions of kinetic theory (as discussed in the previous section), and a relaxation time is therefore interpreted as the mean time between collisions in this regime [2, 4]. In the same way that the liquid relaxation time, which qualitatively describes the frequency of abrupt diffusive atomic motion, can be related to τ_{M}, we postulate here that in the gaslike regime the gas relaxation time, which qualitatively describes the frequency of abrupt collision events, can too be related to τ_{M}. It stands to reason that τ_{M} would be related to this collision frequency, after all it isn't obvious that there could be two separate relaxation timescales operating in the gaslike regime, but I will also provide a mathematical argument for this identification. I summon the Zwanzig and Mountain formula for the infinity frequency shear modulus for a monoatomic fluid with pairwise interactions $\varphi(r)$ [129]:

$$G_\infty = nk_{\mathrm{B}}T + \frac{2\pi n^2}{15}\int_0^\infty \mathrm{d}r\ 4\pi r^2 g(r)\frac{\mathrm{d}}{\mathrm{d}r}\left[r^4\frac{\mathrm{d}\varphi(r)}{\mathrm{d}r}\right]. \tag{7.2.2}$$

The ideal gas limit of any system is achieved by setting the interaction term to zero, which reduces G_∞ to $nk_{\mathrm{B}}T$. Meanwhile, the expression for the viscosity of a hard sphere gas is [122]

$$\eta = \frac{1}{3}\rho v_{\mathrm{th}} l_{\mathrm{FP}}, \tag{7.2.3}$$

where v_{th} is the thermal velocity. Noting that $l_{\mathrm{FP}} = v_{\mathrm{th}}\tau_{\mathrm{c}}$, with τ_{c} the mean time between collisions, and $\frac{1}{2}\rho v_{\mathrm{th}}^2 = \frac{3Nk_{\mathrm{B}}T}{2V}$, we retrieve the result:

$$\frac{\eta}{G_\infty} = \tau_{\mathrm{c}}(= \tau_{\mathrm{M}}). \tag{7.2.4}$$

In other words, the viscoelastic relaxation time represents the microscopic "event" frequencies of both the liquidlike and gaslike fluids far from FL *on either side.* This

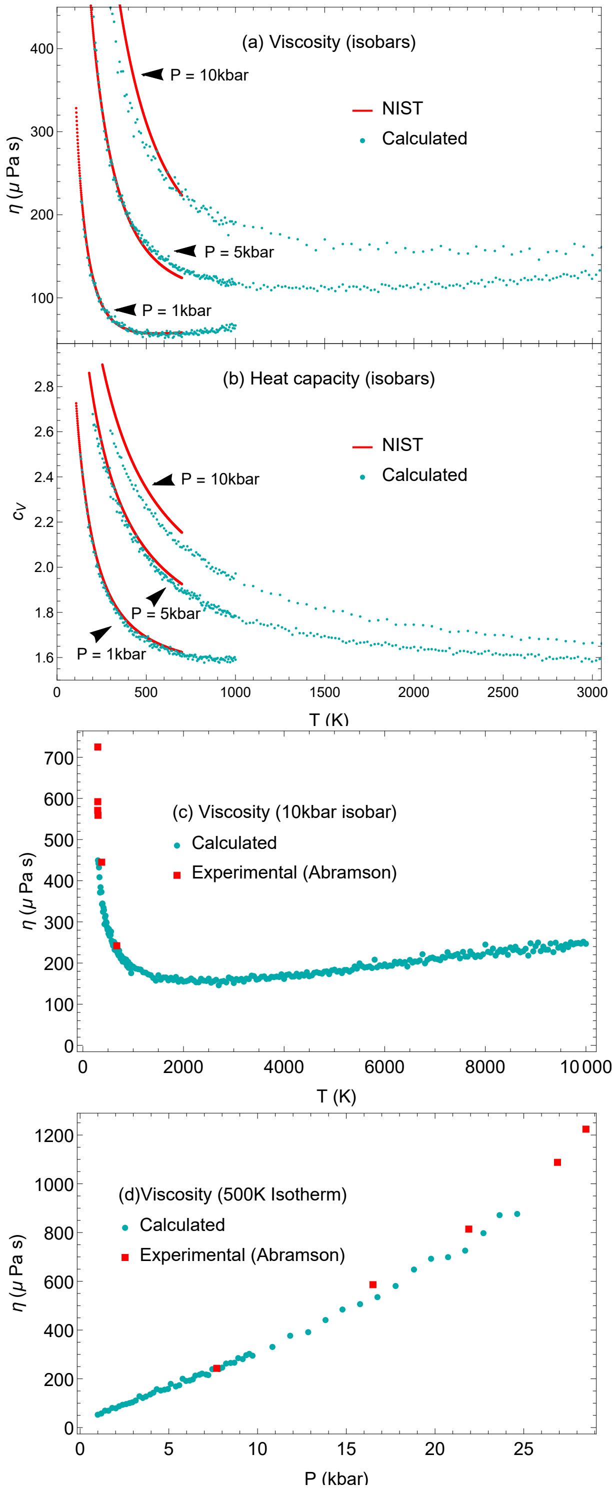

Figure 7.1: Comparison of (a) viscosities η and (b) isochoric specifc heat capacities c_V ($k_B = 1$) calculated from simulated trajectories with experimental data from NIST [97]; comparison of viscosities η calculated from simulated trajectories along the (c) 10 kbar isobar and (d) 500 K isotherm, with experimental data from Abramson [125].

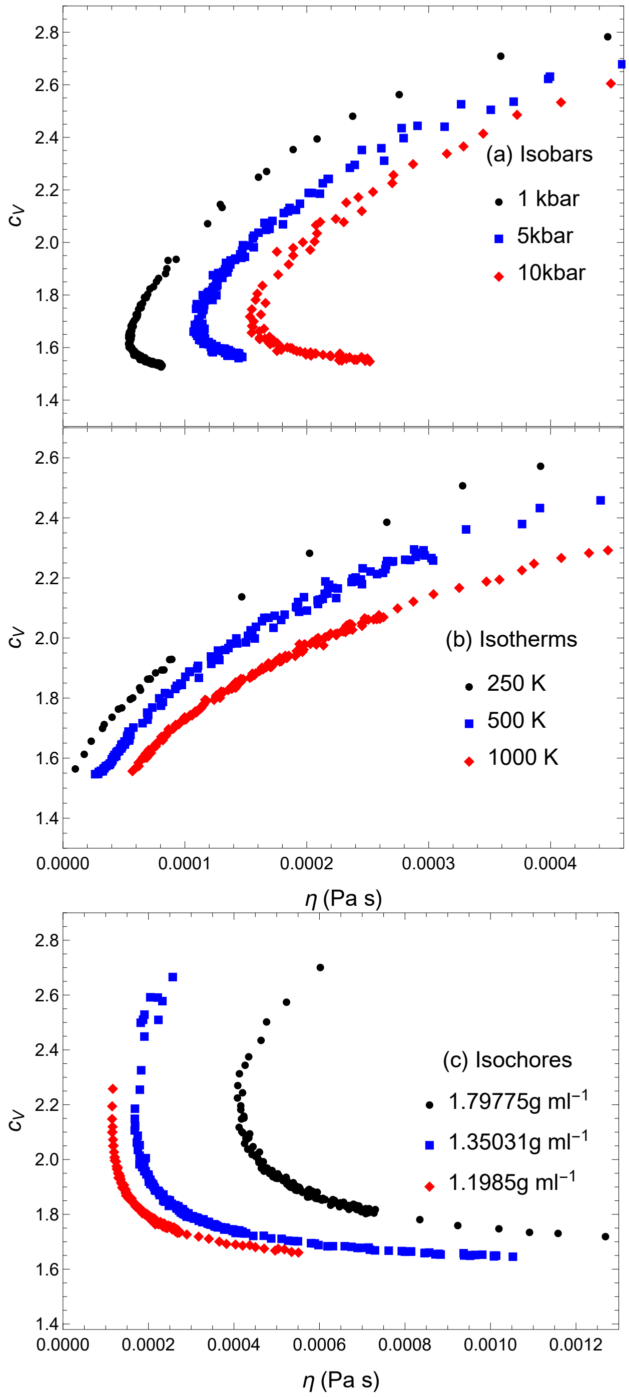

Figure 7.2: Specific heat c_v ($k_\mathrm{B} = 1$) as a function of viscosity η, calculated along three (a) isobars; (b) isotherms; (c) isochores.

makes it a natural choice of dynamical parameter close to the FL, because although the diffusion and collision times do not carry much physical meaning in such states, τ_{M} is always well-defined. The minima therefore represent a crossover from a liquidlike relaxation time commanded by diffusion and oscillation events [130] to a gaslike relaxation time commanded by collisions [41]. This same crossover takes place along isochores, but manifests differently in τ_{M} because τ_{M} can only decrease with temperature on an isochore. Indeed, $\tau = \frac{L}{v_{\mathrm{th}}}$ in the gaslike regime, where L and v_{th} are the particle mean-free path and thermal velocity in the gaslike state and $L = \frac{1}{n\sigma}$, where σ is the particle cross-section area. Hence τ_{M} decreases with temperature at constant n mostly because $v_{\mathrm{th}} \propto \sqrt{T}$ increases (σ decreases with temperature weakly). We note that the minima of both η and τ_{M} depend on the path taken on the phase diagram and path parameters.

We now investigate the relationship between dynamics and thermodynamics by plotting c_V as a function of τ_{M} along these nine paths in Fig. 7.4. Along isobars and isotherms, $c_V(\tau_{\mathrm{M}})$ has clear turning points corresponding to the minima in τ_{M}. This turning point occurs close to $c_V = 2k_{\mathrm{B}}$, such that the crossover in c_V from liquidlike to gaslike corresponds to the dynamical transition in τ_{M}. Along isochores, the situation is again more subtle. However, since the ideal gas limit as $T \to \infty$ corresponds to both $c_V \to 3/2$ and $\tau_{\mathrm{M}} \to 0$, the function $c_V(\tau_{\mathrm{M}})$ in its gaslike regime must approach 3/2 as $\tau_{\mathrm{M}} \to 0$. Inspection of Fig. 7.4c reveals that this is indeed the case, and that $c_V(\tau_{\mathrm{M}})$ settles into this limiting behaviour again close to $c_V = 2k_{\mathrm{B}}$.

Notably, Figures 7.2 and 7.4 show the significant path dependence of c_V on η and τ_{M}: c_V depends differently on these parameters along isochoric, isobaric and isothermic paths as well as different conditions for each path. Moreover, switching the dependence of c_V from η to the related τ_{M} completely changes the shape of the curves.

We now come to the pinnacle of these analyses. Recall our discussion of gapped momentum states in liquids in Chapter 2. We recall the gapped wavevector, k_{g} from Eq. 2.2.15:

$$k_{\mathrm{g}} = \frac{1}{2c^{\mathrm{T}}\tau_{\mathrm{M}}}, \tag{2.2.15}$$

which was the solution to Eq. 2.2.12:

$$(c^{\mathrm{T}})^2\boldsymbol{\nabla}^2\mathbf{v}^{\mathrm{T}} = \frac{1}{\tau_{\mathrm{M}}}\frac{\partial \mathbf{v}^{\mathrm{T}}}{\partial t} + \frac{\partial^2 \mathbf{v}^{\mathrm{T}}}{\partial t^2}. \tag{2.2.12}$$

It follows from the discussion in Section 2.2 and Eq. 2.2.15 in particular that the solution to the Maxwell-Frenkel viscoelasticity importantly depends on a certain parameter with dimensions of length. We call this parameter the dynamical fluid elasticity length $\lambda_{\mathrm{d}} = c^{\mathrm{T}}\tau_{\mathrm{M}}$. The physical meaning of this length is that it sets the range of propagation of solid-like transverse waves in the liquid because τ_{M} is the time during which the shear stress is relaxed. Hence, c_V should uniquely depend on λ_{d} because (a) λ_{d} governs the propagation of transverse modes and (b) each mode carries the energy $k_{\mathrm{B}}T$ (in harmonic classical case). Moreover, this dependence is predicted to be unique and path-independent, in contrast to the dependence of c_V on η or τ_{M} plotted earlier. Therefore, we plot $c_V(\lambda_{\mathrm{d}})$ in Fig. 7.5, and will use λ_{d} in our subsequent analysis

The result of this master plot in Fig. 7.5 is striking. Despite the clear difference among paths of the same and different type seen in Figs. 7.2, 7.3 and 7.4, the functions

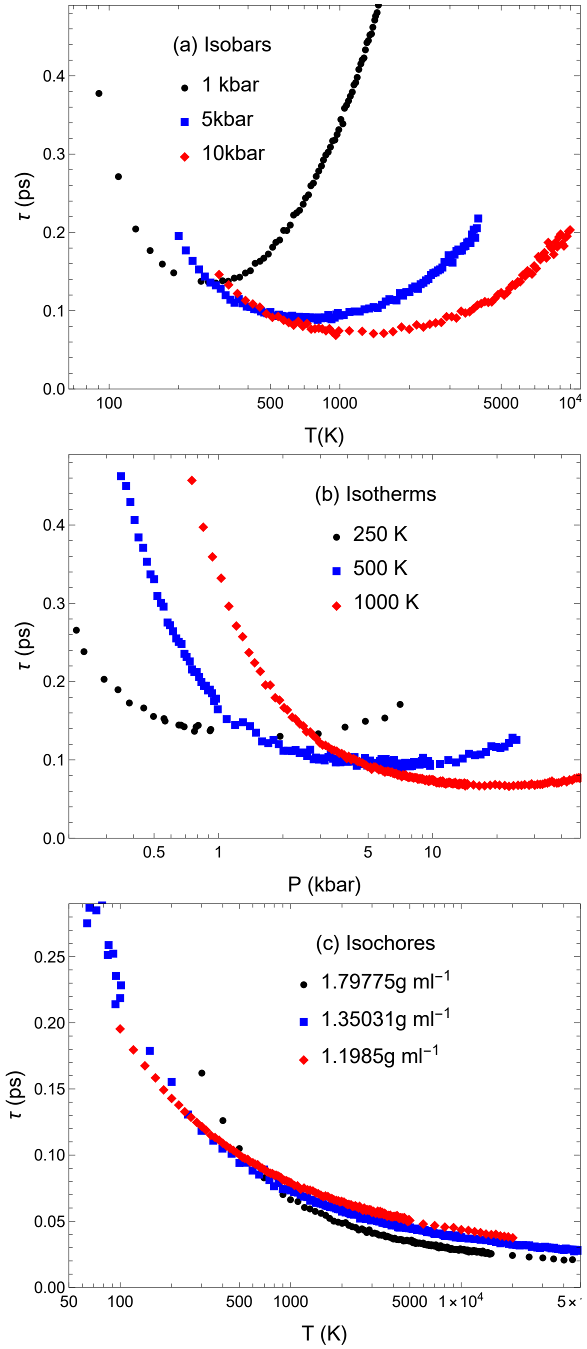

Figure 7.3: Liquid relaxation time τ of molecular dynamics trajectories along three (a) isobars; (b) isotherms; (c) isochores.

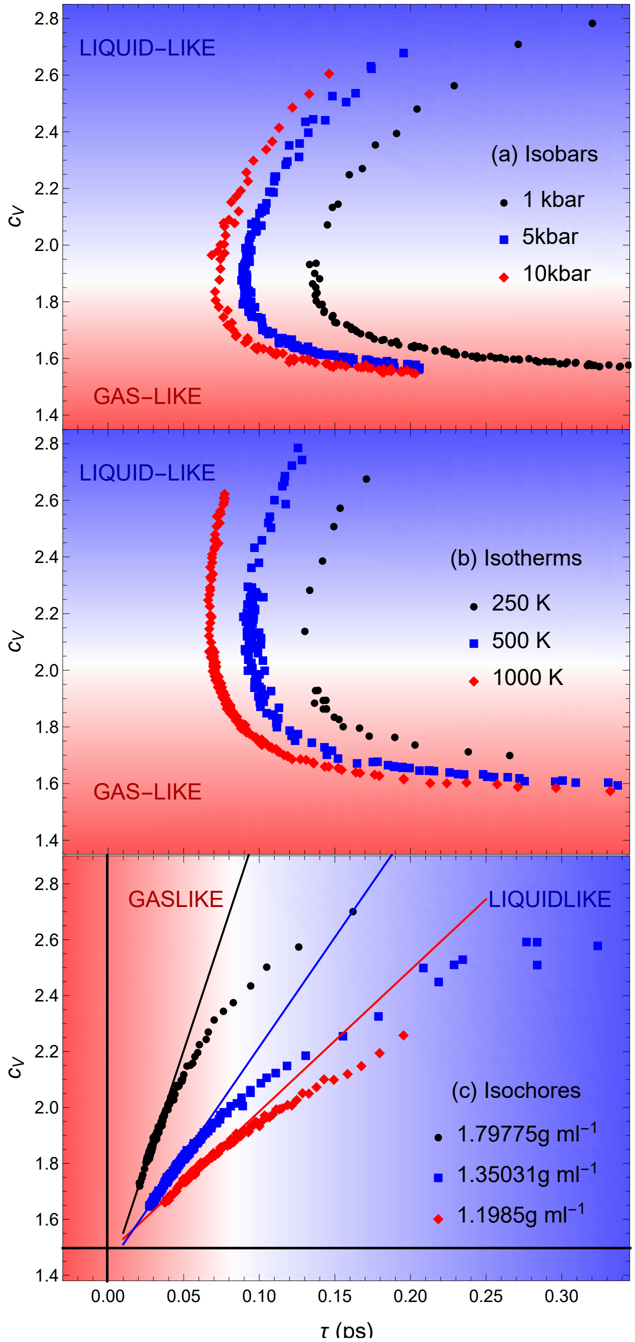

Figure 7.4: Specific heat c_V ($k_\mathrm{B} = 1$) as a function of relaxation time τ, calculated along three (a) isobars ; (b) isotherms; (c) isochores. The solid lines in (c) represent the approach of c_V and τ to their limiting ideal-gas value $c_V = 3/2$ at large temperature and are meant as guides for the eye.

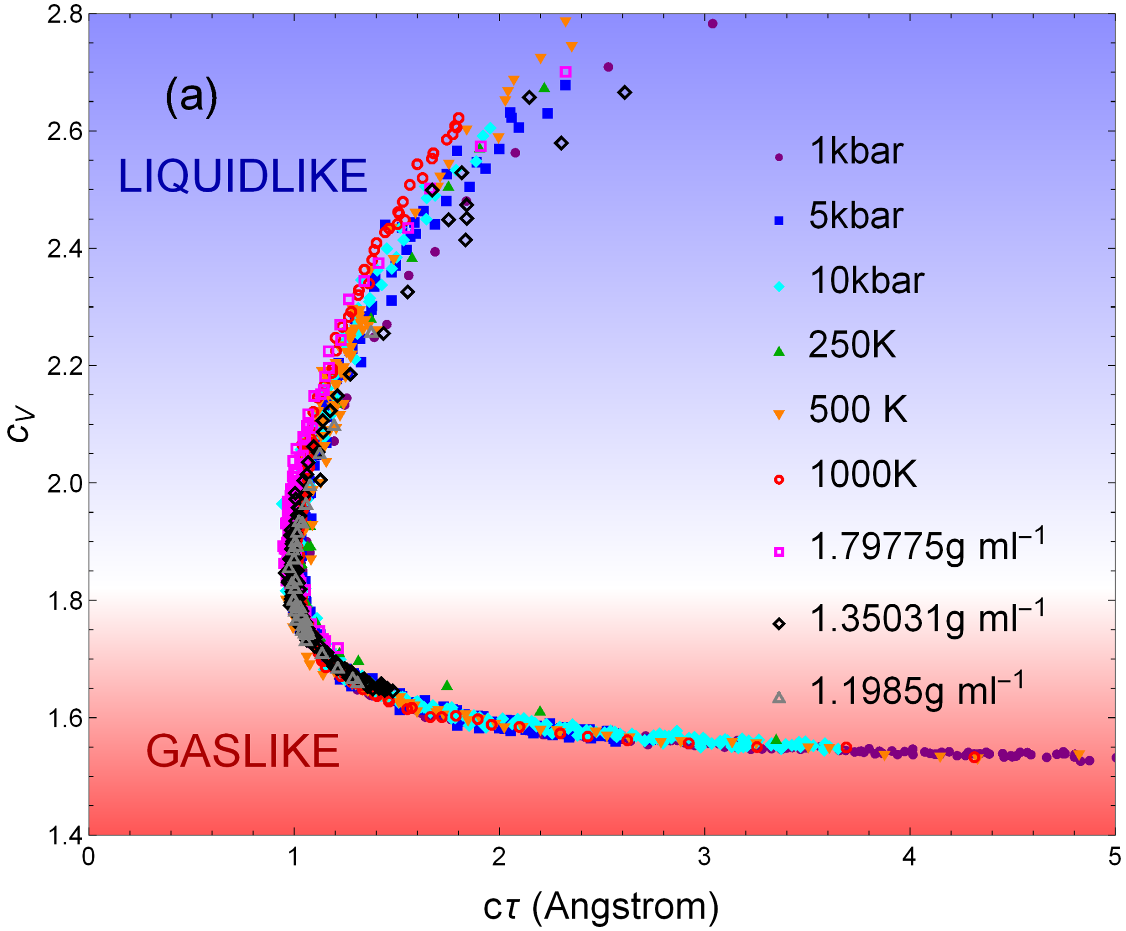

Figure 7.5: Simulated c_V ($k_\mathrm{B} = 1$) of argon as a function of the dynamical length, $\lambda_\mathrm{d} = c\tau$ across 9 paths spanning the supercritical state up to 330 T_c and 8000 P_c. All these paths collapse onto a single curve and undergo a unified dynamic-thermodynamic transition at the path-independent point $c_V = 1.88$ and $\lambda_\mathrm{d} = 1$ Å

$c_V(c^{\mathrm{T}}\tau_{\mathrm{M}})$ *along all deeply supercritical paths* converge into the same "c"-shaped curve in Fig. 7.5. The liquidlike parts of the paths follow a similar shape before converging into exactly the same curve. We can consider the $c_V(\lambda_{\mathrm{d}})$ curves to belong to a single family, the loci of which converge at the inversion point of $c_V \approx 1.88k_{\mathrm{B}}$. From here on out, I will call the loci, and the shape they trace out, the *main sequence.*

The values of $c_V \approx 2k_{\mathrm{B}}$ and $\lambda_{\mathrm{d}} \approx 1$ Å at the inversion point in Fig. 7.5 are physically significant. As previously explained, the value of $c_V = 2k_{\mathrm{B}}$ corresponds to a complete lack of propagating transverse modes from the fluid's phonon spectrum, with atoms effectively interacting only longitudinally. In Frenkel's theory $c_V = 2k_{\mathrm{B}}$ defines the upper limit (in temperature), occurring well above the melting point where τ_{M} becomes comparable to Debye vibration period. At this point, k_{g} in Eq. 2.2.15 becomes close to the largest wavevector set by the interatomic separation in the system (UV cutoff), and all transverse waves disappear from the spectrum, resulting in $c_V = 2$.

Anharmonicity can change this $c_V = 2k_{\mathrm{B}}$ result by a relatively small amount [41], and the disappearance of transverse modes corresponds in anharmonic systems to $c_V = 2k_{\mathrm{B}}$ only approximately. We also note that similarly to solids, plane waves decay in liquids. The decay mechanisms in solids include anharmonicity, defects and structural disorder present in, for example, glasses. Despite this decay, high-temperature specific heat in solids is governed by phonons. In liquids, the additional decay mechanism is related to atomic jumps [41]. Nevertheless, the propagation length of high-frequency excitations in liquids and supercritical fluids is on the order of nanometers, as evidenced by experiments and modelling [131, 132, 133, 103]. This is similar to room-temperature solids where the lifetime of high-frequency phonons is on the order of picoseconds and the propagation range is on the order of nanometers [134] and where disorder and/or defects reduce these values further. This is also similar to glasses which are structurally similar to liquids [135]. Therefore, phonon excitations govern the specific heat in liquids and supercritical fluids to the same extent they do in solids.

The significance of the propagation range λ_{d} reaching about 1 Å at the inversion point in Fig. 7.5 is that it corresponds to the shortest distance in the system (UV cutoff), the interatomic separation on the order of Angstroms in condensed matter phases. This distance is fixed by fundamental physical constants in the form of the Bohr radius which, incidentally, together with the Rydberg energy, sets the viscosity minimum [136]. The UV cutoff puts the upper limit for k-points for propagating waves in the system. Recall that k_{g} in 2.2.15 sets the range of transverse waves. When k_{g} becomes comparable to the largest, Debye, wavevector, all transverse modes disappear from the system spectrum. We have calculated the Debye wavevector $k_{\mathrm{D}} = (6\pi^2 n)^{\frac{1}{3}}$ [7], to be about 1.0 Å^{-1} at the inversion point. Equating it to $\frac{1}{2c^{\mathrm{T}}\tau_{\mathrm{M}}}$ in 2.2.15 gives $\lambda_{\mathrm{d}} = c^{\mathrm{T}}\tau_{\mathrm{M}} \approx 0.5$ Å. This is consistent with about 1 Å at the inversion point in Fig. 7.5, given the approximate nature of Debye model and that 2.2.15 applies to the linear part of the dispersion relation only but not to the range where $\omega(k)$ flattens off close to the zone boundary at $k = k_{\mathrm{D}}$.

In the gaslike state, the quantity $c^{\mathrm{T}}\tau_{\mathrm{M}}$ increases towards the ideal limit of $c_V = 3/2$ in Fig. 7.5. The collapse of all curves in the gaslike regime in Fig. 7.5a implies that $c\tau$ is the *only* parameter necessary to characterise the loss of these degrees of freedom in this regime.

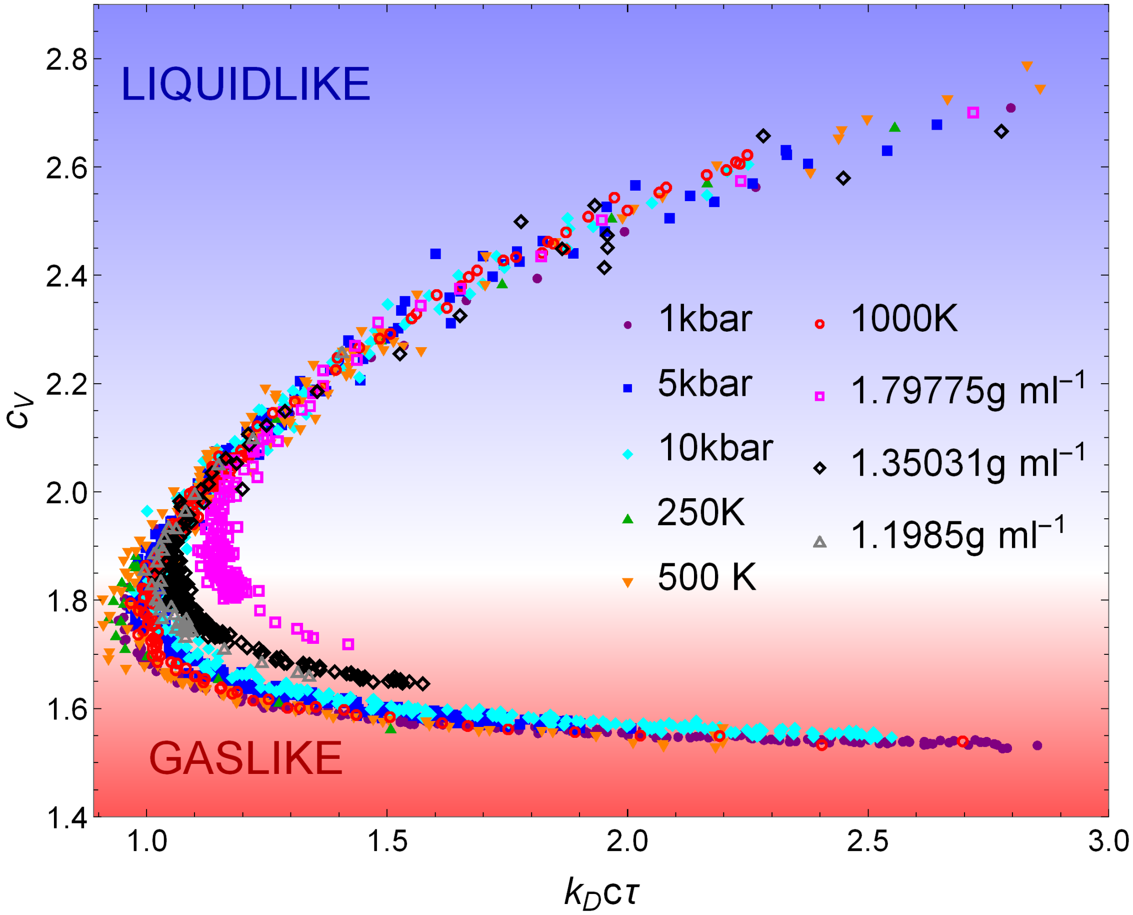

Figure 7.6: c_V as a function of $c^{\mathrm{T}}\tau_{\mathrm{M}}k_{\mathrm{D}}$ ($k_{\mathrm{B}}=1$), where the curves similarly converge in the liquidlike state at the path-independent point close to $c_V=2$.

An alternative way to collapse the data from different paths is informed by the phonon theory of liquid thermodynamics. As we saw, the liquid energy at low temperatures, where transverse waves exist below the Frenkel line, depends on the ratio of k_{g} in 2.2.15 and the Debye wavector k_{D}: $\frac{k_{\mathrm{g}}}{k_{\mathrm{D}}}$ [41, 103, 137] (or, alternatively, on $\frac{\omega^{\mathrm{F}}}{\omega_{\mathrm{D}}}$ for propagating waves [41], where $\omega_{\mathrm{F}}=\frac{1}{\tau_{\mathrm{M}}}$ and ω_{D} is Debye frequency). However, this disappearance of transverse modes can only proceed up to the largest k-point, k_{D}, set by the UV cutoff in the system as discussed earlier. As a result, $\frac{k_{\mathrm{g}}}{k_{\mathrm{D}}}$ enters the equation for the liquid energy. We plot c_V as a function of dimensionless product $c^{\mathrm{T}}\tau_{\mathrm{M}}k_{\mathrm{D}}$ in Fig. 7.6. We observe that the curves from all paths collapse in the region of large c_V down to about $c_V=2$, showing that c_V below the Frenkel line depends on the product $c^{\mathrm{T}}\tau_{\mathrm{M}}\tau k_{\mathrm{D}}$ only, as predicted theoretically. This is followed by the divergence of c_V below $c_V=2$ in the gaslike state along different paths, presumably because the solid-like concepts underlying k_{D} become progressively less relevant in the gaslike state at high temperature.

The key result of this work is visible in both scaling graphs in Figs. 7.5 and 7.6: the data collapse in either large or small-value range of c_V; the curves diverge from each other in the other range; and this divergence takes place near the key value $c_V=2k_{\mathrm{B}}$. We have identified two parameters, λ_d and $\lambda_\mathrm{d} k_\mathrm{D}$, which fully characterise the heat capacity of argon.

7.3 Molecular Dynamics Simulations - Carbon Dioxide

Argon is all well and good, however it is almost as simple a system as we can simulate, with only the hard sphere and soft sphere systems being any simpler. The single interaction type between loose atoms is very helpful as a conceptual tool, however for practical and conceptual reasons we ought to see what happens to the "c"-transition in other types of fluid. The first system I considered is nitrogen, N_2, modelled as a rigid body with two Lennard-jones sites. In this case, the formula for heat capacity must be modified to account for the change to the equipartition, from Eq. 3.3.12 to:

$$c_V = \frac{5}{2} k_\mathrm{B} \left(1 - \frac{\langle K^2 \rangle_{NVE} - \langle K \rangle^2_{NVE}}{\frac{5}{2} N k_\mathrm{B}^2 \langle T \rangle^2_{NVE}} \right)^{-1}, \tag{7.3.1}$$

with K again the kinetic energy. Changing from a monoatomic to a rigid diatomic Lennard-Jones system is a small shift, but there are noteworthy changes to the dynamics. The viscosity will certainly be somewhat sensitive to the extra dimension afforded to the molecules and the addition of rotational dynamics. The "c"-transition, however, still holds. I would place the graphs here, but the next system is also a rigid linear molecule but its energetics are far more complicated, such that nitrogen offers nothing new except encouragement. This next system is a return to carbon dioxide.

As already stated, carbon dioxide is one of the most used supercritical fluids, enjoying a variety of industrial and environmental applications. It's also very accessible, with a critical temperature of around 300 K and a critical pressure of "only" around 75 bar. Theoretically, it importantly differs from nitrogen because it contains two different elements and its bonds are not entirely covalent. Oxygen's electronegativity gives carbon dioxide a quadrupole moment and therefore electrostatic interactions must be included in our simulations. Furthermore we have to contend with three different sorts of Van der Waals interactions between the different element pairs. The energetics of carbon dioxide are therefore considerably more complicated, and there is plenty of room for the viscosity, speed of sound, and heat capacity to diverge from the very tidy interrelation we found in argon and nitrogen.

The crystal structure of carbon dioxide naturally implicates some significant order with respect to orientation. Setting up an initial configuration in this structure, knowing full well that I shall only go on to melt it, struck me as a tad gratuitous, so initial configurations of 512 carbon dioxide molecules were produced in an unphysical simple cubic structure. The exact same equilibration procedure as used in argon is used here. Analysis was performed in the same way, save for the modification in c_V seen in Eq. 7.3.1. DL_POLY automatically calculates the $k \to 0$ limit stress tensor according to the different types of forces included in the setup, so no modification on my part was necessary. We simply note that in the gaslike end of the "c"-transition, c_V (this time measured per molecule) must approach $\frac{5k_{\mathrm{B}}}{2}$ rather than $\frac{3k_{\mathrm{B}}}{2}$. The inversion point of the “c”-transition is more difficult to predict, as carbon dioxide’s more complicated inner structure allows it to evade a simple modal decomposition. If there is no significant orientational collective dynamics at the FL, however, which seems a reasonable assumption, then we would expect the inversion point to below slightly below $3k_{\mathrm{B}}$, equivalent to argon and as it does in nitrogen.

We needn’t indulge in the story of the previous section, we know our favourite parameter and we know what to do with it. What is worth mentioning, however, is the potential for carbon dioxide I’m using, the same as in Section 3, models van der Waals forces using the Buckingham equation, Eq. 3.2.5. As stated, the behaviour of the Buckingham potential at small distances is unphysical, and its usage comes with the proviso that an atom never be likely to cross the maximum caused by the competing attractive and repulsive terms. Should we choose an isochore as a path on the phase diagram and try to follow it up to a gaslike c_V near $\frac{5k_{\mathrm{B}}}{2}$, this unphysical attraction becomes a problem. This is because a fixed density requires enormous temperatures in order for atoms to surpass their attractive terms and acquire nearly unbound motion. Unfortunately very high kinetic energy at fixed extreme compression is exactly what will cause an atom to overcome the Buckingham potential’s maximum. For this reason, no supercritical isochore will be extendable by our simulations into the gaslike regime. This isn’t a problem, however, since the other paths I have selected still sample a wide region of the phase diagram and adequately demonstrate path independence. The paths are three isobars: 2 kbar, 5 kbar, 10 kbar; and two isotherms: 1000 K and 2000 K.

Behold the “c”-transition in Fig. 7.7, just as stark in carbon dioxide as it was in argon. As expected, the transition occurs at around $2.9k_{\mathrm{B}}$, implying that the thermodynamic evolution in the gaslike state beyond the inversion point is defined, as in the simple monoatomic theoretical case, by the loss of short-wavelength intermolecular collective longitudinal modes. The shape of the curves in Figs. 7.5 and 7.7 are very similar, surprisingly similar, in fact. The inversion point occurs again at $\lambda_{\mathrm{d}} = 1$ Å, and the curves coincide not only in the gaslike states, but also in the liquidlike states, whereas there is moderate divergence in argon. Why carbon dioxide exhibits an even neater transition than argon is a mystery to me.

The critical point of carbon dioxide is 303 K, 73.8 bar. The critical point of argon is 151 K, 48.6 bar. This means that near critical effects are much less easily avoided in carbon dioxide, and indeed I ran into them without specifically looking for them. The “c”-transition operates in a huge range of the supercritical state, but it is only the deep supercritical state which hosts it. Near the critical point, the curves fail to collapse onto the main sequence curve in the gaslike state, as can be seen in argon and carbon dioxide in Fig. 7.8. The near-critical 500 K isotherm of carbon dioxide and near-critical 10 bar isobar of argon both deviate from the main sequence roughly when they pass near the critical isochore, returning to the main sequence curve in the deeply liquidlike and gaslike states along the paths far from the critical point. This demonstrates the uniqueness and importance of near-critical state and the near critical anomalies.

Moreover, a subcritical isobar, at 10 bar, was simulated in argon and underwent “c”-transition analysis, the results of which are plotted in Fig. 7.8b. Naturally a subcritical path will contain a discontinuity in the heat capacity and dynamical length, and this

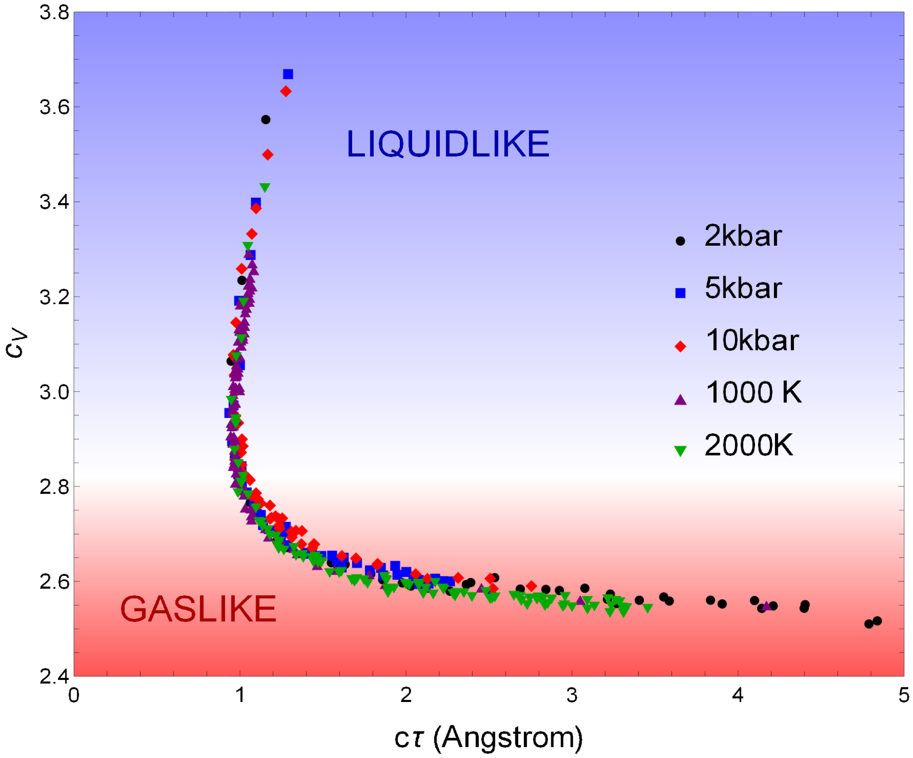

Figure 7.7: Simulated c_V ($k_\mathrm{B} = 1$) of carbon dioxide as a function of the dynamical length, $\lambda_\mathrm{d} = c\tau$ across 5 paths spanning the supercritical state up to 33 T_c and 520 P_c. All these paths collapse onto a single curve and undergo a unified dynamic-thermodynamic transition at the path-independent point $c_V = 2.9$ and $\lambda_\mathrm{d} = 1$Å

can be seen in the figure. However, on either side of this continuity the curves fall onto the main sequence. In the gaseous (not gaslike!) state the curve coincides exactly with the other paths, and in the liquid state it falls into the locus of similar curves, just like the other liquidlike paths. This is a rather profound discovery, as it extends the "c"-transition into the subcritical regimes - liquids and gases. Recall the vast range of supercritical states which conform to both sides of the "c"-transition - this dynamical correspondence is shared by liquids and gases below the critical point. One starts to wonder what essential differences exist between liquids and liquidlike supercritical fluids, and likewise between gases and gaslike supercritical fluids. We'll return to this.

7.4 Discussion

This transition, the "c"-transition as we call it, was not an expected consequence of the FL. The expression for C_V in Eq. 2.2.8 is only very approximate, especially regarding its volume dependence which arises through k_{D} and the partial derivative $\left(\frac{\partial k_{\mathrm{g}}}{\partial T}\right)_V$. It is far from obvious that across many different phase diagram paths, differing by orders of magnitude in temperature and pressure, the functions $c_V(\lambda_{\mathrm{d}})$ would all converge into a single point, at the point $c_V \approx 1.9k_{\mathrm{B}}$, and at the apex of a transition from liquidlike to gaslike behaviour. One could have predicted that a path-independent expression for c_V in the gaslike state would have been derivable from dynamical considerations, but the convergence of all curves at a single point exactly at the apex of the liquidlike to gaslike transition is a very striking discovery.

As mentioned earlier, the dynamical VAF criterion of the Frenkel line corresponds to the disappearance of the oscillatory component of particle motion. In Fig. 7.9, we plot the line calculated using the VAF criterion in argon, together with the "c"-transition line determined by (P,T) at the inversion point where $c_V \approx 1.9$ in Fig. 7.5. We also plot the critical isochore for comparison. The Frenkel line from the VAF criterion and the inversion point are close and run parallel to each other. This serves as self-consistency check for our theory and implies that the inversion point can serve as a hallmark and a definition of the supercritical transition between the liquidlike and gaslike states at the FL. As mentioned earlier, the inversion point is unambiguously defined in Fig. 7.5 and does not depend on a theory such as that underlying the thermodynamic criterion $c_V = 2k_{\mathrm{B}}$ and the dynamical VAF criterion.

Let me reiterate that near the critical point, the dynamical and thermodynamical properties are strongly affected by near-critical anomalies [22, 44], and the function $c_V(\lambda_{\mathrm{d}})$ is affected as a result. The function $c_V(\lambda_{\mathrm{d}})$ calculated along near-critical paths does not collapse onto the inversion point. On the other hand, our main sequence curve in Figs. 7.5 and 7.7 is deeply supercritical (and subcritical) and is therefore free of the near-critical anomalies. The deeply supercritical state was simultaneously very mysterious, on account of underexploration, and little considered, so the operation of the "c"-transition in the deep supercritical state and not near the critical point is an unexpected discovery. The critical point is often accompanied by a rather famous example: one can continuously transform a liquid into a gas by going around the critical point. Of course if one strays close to the critical point in such a venture, while no boiling will occur, the transformation

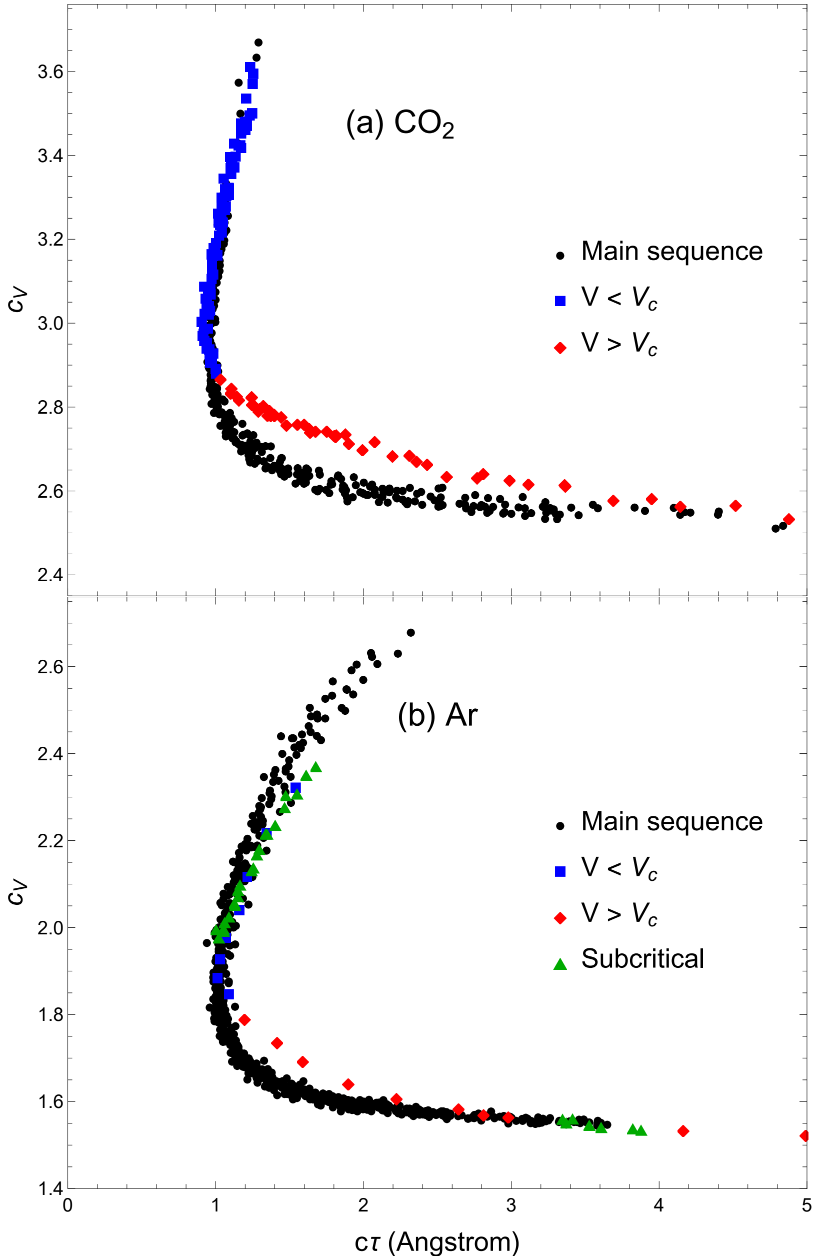

Figure 7.8: (a): Comparison of a near critical isotherm (500 K) in carbon dioxide to the main sequence "c"-transition curve from deeply supercritical state points. (b) Comparison of a near critical isobar and a subcritical isobar in argon to the main sequence. In both figures, the near-critical paths are split according to whether volume is above or below the volume of the critical isochore, V_c.

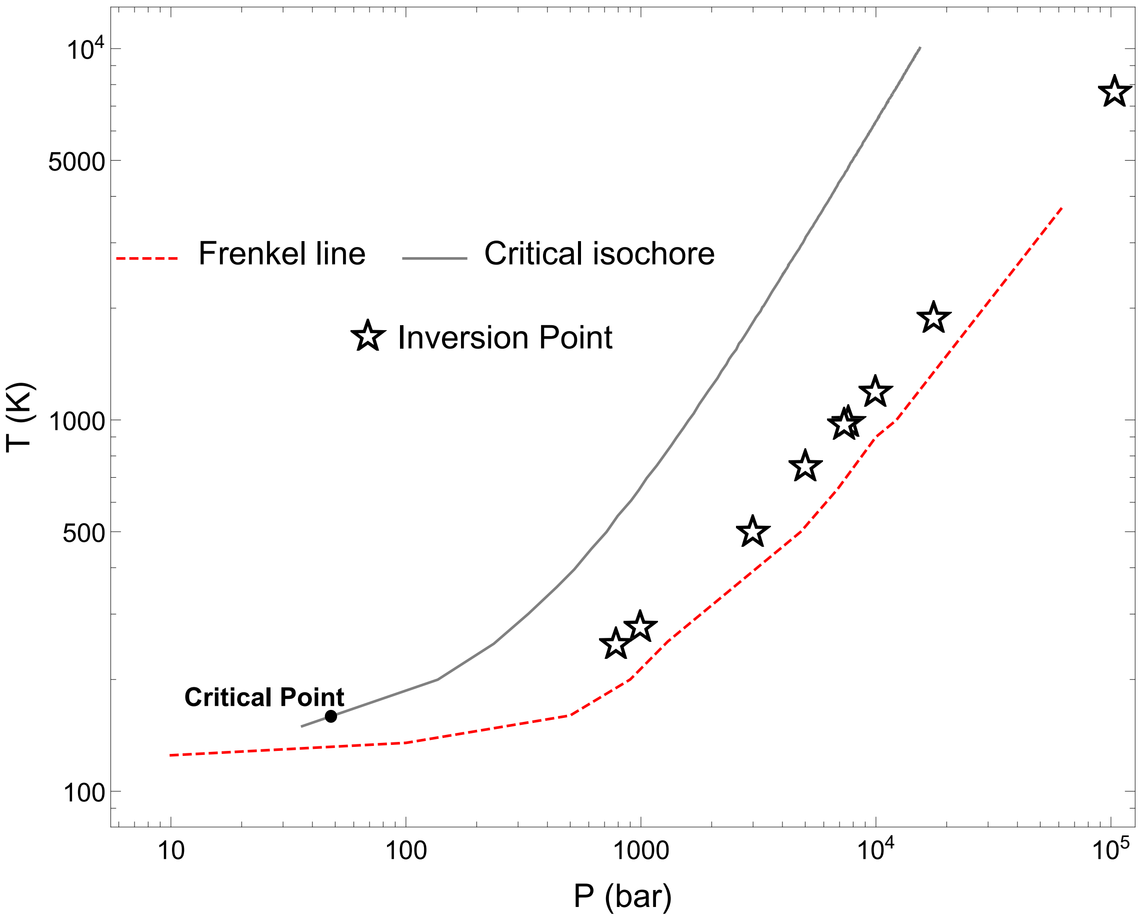

Figure 7.9: Phase diagram of argon showing the inversion points of the "c"-transition corresponding to $c_V \approx 1.9k_\mathrm{B}$ in Fig. 7.5, the Frenkel line determined by the VAF criterion [23], the critical point, and the critical isochore.

will nonetheless contain interesting anomalies. If, however, the critical point is avoided and a deeply supercritical path is chosen, what one will effectively do is traverse the entirety of the “c”-curve, from liquid to liquidlike to gaslike to gas. The near critical state, and the boiling line itself, are the anomalous parts of the phase diagram. The subcritical states and deeply supercritical states, at least in the sense of the “c”-transition, are one and the same.

There have been a great many proposals of methods to separate the supercritical state into liquidlike and gaslike regions recently. The Widom line [22], as mentioned, makes use of the near critical anomalies, effectively continuations of the boiling line itself, as they extend into the supercritical state. The Frenkel line itself, of course, has several different definitions including dynamic, thermodynamica, and spectral [138]. Another recent proposal [139] defined a dynamical degree of “solidicity”, derived from the VAF, to separate rigid and nonrigid states. This was related to the FL, and provided an alternative definition. Indeed, as the authors say, the FL is more fundamental than a liquid and gaseous state, existing in soft-sphere systems without a boiling line or critical point, a property understood since the FL’s early days [23]. The FL as a concept is therefore inundated with different definitions, all of which roughly agree with each other, and all of which are based on fundamental theoretical considerations with origins in our expectations of rigid and nonrigid states. The “c”-transition, however, is empirical - it defines a transition in and of itself, without needing to discuss expectations. There are two regimes in the supercritical state, one where the function $c_V(\lambda_\mathrm{d})$ falls on the universal curve at $c_V \lessapprox 1.9k_\mathrm{B}$, and one where the function $c_V(\lambda_\mathrm{d})$ converges upon the universal point, for any path, at $c_V \approx 1.9k_\mathrm{B}$. As can be seen in Fig. 7.9, the “c”-transition is closely traced by the VAF criterion of the FL, which confirms its origins. The discovery of the “c”-transition is a vindicating event for Frenkel theory, because I discovered it having been guided by this theory and nothing else. Equally, one can take the “c”-transition as the more fundamental phenomenon, since it’s unambiguous, and the FL and its accompanying theories to be a comprehensive explanation of this transition. There is much still to learn about the “c”-transition, and we must consider it as a distinct entity and not only view it by the grace of the FL, as there is no guarantee that the FL can provide us with all the answers.

The collapse of all curves up to the key value of about $c_V = 2k_\mathrm{B}$ and divergence of curves along different paths beyond this value has two further implications. First, it suggests that the inversion point $c_V = 2k_\mathrm{B}$ is a special point on the phase diagram. Second, if a thermodynamic property has a wide crossover, the behavior of different properties strongly depends on the path taken on the phase diagram. On the other hand, the observed collapse of all paths at the special inversion point close to $c_V = 2k_\mathrm{B}$ and $\lambda_d = 1$ Å indicates either a sharp crossover or a dynamically driven phase transition related to the “c”-transition between liquidlike and gaslike states. Within the uncertainty set by fluctuations in our simulations, we do not observe an anomaly of c_V in Fig. 7.1b at temperatures and pressures corresponding to the inversion point (our simulations put an upper boundary of about $0.05k_\mathrm{B}$ on the value of a possible anomaly of c_V). This does not exclude a weak thermodynamic phase transition, similar to a percolation transition, or a higher-order phase transition seen in higher derivatives of thermodynamic functions. The hunt for this phase transition is the topic of the next chapter.

In summary, we have discovered a universal, striking, and demonstrative inter-relation between dynamics and thermodynamics using the specific heat c_V and the dynamical parameter of the fluid elasticity length, $\lambda_{\mathrm{d}} = c^{\mathrm{T}}\tau_{\mathrm{M}}$. This connection provides a clear and path-independent transition between liquidlike and gaslike supercritical states, which we call a "c"-transition. Our "c"-shaped main sequence curve provides an unambiguous and path-independent criterion for the separation of liquidlike and gaslike states, calculated from accessible quantities in molecular dynamics simulations. The collapse onto this main sequence curve occurs in the supercritical state up to $T = 330T_c$ and $P = 8000P_c$, meaning the transition, and the distinct states it separates, exist over a far larger range of temperatures and pressures than the boiling line which separates subcritical liquids and gases. The collapse is indicative of either a sharp crossover or a new phase transition operating in the supercritical state.

Chapter 8

The Possibility of a Phase Transition

8.1 What is the nature of the "c"-transition?

The search for a phase transition at the FL, as I mentioned, was long frustrated by finding a suitable order parameter, with any obvious choices being too difficult to unambiguously define. The "c"-transition, if it does nothing else, makes it rather clear what the important parameter of the supercritical state is: $\lambda_{\mathrm{d}} = c^{\mathrm{T}}\tau_{\mathrm{M}}$. Or there may be a way in via $\lambda_{\mathrm{d}}k_{\mathrm{D}}$ due to the second manifestation of the "c"-transition seen in Fig. 7.6. The thermodynamic function c_V has a special relationship with λ_{d}, but the transition itself, along any one given path, is simply a stationary point. It's worth noting that no other obvious thermodynamic function shares a special relationship with λ_{d}. The "c"-transition is suggestive of a thermodynamic phase transition for the following reasons. The "c"-curves all converge into a single special point, $c_V \approx 1.9k_{\mathrm{B}}$, $\lambda_{\mathrm{d}} \approx 1$ Å for argon, which is path-independent, depending, rather, only on the constitution of the fluid. Therefore the fluid, as it arrives at this inversion point, approaches a sort of corresponding state where certain aspects of the dynamics and thermodynamics are identical, no matter how (on which path) this inversion point is approached. Furthermore, the curves on the gaslike side of the transition are all identical, such that the corresponding states which the inversion point heralds are not transitory, but rather define the whole supercritical state on the gaslike side of the "c"-transition. This implies a profound change in dynamics. However in order to find a thermodynamic phase transition, or convince ourselves of its absence, we must turn back to parameters such as temperature to characterise our properties.

8.2 Precision Measurements of c_V from Molecular Dynamics Simulations

The precision achieved in c_V in the MD simulations of argon was about $0.05k_{\mathrm{B}}$, though this belies somewhat problematic behaviour. Properties like energy, VAFs, RDFs, *etc* are relatively straightforward to calculate, as they are calculated as time averages of trajectories. Viscosity has its own problems, as discussed. The heat capacity, calculated from Eq. 3.3.12 is not so simple - the quantity itself is an average, or rather a function of several averages. Such quantities are called *fluctuation properties*. Fluctuation properties have a very sensitive dependence on the trajectory used to calculate them, and one needs to make sure that the trajectory is sampling the desired ensemble.

In the case of the NVE ensemble, this means ensuring that the standard deviation of energy is negligible, which was already being done. Furthermore it means ensuring that each trajectory samples sufficiently many states that its mean temperature is tolerably close to the target temperature, which furthermore requires that the trajectories be properly equilibrated. Nonetheless a non-insensible trajectory-dependence will remain, and averaging over initial conditions, each of which must satisfy the above conditions, is required.

In the case of the simulations done for the “c”-transition, processing was less rigid. This is because viscosity was a much greater source of error than trajectory dependence of fluctuation properties. The average c_V calculated at each state point had a standard deviation of up to $0.05k_\mathrm{B}$, which precludes identification of an anomaly in c_V of around this size or smaller. This error came from two sources: insufficient temperature control and short trajectories. I'll address these in order, and how I fixed them. Throughout this section the advice I received from and discussions I had with Alin-Marin Elena and Vlad Sokhan were invaluable.

The temperature control is caused by relatively short and cavalier periods of equilibration. By no means unacceptable by typical MD standards, but when we have our eyes on a precision much better than that achieved in the previous chapter, we have to do better. The first thing we would have to do is discard our smallest system size of 500. Fluctuations will always be unacceptably large in such a system. 4000 atoms however should be enough. The problem with equilibration to a certain temperature in the NVE ensemble is a tricky business, as I hinted at in Chapter 3. Simply initialising the system with a Maxwell velocity distribution at the target temperature is not good enough because it is the energy we are holding constant. The mean temperature on that energy hypersurface is by no means guaranteed to match the instantaneous temperature of the initial configuration we seeded, though it will be somewhat close. Repeatedly reseeding the velocities is suboptimal because you are effectively restarting the trajectory in this case and will run into the problem that the initial configuration won't be any more likely to represent the temperature of the whole hypersurface.

The idea, then, is to let the trajectory “carry on” while also directing it towards the temperature we want, so we don't have to deal with the sudden shift in temperature when a reseeded NVE trajectory relaxes into its “main sequence” phase space. One way to do this is by rescaling velocities. If one has an NVE trajectory with mean temperature T_0, whose target temperature is T, we can take the ratio $\frac{T}{T_0}$. We then take the final configuration of the trajectory and scale each velocity by the square root of the above ratio, effectively scaling the temperature by the same ratio, then we have made an attempt at correcting the temperature without significantly disrupting the trajectory. Repeated applications of this will allow the mean temperature of the trajectory to be set arbitrarily close to the target temperature. This method very quickly allows one to set the temperature of a trajectory very precisely, but at a cost. Rescaling velocities in this way is, unsurprisingly, very unphysical because it affects every atom in the same way, which is not in any way how contact with a thermal bath works. The scaling removes more energy from high velocity atoms than low ones, and so the effect of repeated velocity rescaling is to drain energy from high frequency modes into low frequency modes [140], as described before. This effect, the "flying ice cube effect" is particularly troublesome for rescaling thermostats such as the Berendsen thermostat. We should, however, still be careful here as the repeated removal of energy disproportionately from high-frequency modes may deposit the system in a strange part of phase space, nominally at the target temperature, but not at all sampling the "main sequence" dynamics of the equilibrium energy hypersurface associated with the target temperature.

The alternative to this is then to change the system's energy in a physical way. One might ask why we don't just take the final configuration of a trajectory under NVT dynamics (using, say, the Langevin thermostat) and subject that to NVE dynamics. The problem with this is effectively the same problem as simply setting an initial velocity distribution at the target temperature. The trajectory may have had the right temperature in NVT, but taking a point on that trajectory and sending it down a new NVE trajectory does not come with a guarantee of maintaining the correct temperature. We can, however, get close, by carefully tuning the friction constant of the thermostat. If the coupling between the bath and the system is very weak, then the dynamics are no terribly far removed from NVE dynamics. If such a weakly-coupled NVT trajectory is then switched to NVE dynamics, not much has changed and the mean temperature should also not change much. This method is not as fast as velocity rescaling, but this penalty comes with increased confidence in our results. In what follows, both methods were used, to no significant difference in results. Both methods allowed temperature to be controlled to within 0.1% of the target. The spacing between neighbouring temperature points is much larger than this, so this precision is acceptable.

The second source of error was short trajectories. One million timesteps was enough to get the viscosity under enough control for its behaviour to be unambiguous. However in order to have faith in our measurement of c_V using Eq. 3.3.12, we need to be sure that our trajectory is long enough to be sampling enough of the hypersurface for it to be passably ergodic. As stated, fluctuation properties like c_V are very sensitively dependent on the trajectory from which they are calculated. Even with temperature control satisfactorily undertaken, a longer trajectory may nonetheless be necessary to be sure that enough of the "main sequence" of the hypersurface is sampled and that rare events do not mar the trajectory. Ascertaining what qualifies as "long enough" is simply a matter of making trajectories longer until the desired precision of c_V is achieved. In what follows, this meant NVE trajectories of four million timesteps. These trajectories were taken from a single long trajectory, split into twenty four-million-timestep sections from which statistics were gathered independently. This is preferable to a single 80-million-timestep trajectory for two reasons: the first is that adding more time steps to a single trajectory has diminishing returns on the convergence towards the "infinite time" average (equal to the microcanonical phase average). Convergence is faster if the trajectory is split up and then the subtrajectories are averaged, up to a point, so it's a matter of finding the optimum. The second reason is that splitting the trajectory up allows us to take a standard deviation of the c_V to be associated with each average, giving us a quantitative measure of the error. We can therefore reliably seek our precision goal and

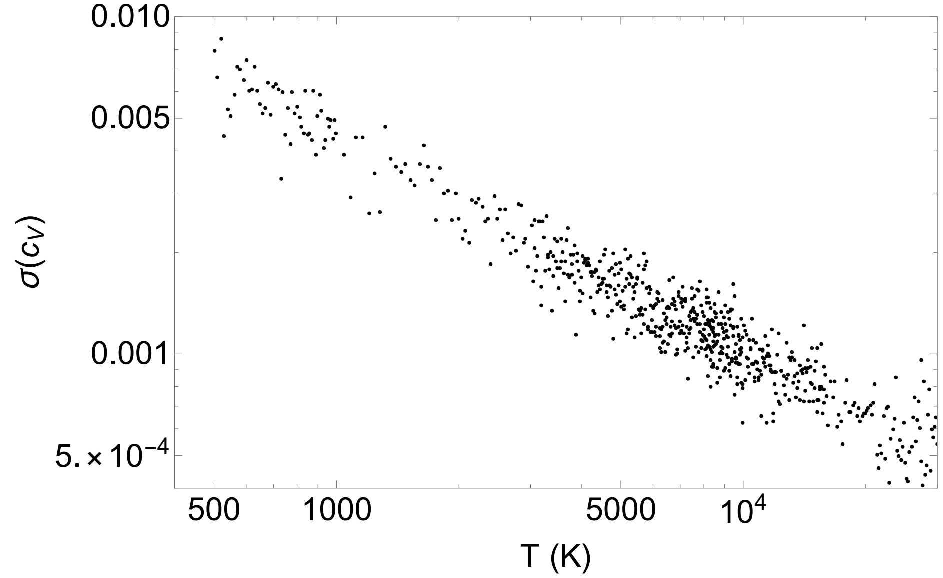

Figure 8.1: Standard deviation $\sigma(c_V)$ of the heat capacity calculated, at each temperature along the unit isochore in Lennard-Jones units (1.688 g/ml), using 20 4-million-timestep trajectories ($k_\mathrm{B} = 1$).

set an upper limit on any discontinuity in c_V on that basis.

The standard deviation on the mean of c_V calculated from the above method is plotted as a function of temperature in Fig. 8.1. The error in c_V, under the same number of trajectories of the same length, is seen to decrease with T as a power law. This is not altogether unexpected since the gaslike state is dynamically far simpler and c_V evolves much more slowly with temperature in this regime. These results were calculated along the unit isochore in Lennard-Jones units (corresponding to 1.688 g/ml, see Tab. 6.2), along which the inversion point of the "c"-transition is between 6000 and 7000 K. This means we achieve a precision of $\pm 0.002 k_\mathrm{B}$ in the region where we expect a possible phase transition to be operating on the basis of the "c"-transition. This will suffice for our first glance.

The full range of c_V along the unit isochore from $T = 500$ K to $T = 50000$ K is shown in Fig. 8.2. The greatest concentration of state points is in the region between $c_V = 2k_\mathrm{B}$ and $c_V = 1.8k_\mathrm{B}$, where as we saw the error is around or below $0.002k_\mathrm{B}$. One cannot appreciate the precision of the entire range at once, so a zoomed-in plot whose range is restricted to the area of most interested is presented in Fig. 8.3. In this region the uncertainty in c_V is between $0.002k_\mathrm{B}$ and $0.001k_\mathrm{B}$. The data here therefore present as a band whose width is twice the error, and we can see very clearly that this band presents no sort of discontinuity. Indeed, there are no close candidates either. Producing this plot took approaching a million hours of processor-time in total.

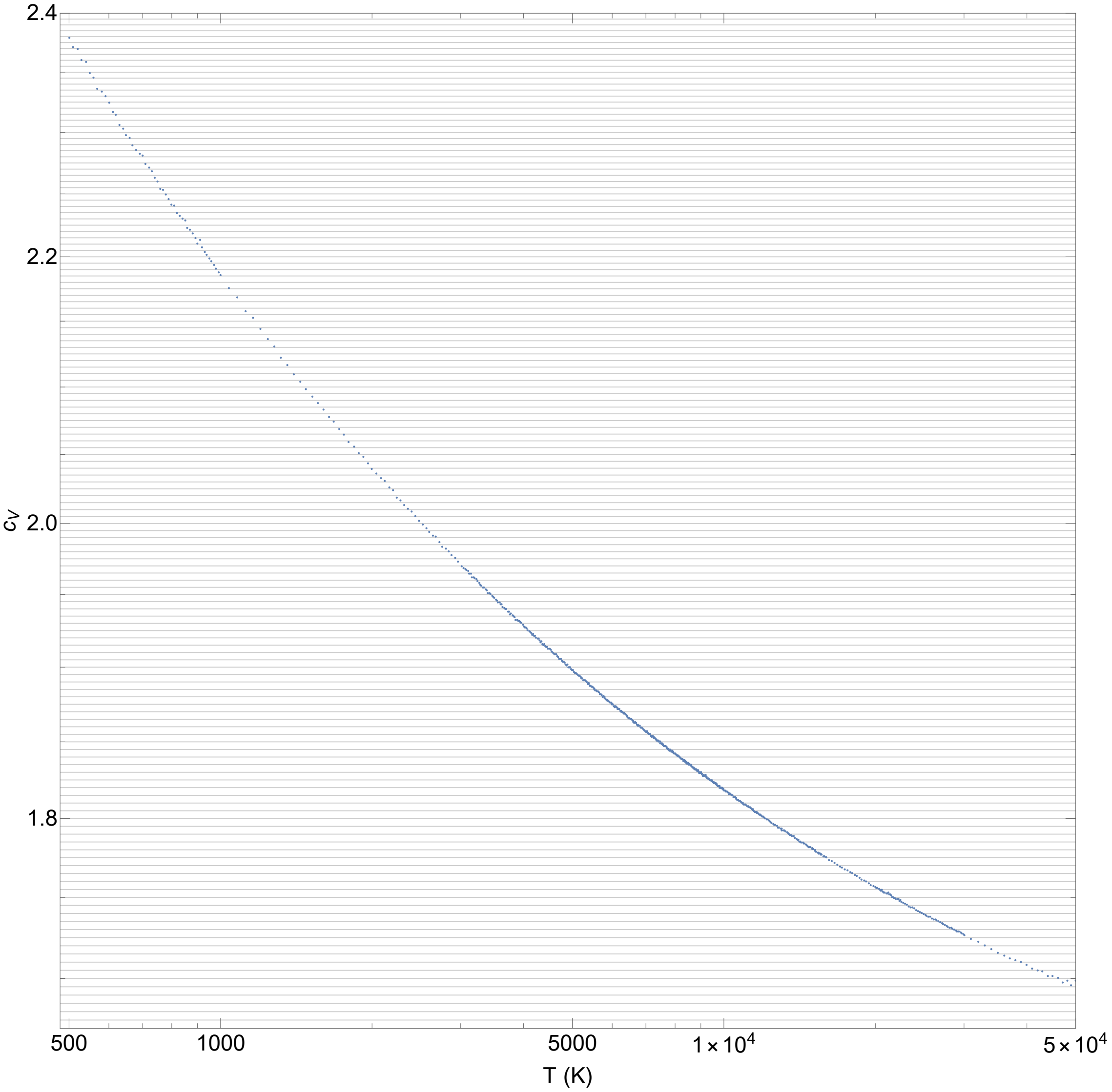

Figure 8.2: Heat capacity c_V calculated along the unit isochore in Lennard-Jones units, using 20 4-million-timestep trajectories ($k_\mathrm{B} = 1$). The gridlines are separated by $0.005k_\mathrm{B}$.

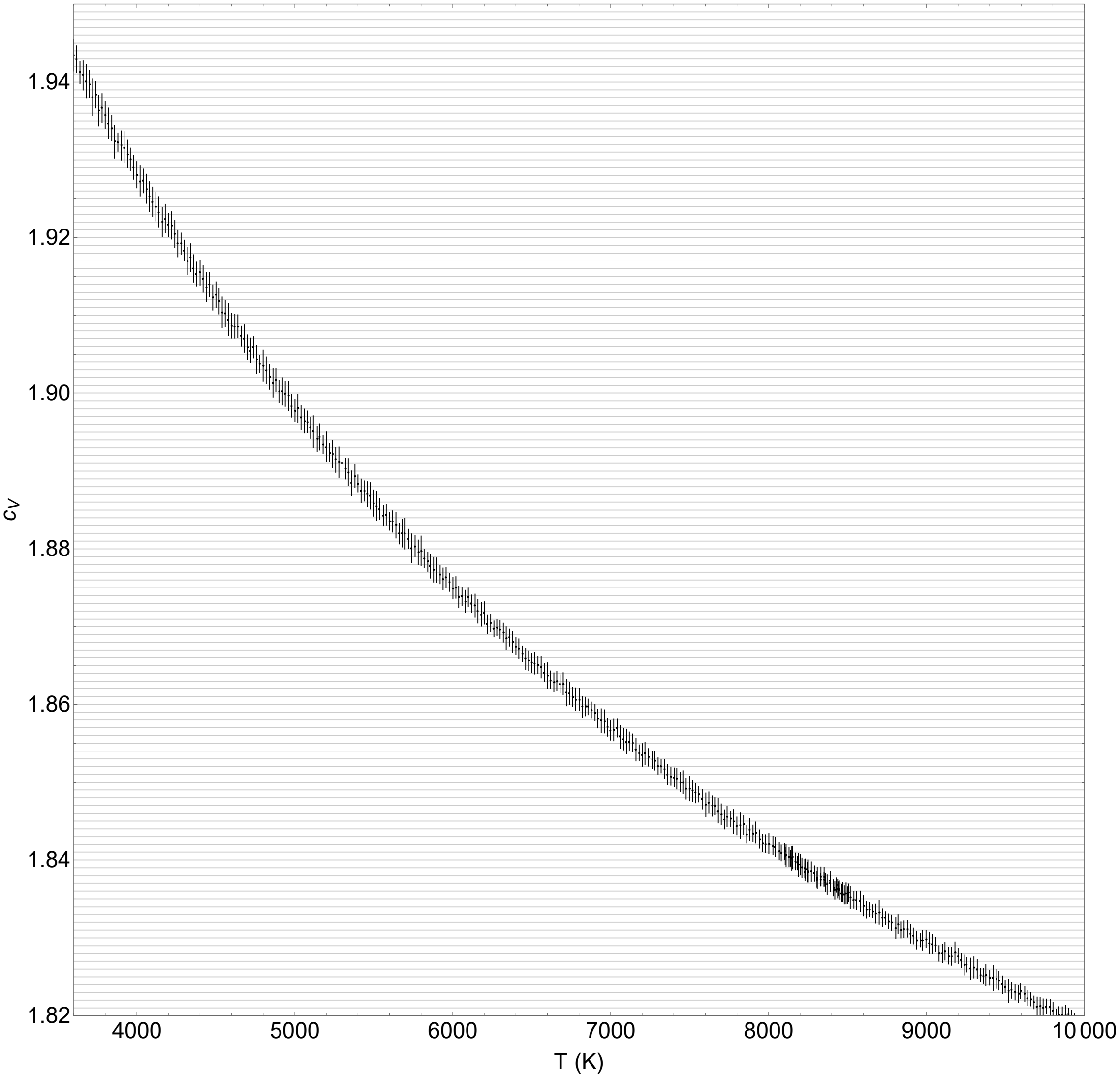

Figure 8.3: Heat capacity c_V calculated along a section of the unit isochore in Lennard-Jones units, using 20 4-million-timestep trajectories ($k_{\mathrm{B}} = 1$). The gridlines are separated by $0.001k_{\mathrm{B}}$.

8.3 Derivatives of c_V

The possibility of a first order transition was remote. Some say that a first order phase transition beyond the critical point is impossible (though this result is a bit dubious and strikes me as somewhat begging the question) [141]. In any case, we have ruled out a first order phase transition implicating c_V to a rather high degree of accuracy. Just as possible, perhaps more plausible, however, is a higher order transition in c_V. Using the thermodynamic definition of c_V,

$$c_V = T\left(\frac{\partial s}{\partial T}\right)_V, \tag{8.3.1}$$

where s is the specific entropy, we note that a first order phase transition across the FL (or "c"-transition inversion point) implies a discontinuous change in the evolution of the available phase space (roughly speaking) with temperature. The change in the evolution of phase space is known, as discussed in the chapter on chaos. A discontinuity in the derivative of c_V,

$$\left(\frac{\partial c_V}{\partial T}\right)_T = T\left(\frac{\partial^2 s}{\partial T^2}\right)_V + \left(\frac{\partial s}{\partial T}\right)_V, \tag{8.3.2}$$

is therefore indicative of a discontinuity in the curvature of entropy with temperature *if we have discarded the possibility of there being a discontinuity in the first derivative.* And so on for higher derivatives.

Calculating such derivatives numerically from c_V calculated directly from the trajectories is unacceptable. Noise in the data is amplified as high order derivatives are taken, and while the first derivative produces intelligible data, the second derivative is utterly dominated by fluctuations. There are, of course, ways of dealing with such fluctuations, but we cannot employ any smoothing when what we are looking for is a discontinuity or kink. If we wish to analyse higher order derivatives, we must calculate them from trajectories directly. We recall the expression for the heat capacity, derived almost by inspection in the canonical ensemble:

$$c_V = \frac{\langle E^2\rangle - \langle E\rangle^2}{N k_{\mathrm{B}} T^2}. \tag{3.3.9}$$

We can continue onwards. We introduce the following definitions:

$$Z = \int \mathrm{d}\Gamma \exp(-\beta\mathscr{H}), \tag{8.3.3}$$

$$\beta = \frac{1}{k_{\mathrm{B}} T}. \tag{8.3.4}$$

And we note the following useful relations:

$$\frac{1}{Z}\frac{\partial Z}{\partial \beta} = -\langle E\rangle, \tag{8.3.5}$$

$$\frac{1}{Z}\frac{\partial^2 Z}{\partial \beta^2} = \langle E^2\rangle, \tag{8.3.6}$$

$$\frac{1}{Z}\frac{\partial^3 Z}{\partial \beta^3} = -\langle E^3 \rangle, \tag{8.3.7}$$

and so on for higher derivatives. Then, we take the first two derivatives of $\langle E \rangle$:

$$\begin{aligned}\frac{\partial \langle E \rangle}{\partial \beta} &= \frac{\partial}{\partial \beta}\left(-\frac{1}{Z}\frac{\partial Z}{\partial \beta}\right),\\ &= \left(\frac{1}{Z}\frac{\partial Z}{\partial \beta}\right)^2 - \frac{1}{Z}\frac{\partial^2 Z}{\partial \beta^2}\\ &= \langle E \rangle^2 - \langle E^2 \rangle,\end{aligned} \tag{8.3.8}$$

$$\begin{aligned}\frac{\partial^2 \langle E \rangle}{\partial \beta^2} &= \frac{\partial}{\partial \beta}\left(\left(\frac{1}{Z}\frac{\partial Z}{\partial \beta}\right)^2 - \frac{1}{Z}\frac{\partial^2 Z}{\partial \beta^2}\right)\\ &= 2\left(\frac{1}{Z}\frac{\partial Z}{\partial \beta}\right)\left(-\frac{1}{Z^2}\left(\frac{\partial Z}{\partial \beta}\right)^2 + \frac{1}{Z}\left(\frac{\partial^2 Z}{\partial \beta^2}\right)^2\right)\\ &\quad + \left(\frac{1}{Z}\frac{\partial^2 Z}{\partial \beta^2}\right)\left(\frac{1}{Z}\frac{\partial Z}{\partial \beta}\right) - \frac{1}{Z}\left(\frac{\partial^3 Z}{\partial \beta^3}\right)\\ &= \langle E^3 \rangle - 3\langle E \rangle\langle E^2 \rangle + 2\langle E \rangle^3.\end{aligned} \tag{8.3.9}$$

From here, it's a matter of converting from derivatives in β to derivatives in T:

$$\frac{\partial C_V}{\partial \beta} = -2k_{\mathrm{B}}\beta C_V - \left(k_{\mathrm{B}}\beta^2\right)^2\left(\langle E \rangle^3 - 3\langle E \rangle\langle E^2 \rangle + 2\langle E \rangle^3\right), \tag{8.3.10}$$

and therefore:

$$\frac{\partial C_V}{\partial T} = -\frac{2C_V}{T} + \left(\frac{1}{k_{\mathrm{B}}T^2}\right)^2\left(\langle E^3 \rangle - 3\langle E \rangle\langle E^2 \rangle + 2\langle E \rangle^3\right). \tag{8.3.11}$$

I have derived the expression for $\frac{\partial^2 C_V}{\partial T^2}$, which involves statistical moments of E up to fourth order, but the calculation is extremely tedious, and will not end up being useful. I simply report the result here:

$$\begin{aligned}\frac{\partial^2 C_V}{\partial T^2} = \frac{2C_V}{T^2} - \frac{2}{T}\frac{\partial C_V}{\partial T} - \frac{4}{k_{\mathrm{B}}^2 T^5}\left(\langle E^3 \rangle - \langle E \rangle\langle E^3 \rangle\right) + \left(\frac{1}{k_{\mathrm{B}}T^2}\right)^3\left(\langle E^4 \rangle - \langle E^3 \rangle\langle E \rangle\right)\\ - \left(\frac{1}{k_{\mathrm{B}}T^2}\right)^2 C_V\langle E^2 \rangle - \left(\frac{1}{k_{\mathrm{B}}T^2}\right)^3\langle E \rangle\left(\langle E^3 \rangle - \langle E \rangle\langle E^2 \rangle\right) + \frac{4}{k_{\mathrm{B}}T^3}\langle E \rangle C_V\\ - \frac{2}{k_{\mathrm{B}}T}C_V^2 - \frac{2}{k_{\mathrm{B}}T^2}\langle E \rangle\frac{\partial C_V}{\partial T}.\end{aligned} \tag{8.3.12}$$

Ideally one would wish to transform Eq. 8.3.11 into the NVE ensemble, but this is a very tricky business which I won't get into here. We will therefore attempt our calculation of $\frac{\partial C_V}{\partial T}$ from an NVT trajectory. As in the previous section, we use very long trajectories, split up into subtrajectories which were treated as separate initial conditions

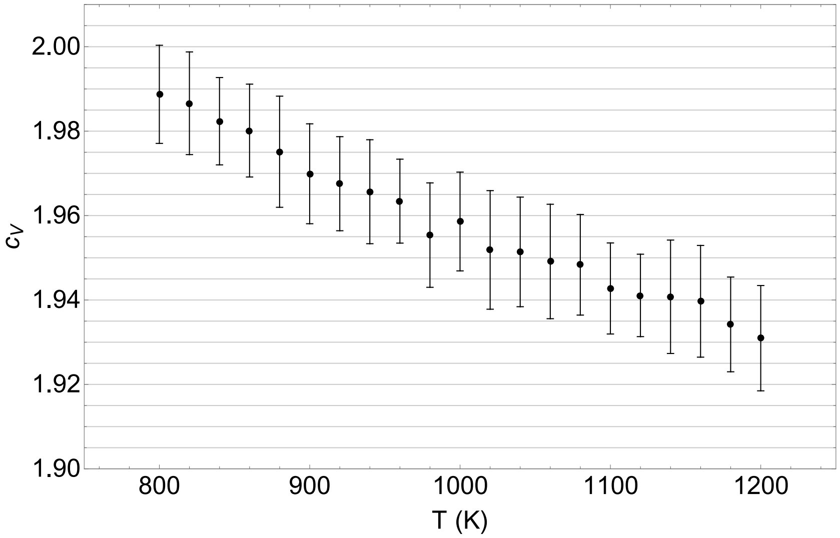

Figure 8.4: Heat capacity c_V calculated along the 1.35 g ml^{-1} isochore in the NVT thermostat with a friction constant of $1ps$, using 40 36-million-timestep trajectories ($k_\mathrm{B} = 1$). The gridlines are separated by $0.005k_\mathrm{B}$.

and from which data were gathered. However, the four million timestep subtrajectories were vastly unsatisfactory for the task at hand - the standard deviation of c_V itself was almost $0.1k_\mathrm{B}$ for such trajectories, almost 50 times higher than in the NVE ensemble. This problem was seen for many different thermostat coupling strengths. By increasing the length of the subtrajectories to thirty-six million (!) timesteps, the uncertainty on c_V can be reduced to about $0.01k_\mathrm{B}$ - a fifth of the precision at the cost of nine times the computational work compared to NVE measurements. These results are shown in Fig. 8.4, calculated along the 1.35 g ml^{-1} isochore with 40 subtrajectories.

From these trajectories, using Eq. 8.3.11, I calculated $\frac{\partial c_V}{\partial T}$. These results are plotted in Fig. 8.5, where we can see that my approach has failed to produce anything meaningful. The uncertainty in each point is an order of magnitude larger than its absolute value and these results could not be trusted if I took the time to extend the temperature range. The NVE ensemble is clearly much neater than the NVT ensemble when it comes to calculating fluctuation properties. A brute-force method of reducing fluctuations is simply increasing the length of the trajectories, though this comes at a devastating computational cost. Taking the average over a vast number of initial conditions will allow the convergence of the derivative to a sensible value but the uncertainty on that value would be unacceptably high. Alternative solutions to this problem, including an analytical expression for $\frac{\partial C_V}{\partial T}$ in the NVE ensemble, are currently underway. For now, this chapter ends simply as a report of what has been done to ascertain a phase transition.

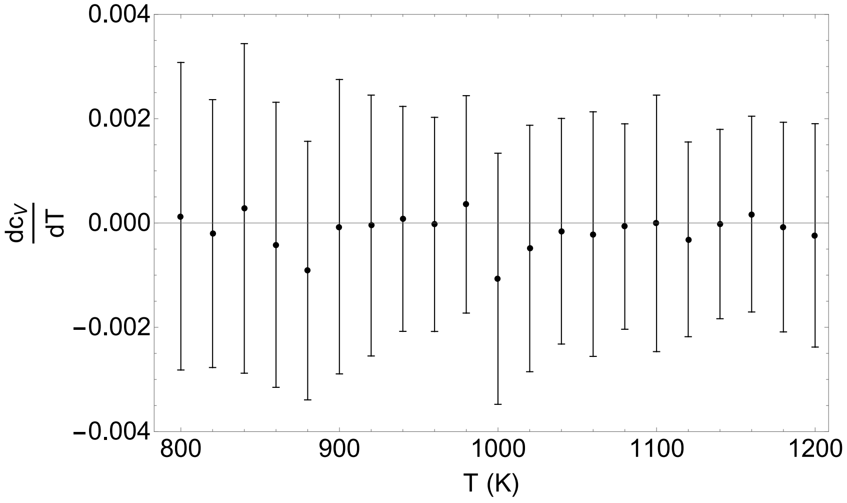

Figure 8.5: Derivative of the heat capacity $\frac{\partial c_V}{\partial T}$ calculated along the 1.35 g ml^{-1} isochore in the NVT thermostat with a friction constant of $1ps$, using 40 36-million-timestep trajectories ($k_\mathrm{B} = 1$).

Chapter 9

Beyond Super and Subcritical

9.1 Conclusions

The supercritical state has had a long but somewhat barren history. There is a sense in which the critical point itself has been for an obstacle to the study of the supercritical state. This is not an entirely unreasonable eventuality, for the critical point raises very interesting questions about the nature of the boiling line it terminates and about the states the boiling line separates. However the continuous disappearance, or rather weakening, of the near-critical anomalies into obscurity in the deep supercritical state has the potential for deceit. The near-critical anomalies are echoes of the boiling line, but their termination must not be taken out of context. The boiling line is a particular manifestation of the fundamental transition from a mixed dynamical state to a pure dynamical state via the disappearance of molecular oscillation. Does such a transition happen even in deeply supercritical states far from the critical point? Of course it must. So we ought to be optimistic in our estimation of the supercritical state. Using the old thought experiment, if we continuously thermodynamically transform a liquid into a gas by taking a path which skirts far beyond the critical point, with our modern understanding of the liquid state, we know we must pass from states where the thermodynamics is governed by a mixed dynamical state of disappearing oscillations and dominating diffusion events to states where the thermodynamics is governed by a pure dynamical state of chaotic collisions. These states are not only different instantaneously, but their evolution along any phase diagram path is different. A mixed dynamical state has competing effects which wax or wane, a pure dynamical state evolves more... unanimously. Some sort of transition is inevitable, and we should be very careful to assume its unimportance.

The FL is born in the constructive distinction between liquids and gases of particle dynamics. The distinction between liquidlike and gaslike on the basis of oscillatory motion is as old as corpuscle theory, and the use of VAFs to meaasure this distinction goes back to the early days of MD simulations [142, 143, 144]. The proposition of the FL and its definition in the VAF criterion guides our gaze in the vast supercritical so that we might find wide transitions occurring far from the critical point. The VAF criterion, though rather rough, has the strong advantage of being path independent. The crossover of particle dynamics affects other physical quantities of the supercritical system. Viscosity, speed of sound and thermal conductivity all decrease with temperature in the liquidlike regime but increase with temperature above the line as in gases. Furthermore, the diffusion constant crosses over from exponential temperature dependence in the liquidlike regime to power-law dependence as in gases. These definitions all depend on the path chosen on the phase diagram, the crossovers and minima of these properties may deviate from the FL [41]. The VAF criterion defines a line on the phase diagram which is path independent.

The link between dynamics and structure is no secret, and structure is amenable to experimentation, gives ready insight into the energetics of a system, and is an intuitive description of the system's microscopic nature. It is for this reason that I am among many early pioneers who have investigated the structural changes implicated with the FL, using simulations or experiments. Argon, neon, and nitrogen all sport moderate crossovers in structure [46, 47, 76], and the trends established in these projects guided my own work in the structure of supercritical fluids. Water and carbon dioxide are, as has been heavily emphasised, important compounds. They both see extensive use industrially and environmentally in their supercritical forms, carbon dioxide is prevalent in its supercritical form in the Venerean atmosphere, and water needs no introduction as the most studied compound in science. It is natural that these compounds would be the next step for research of the implications of the FL.

The transition in water was a surprise. It also hinted at a very rich collection of behaviours of different fluids across the FL. Water's interesting structure and its strange evolution with temperature have been seen to be intimately connected with the FL. This is not a surprise if we consider the dynamical transition at the FL to be a fundamental idea to the study of liquids and supercritical fluids. Every fluid has a FL, and a fluid with an interesting liquid state will have an interesting transition at the FL. Specifically we saw from RDFs, angular distribution functions, and coordination distributions that the FL sits at the apex of water's transition between tetrahedral and disordered closely packed structures. The structural evolution with temperature was noticeably different in these states which the FL separated, revealing that the dynamical distinction between these states is significant. Water also exhibits the sort of transitions seen previously in argon [76]. These two observations demonstrate not only the diverse implications of the FL but also its very fundamental nature.

Carbon dioxide, too, showed the same subtle crossover in structural correlations as argon. This crossover in the heights of the first peak is related to the other transition observed, which shows the FL to be the point of deviation from uniform expansion in the liquidlike state, beyond which carbon dioxide loses its short-medium range order due to the decoupling of the first nearest neighbour distance from the density. This is the sort of transition that does not occur in every liquid, but the mechanism is good to have been associated with the FL. These different but related discoveries in water and carbon dioxide are important additions to the literature of structural crossovers at the FL. With this work, structural crossovers have been seen in experiments or simulations across the FL in argon [76], neon [46], nitrogen [47], water [74], and carbon dioxide [90]. This is a diverse range of systems, and the observations made regarding them will guide and inspire future work concerning the implications of the FL.

My work on dynamical instability in the supercritical state follows in a similar vein to my work on water and carbon dioxide in the sense that I am probing new implications of the FL. The similarity ends here, however, because dynamical instability is a very "low-level" property of the phase space and is amenable only to theoretical (as opposed to any experimental measurements) consideration for thermodynamic systems. The maximal Lyapunov exponent is very sensitive to changes of macroscopic phase and can give clues to the nature of a transition which "higher-level" techniques would be insensitive to. We saw that, unlike at the melting transition, the maximal Lyapunov exponent underwent a smooth transition as it crossed the Frenkel line. On the gaslike side of this transition, the exponent follows a very simple relationship with energy which I explain according to the simplicity of the dynamics, as opposed to the mixed dynamical state of liquids. This work was the first of its kind, exploring the dynamical instability of the supercritical state and doing so in the shadow of Frenkel's theory. Analysis of dynamical instability is a useful tool, especially concerning states which we poorly understand. This work will inspire, in me and I hope in others, further investigation into the chaos of supercritical fluids.

A goal from the very beginning of the project was to get to the bottom of the transition at the FL. It's not clear whether the "c"-transition is the beginning of final stretch of this goal, or has simply raised further questions. The "c"-transition speaks for itself, but is elucidated by Frenkel theory. It makes evident the singular importance of dynamics, and in particular collective dynamics, in understanding the fluid states of matter. We still have only a motivation, rather than an explanation, for *why* the "c"-transition occurs. The "c"-transition, it seems to Kostya and me, is for an apotheosis to all the work done on the FL so far. When it comes to future work, this is what I shall focus on.

9.2 Further Work

The first order of business is to extend the study of the "c"-transition to a greater variety of fluids. Water is an obvious choice. Simulations of supercritical water towards this end are currently underway. Other systems or interest are molten metals, such as lead or gallium, more complex molecular liquids, such as ethane or ammonia, fluid mixtures such as molten sodium chloride, and possibly even exotic fluids such as plasmas. The exception of near critical paths to the "c"-transition is perhaps not surprising, but it certainly is profound and sets these states apart from other fluid states. Simulating more near-critical paths and subcritical paths and subjecting them to "c"-transition analysis may help shed light on how these states can be so different. Likewise, certain isochores straddle the boiling line and therefore contain liquid-gas mixtures. These states could be interesting to study. Combining analysis of dynamical instability with the "c"-transition analysis could be very interesting too.

There is tentative evidence that the "c"-transition may manifest in a modified definition of λ_d using the "longitudinal" Maxwell relaxation time, $\tau^\mathrm{L} = \frac{\zeta + \frac{4}{3}\eta}{K}$, where K is the bulk modulus and ζ is the bulk viscosity. This is important because the bulk modulus of a fluid is possible to measure directly via experimentation, unlike the shear modulus which can at best be inferred. An experimental observation of the "c"-transition would be a very valuable discovery.

Finally, there is the question of a phase transition associated with the “c”-transition. Reducing the uncertainty in c_V to below $0.001k_\mathrm{B}$ is a straightforward but taxing matter. The matter of reducing fluctuations in NVT ensemble calculations is also currently underway. One can also approach the topic from another point of view. We have our special parameter λ_d, we can investigate how it evolves in the liquidlike and gaslike states and see what we find. The idea of a phase transition in the supercritical state is contrary to all traditional knowledge, but there is no definitely *proof* of an absence of a phase transition beyond the critical point - we are exploring the possibility. There’s certainly something going on, and attacking it from several angles will help us better understand it.

Bibliography

[1] A. V. Granato, "The specific heat of simple liquids," *Journal of Non-Crystalline Solids*, vol. 307-310, pp. 376–386, sep 2002.

[2] J. Frenkel, *Kinetic Theory of Liquids.* New York: Doe, ver ed., 1955.

[3] J.-P. Boon and S. Yip, *Molecular hydrodynamics.* Dover Publications, 1991.

[4] S. Chapman and T. G. Cowling, *The mathematical theory of non-uniform gases.* Cambridge: Cambridge University Press, 1990.

[5] D. J. Evans and D. J. Searles, "Equilibrium microstates which generate second law violating steady states," *Physical Review E*, vol. 50, pp. 1645–1648, aug 1994.

[6] J.-P. Hansen and I. R. McDonald, *Theory of simple liquids.* Elsevier Academic Press, 2006.

[7] L. D. Landau and E. M. Lifshitz, *Statistical Physics.* Oxford: Elsevier Butterworth-Heinemann, 3 ed., 1980.

[8] U. U. Balucani and M. Zoppi, *Dynamics of the liquid state.* Clarendon Press, 1994.

[9] Frederick Reif, *Fundamentals of Statistical and Thermal Physics.* Waveland Press, 2010.

[10] A.-L. de Lavoisier, *Oeuvres de Lavoisier, publiées par les soins de son excellence le ministre de l'instruction publique et des Cultes*, vol. 2. Paris: Impr. impériale, 1862.

[11] M. Faraday, "On fluid chlorine," *Philosophical Transactions of the Royal Society of London*, vol. 113, pp. 160–165, dec 1823.

[12] M. Faraday, "XVII. On the condensation of several gases into liquids," *Philosophical Transactions of the Royal Society of London*, vol. 113, pp. 189–198, dec 1823.

[13] C. Cagniard de la Tour, "Exposé de quelques résultats obtenu par l'action combinée de la chaleur et de la compression sur certains liquides, tels que l'eau, l'alcool, l'éther sulfurique et l'essence de pétrole rectifiée," *Ann. Chim. Phys.*, vol. 21, pp. 127–132, 1822.

[14] C. Cagniard de la Tour, "Nouvelle note sur les effets qu'on obtient par l'application simultanée de la chaleur et de la compression a certains liquides," *Ann. Chim. Phys.*, vol. 22, pp. 410–415, 1823.

[15] T. Andrews, "On the continuity of the gaseous and liquid states of matter ," *Philosophical Transactions of the Royal Society of London*, vol. 159, pp. 575–590, dec 1869.

[16] J.-L. Barrat and J.-P. Hansen, *Basic Concepts for Simple and Complex Liquids.* Cambridge University Press, mar 2003.

[17] E. Kiran, P. G. Debenedetti, and C. J. Peters, *Supercritical Fluids: Fundamentals and Applications (NATO Science Series E: Applied Sciences vol 366).* Boston: Kluwer, 2000.

[18] K. Nishikawa and T. Morita, "Inhomogeneity of molecular distribution in supercritical fluids," *Chemical Physics Letters*, vol. 316, pp. 238–242, jan 2000.

[19] H. Nakayama, K. I. Saitow, M. Sakashita, K. Ishii, and K. Nishikawa, "Raman spectral changes of neat CO2 across the ridge of density fluctuation in supercritical region," *Chemical Physics Letters*, vol. 320, pp. 323–327, apr 2000.

[20] K. Nishikawa, K. Kusano, A. A. Arai, and T. Morita, "Density fluctuation of a van der Waals fluid in supercritical state," *Journal of Chemical Physics*, vol. 118, pp. 1341–1346, jan 2003.

[21] T. Sato, M. Sugiyama, K. Itoh, K. Mori, T. Fukunaga, M. Misawa, T. Otomo, and S. Takata, "Structural difference between liquidlike and gaslike phases in supercritical fluid," *Physical Review E - Statistical, Nonlinear, and Soft Matter Physics*, vol. 78, p. 051503, nov 2008.

[22] L. Xu, P. Kumar, S. V. Buldyrev, S. H. Chen, P. H. Poole, F. Sciortino, and H. E. Stanley, "Relation between the Widom line and the dynamic crossover in systems with a liquid-liquid phase transition," *Proceedings of the National Academy of Sciences of the United States of America*, vol. 102, pp. 16558–16562, nov 2005.

[23] V. V. Brazhkin, Y. D. Fomin, A. G. Lyapin, V. N. Ryzhov, E. N. Tsiok, and K. Trachenko, ""Liquid-Gas" Transition in the Supercritical Region: Fundamental Changes in the Particle Dynamics," *Physical Review Letters*, vol. 111, p. 145901, oct 2013.

[24] V. V. Brazhkin, Y. D. Fomin, A. G. Lyapin, V. N. Ryzhov, and K. Trachenko, "Two liquid states of matter: A dynamic line on a phase diagram," *Physical Review E*, vol. 85, p. 031203, mar 2012.

[25] V. V. Brazhkin and K. Trachenko, "What separates a liquid from a gas?," *Physics Today*, vol. 65, pp. 68–69, nov 2012.

[26] J. McHardy and S. P. Sawan, *Sawan, Supercritical Fluid Cleaning: Fundamentals, Technology and Applications.* Westwood: Noyes Publications, 1998.

[27] G. Brunner, "Applications of Supercritical Fluids," *Annual Review of Chemical and Biomolecular Engineering*, vol. 1, pp. 321–342, jun 2010.

[28] E. S. Alekseev, A. Y. Alentiev, A. S. Belova, V. I. Bogdan, T. V. Bogdan, A. V. Bystrova, E. R. Gafarova, E. N. Golubeva, E. A. Grebenik, O. I. Gromov, V. A. Davankov, S. G. Zlotin, M. G. Kiselev, A. E. Koklin, Y. N. Kononevich, A. E. Lazhko, V. V. Lunin, S. E. Lyubimov, O. N. Martyanov, I. I. Mishanin, A. M. Muzafarov, N. S. Nesterov, A. Y. Nikolaev, R. D. Oparin, O. O. Parenago, O. P. Parenago, Y. A. Pokusaeva, I. A. Ronova, A. B. Solovieva, M. N. Temnikov, P. S. Timashev, O. V. Turova, E. V. Filatova, A. A. Philippov, A. M. Chibiryaev, and A. S. Shalygin, "Supercritical fluids in chemistry," *Russian Chemical Reviews*, vol. 89, pp. 1337–1427, dec 2020.

[29] J. E. Proctor and H. E. Maynard-Casely, *The Liquid and Supercritical Fluid States of Matter.* Boca Raton: CRC Press, 1st ed., sep 2020.

[30] W. Leitner, "Supercritical carbon dioxide as a green reaction medium for catalysis," *Accounts of Chemical Research*, vol. 35, pp. 746–756, sep 2002.

[31] C. A. Eckert, B. L. Knutson, and P. G. Debenedetti, "Supercritical fluids as solvents for chemical and materials processing," *Nature*, vol. 383, pp. 313–318, sep 1996.

[32] P. E. Savage, S. Gopalan, T. I. Mizan, C. J. Martino, and E. E. Brock, "Reactions at supercritical conditions: Applications and fundamentals," *AIChE Journal*, vol. 41, no. 7, pp. 1723–1778, 1995.

[33] E. J. Beckman, "Supercritical and near-critical CO2 in green chemical synthesis and processing," *The Journal of Supercritical Fluids*, vol. 28, pp. 121–191, mar 2004.

[34] P. G. Jessop, T. Ikariya, and R. Noyori, "Homogeneous Catalysis in Supercritical Fluids," *Chemical Reviews*, vol. 99, no. 2-3, pp. 475–493, 1999.

[35] D. J. Evans and G. P. Morriss, *Statistical mechanics of nonequilibrium liquids.* Academic Press, 1990.

[36] L. P. Kadanoff and P. C. Martin, "Hydrodynamic equations and correlation functions," *Annals of Physics*, vol. 24, pp. 419–469, oct 1963.

[37] J. C. Maxwell, "On the dynamical theory of gases," *Philosophical Transactions of the Royal Society of London*, vol. 157, pp. 49–88, 1867.

[38] J. Frenkel, "Continuity of the Solid and the Liquid States," *Nature*, vol. 136, pp. 167–168, aug 1935.

[39] L Brillouin, *Tensors in Mechanics and Elasticity.* New York: Academic Press, 1964.

[40] J. C. Dyre, "Colloquium: The glass transition and elastic models of glass-forming liquids," *Reviews of Modern Physics*, vol. 78, pp. 953–972, sep 2006.

[41] K. Trachenko and V. V. Brazhkin, "Collective modes and thermodynamics of the liquid state," *Reports on Progress in Physics*, vol. 79, p. 016502, jan 2016.

[42] D. Bolmatov, V. V. Brazhkin, and K. Trachenko, "The phonon theory of liquid thermodynamics," *Scientific Reports*, vol. 2, p. 421, dec 2012.

[43] J. E. Proctor, "Modeling of liquid internal energy and heat capacity over a wide pressure-temperature range from first principles," *Physics of Fluids*, vol. 32, p. 107105, oct 2020.

[44] E. Kiran, P. G. Debenedetti, and C. J. Peters, *Supercritical Fluids: Fundamentals and Applications.* Boston: Kluwer, 2000.

[45] S. M. Stishov, "Phase Transition in Expanded Matter," *JETP Lett.*, vol. 57, p. 196, 1993.

[46] C. Prescher, Y. D. Fomin, V. B. Prakapenka, J. Stefanski, K. Trachenko, and V. V. Brazhkin, "Experimental evidence of the Frenkel line in supercritical neon," *Physical Review B*, vol. 95, p. 134114, apr 2017.

[47] J. E. Proctor, C. G. Pruteanu, I. Morrison, I. F. Crowe, and J. S. Loveday, "Transition from Gas-like to Liquid-like Behavior in Supercritical N2," *Journal of Physical Chemistry Letters*, vol. 10, pp. 6584–6589, nov 2019.

[48] D. Smith, M. A. Hakeem, P. Parisiades, H. E. Maynard-Casely, D. Foster, D. Eden, D. J. Bull, A. R. L. Marshall, A. M. Adawi, R. Howie, A. Sapelkin, V. V. Brazhkin, and J. E. Proctor, "Crossover between liquidlike and gaslike behavior in C H 4 at 400 K," *Physical Review E*, vol. 96, p. 052113, nov 2017.

[49] J. E. Proctor, M. Bailey, I. Morrison, M. A. Hakeem, and I. F. Crowe, "Observation of Liquid-Liquid Phase Transitions in Ethane at 300 K," *Journal of Physical Chemistry B*, vol. 122, pp. 10172–10178, nov 2018.

[50] L. Wang, C. Yang, M. T. Dove, V. V. Brazhkin, and K. Trachenko, "Thermodynamic heterogeneity and crossover in the supercritical state of matter," *Journal of Physics: Condensed Matter*, vol. 31, p. 225401, jun 2019.

[51] G. Battimelli, G. Ciccotti, and P. Greco, *Computer Meets Theoretical Physics.* Springer International Publishing, 2020.

[52] M. Tuckerman, *Statistical Mechanics: Theory and Molecular Simulation.* Oxford: Oxford University Press, 2010.

[53] M. P. Allen and D. J. Tildesley, *Computer Simulation of Liquids.*, vol. 57. Clarendon Press, 1991.

[54] J. L. F. Abascal and C. Vega, “A general purpose model for the condensed phases of water: TIP4P/2005,” *The Journal of Chemical Physics*, vol. 123, p. 234505, dec 2005.

[55] C. Vega and J. L. F. Abascal, “Simulating water with rigid non-polarizable models: a general perspective,” *Physical Chemistry Chemical Physics*, vol. 13, p. 19663, nov 2011.

[56] C. Vega, J. L. F. Abascal, M. M. Conde, and J. L. Aragones, “What ice can teach us about water interactions: a critical comparison of the performance of different water models,” *Faraday Discuss.*, vol. 141, pp. 251–276, nov 2009.

[57] P. Gallo, D. Corradini, and M. Rovere, “Widom line and dynamical crossovers as routes to understand supercritical water,” *Nature Communications*, vol. 5, p. 5806, dec 2014.

[58] M. Gao, A. J. Misquitta, C. Yang, I. T. Todorov, A. Mutter, and M. T. Dove, “Molecular dynamics study of CO2 absorption and desorption in zinc imidazolate frameworks,” *Molecular Systems Design & Engineering*, vol. 2, pp. 457–469, oct 2017.

[59] U. Seifert, “Stochastic thermodynamics, fluctuation theorems and molecular machines,” *Reports on Progress in Physics*, vol. 75, p. 126001, nov 2012.

[60] S. C. Harvey, R. K.-Z. Tan, and T. E. Cheatham III, “The Flying Ice Cube: Velocity Rescaling in Molecular Dynamics Leads to Violation of Energy Equipartition,” *Journal of Computational Chemistry*, vol. 19, no. 7, 7267.

[61] T. Schlick, *Molecular Modeling and Simulation: An Interdisciplinary Guide.* New York: Springer, 2 ed., 2010.

[62] S. Melchionna, G. Ciccotti, and B. L. Holian, “Hoover npt dynamics for systems varying in shape and size,” *Molecular Physics*, vol. 78, pp. 533–544, feb 1993.

[63] D. Quigley and M. I. Probert, “Langevin dynamics in constant pressure extended systems,” *Journal of Chemical Physics*, vol. 120, pp. 11432–11441, jun 2004.

[64] I. T. Todorov, W. Smith, K. Trachenko, and M. T. Dove, “DL_POLY_3: new dimensions in molecular dynamics simulations via massive parallelism,” *Journal of Materials Chemistry*, vol. 16, p. 1911, may 2006.

[65] P. H. Poole, F. Sciortino, U. Essmann, and H. E. Stanley, “Phase behaviour of metastable water,” *Nature*, vol. 360, pp. 324–328, nov 1992.

[66] P. Gallo, K. Amann-Winkel, C. A. Angell, M. A. Anisimov, F. Caupin, C. Chakravarty, E. Lascaris, T. Loerting, A. Z. Panagiotopoulos, J. Russo, J. A. Sellberg, H. E. Stanley, H. Tanaka, C. Vega, L. Xu, and L. G. M. Pettersson, "Water: A Tale of Two Liquids," *Chemical Reviews*, vol. 116, pp. 7463–7500, jul 2016.

[67] Y. Katayama, T. Hattori, H. Saitoh, T. Ikeda, K. Aoki, H. Fukui, and K. Funakoshi, "Structure of liquid water under high pressure up to 17 GPa," *Physical Review B - Condensed Matter and Materials Physics*, vol. 81, p. 014109, jan 2010.

[68] A. Soper, "The radial distribution functions of water and ice from 220 to 673 K and at pressures up to 400 MPa," *Chemical Physics*, vol. 258, pp. 121–137, aug 2000.

[69] T. Ikeda, Y. Katayama, H. Saitoh, and K. Aoki, "High-temperature water under pressure," *The Journal of Chemical Physics*, vol. 132, p. 121102, mar 2010.

[70] J. Marti, "Analysis of the hydrogen bonding and vibrational spectra of supercritical model water by molecular dynamics simulations," *The Journal of Chemical Physics*, vol. 110, pp. 6876–6886, apr 1999.

[71] O. Chara, A. N. McCarthy, and J. R. Grigera, "Crossover between tetrahedral and hexagonal structures in liquid water," *Physics Letters A*, vol. 375, pp. 572–576, jan 2011.

[72] C. Yang, V. V. Brazhkin, M. T. Dove, and K. Trachenko, "Frenkel line and solubility maximum in supercritical fluids," *Physical Review E*, vol. 91, p. 012112, jan 2015.

[73] Y. E. Gorbaty and Y. N. Demianets, "The pair-correlation functions of water at a pressure of 1000 bar in the temperature range 25-500°C," *Chemical Physics Letters*, vol. 100, pp. 450–454, aug 1983.

[74] C. Cockrell, O. A. Dicks, V. V. Brazhkin, and K. Trachenko, "Pronounced structural crossover in water at supercritical pressures," *Journal of Physics: Condensed Matter*, vol. 32, p. 385102, sep 2020.

[75] A. A. Maradudin, E. W. Ontroll, G. H. Weiss, and I. P. Ipatova, *Theory of lattice dynamics in the harmonic approximation by A. A. Maradudin.* New York: Academic Press, 1971.

[76] L. Wang, C. Yang, M. T. Dove, Y. D. Fomin, V. V. Brazhkin, and K. Trachenko, "Direct links between dynamical, thermodynamic, and structural properties of liquids: Modeling results," *Physical Review E*, vol. 95, p. 032116, mar 2017.

[77] T. Sarbu, T. Styranec, and E. J. Beckman, "Non-fluorous polymers with very high solubility in supercritical CO2 down to low pressures," *Nature*, vol. 405, pp. 165–168, may 2000.

[78] J. M. DeSimone, Z. Guan, and C. S. Elsbernd, "Synthesis of fluoropolymers in supercritical carbon dioxide," *Science*, vol. 257, pp. 945–947, aug 1992.

[79] A. I. Cooper, "Polymer synthesis and processing using supercritical carbon dioxide," *Journal of Materials Chemistry*, vol. 10, pp. 207–234, jan 2000.

[80] J. M. Blackburn, D. P. Long, A. Cabañas, and J. J. Watkins, "Deposition of conformal copper and nickel films from supercritical carbon dioxide," *Science*, vol. 294, pp. 141–145, oct 2001.

[81] J. M. DeSimone, "Practical approaches to green solvents," *Science*, vol. 297, pp. 799–803, aug 2002.

[82] C. J. Li and B. M. Trost, "Green chemistry for chemical synthesis," *Proceedings of the National Academy of Sciences of the United States of America*, vol. 105, pp. 13197–13202, sep 2008.

[83] P. T. Anastas and M. M. Kirchhoff, "Origins, current status, and future challenges of green chemistry," *Accounts of Chemical Research*, vol. 35, pp. 686–694, sep 2002.

[84] P. Anastas and N. Eghbali, "Green Chemistry: Principles and Practice," *Chem. Soc. Rev.*, vol. 39, pp. 301–312, dec 2010.

[85] D. J. Cole-Hamilton, "Homogeneous catalysis - New approaches to catalyst separation, recovery, and recycling," *Science*, vol. 299, pp. 1702–1706, mar 2003.

[86] J. A. Dahl, B. L. Maddux, and J. E. Hutchison, "Toward greener nanosynthesis," *Chemical Reviews*, vol. 107, pp. 2228–2269, jun 2007.

[87] P. G. Jessop, Y. Hsiao, T. Ikariya, and R. Noyori, "Homogeneous Catalysis in Supercritical Fluids: Hydrogenation of Supercritical Carbon Dioxide to Formic Acid, Alkyl Formates, and Formamides," *Journal of the American Chemical Society*, vol. 118, pp. 344–355, jan 1996.

[88] E. Reverchon, "Supercritical fluid extraction and fractionation of essential oils and related products," *Journal of Supercritical Fluids*, vol. 10, pp. 1–37, apr 1997.

[89] C. Song, "Global challenges and strategies for control, conversion and utilization of CO2 for sustainable development involving energy, catalysis, adsorption and chemical processing," *Catalysis Today*, vol. 115, pp. 2–32, jun 2006.

[90] C. J. Cockrell, O. Dicks, L. Wang, K. Trachenko, A. K. Soper, V. V. Brazhkin, and S. Marinakis, "Experimental and modeling evidence for structural crossover in supercritical CO2," *Physical Review E*, vol. 101, p. 052109, may 2020.

[91] M. S. Green, "Markoff random processes and the statistical mechanics of time-dependent phenomena," *The Journal of Chemical Physics*, vol. 20, pp. 1281–1295, aug 1952.

[92] K. Tsujia, Y. Katayama, Y. Morimoto, and O. Shimomura, "Structure of liquid rubidium under high pressure," *Journal of Non-Crystalline Solids*, vol. 205-207, pp. 295–298, oct 1996.

[93] Y. Katayama and K. Tsuji, "X-ray structural studies on elemental liquids under high pressures," *Journal of Physics: Condensed Matter*, vol. 15, pp. 6085–6103, sep 2003.

[94] S. Yamamoto, Y. Ishibashi, Y. Inamura, Y. Katayama, T. Mishina, and J. . Ichiro Nakahara, "Pressure dependence of local structure in liquid carbon disulfide," *J. Chem. Phys*, vol. 124, p. 144511, 2006.

[95] H. Akaike, "A New Look at the Statistical Model Identification," *IEEE Transactions on Automatic Control*, vol. 19, no. 6, pp. 716–723, 1974.

[96] G. Schwarz, "Estimating the Dimension of a Model," *https://doi.org/10.1214/aos/1176344136*, vol. 6, pp. 461–464, mar 1978.

[97] National Institute of Standards and Technology, "Thermophysical Properties of Fluid Systems." https://webbook.nist.gov/chemistry/fluid/.

[98] J. R. Dorfman, *An Introduction to Chaos in Nonequilibrium Statistical Mechanics.* Cambridge University Press, aug 1999.

[99] B. M. Boghosian, P. V. Coveney, and H. Wang, "A New Pathology in the Simulation of Chaotic Dynamical Systems on Digital Computers," *Advanced Theory and Simulations*, vol. 2, p. 1900125, dec 2019.

[100] J. R. Dorfman and P. Gaspard, "Chaotic scattering theory of transport and reaction-rate coefficients," *Physical Review E*, vol. 51, pp. 28–35, jan 1995.

[101] P. Gaspard, *Chaos, Scattering and Statistical Mechanics.* Cambridge University Press, may 1998.

[102] C. Cockrell, O. Dicks, V. Brazhkin, and K. Trachenko, "Pronounced structural crossover in water at supercritical pressures," *Journal of Physics Condensed Matter*, vol. 32, no. 38, 2020.

[103] C. Yang, M. Dove, V. Brazhkin, and K. Trachenko, "Emergence and Evolution of the k Gap in Spectra of Liquid and Supercritical States," *Physical Review Letters*, vol. 118, p. 215502, may 2017.

[104] G. Benettin, L. Galgani, and J. M. Strelcyn, "Kolmogorov entropy and numerical experiments," *Physical Review A*, vol. 14, pp. 2338–2345, dec 1976.

[105] S. K. Nayak, R. Ramaswamy, and C. Chakravarty, "Maximal Lyapunov exponent in small atomic clusters," *Physical Review E*, vol. 51, pp. 3376–3380, apr 1995.

[106] V. Mehra and R. Ramaswamy, "Curvature fluctuations and the lyapunov exponent at melting," *Physical Review E - Statistical Physics, Plasmas, Fluids, and Related Interdisciplinary Topics*, vol. 56, pp. 2508–2517, sep 1997.

[107] C. Dellago and H. A. Posch, "Kolmogorov - Sinai entropy and Lyapunov spectra of a hard-sphere gas," *Physica A: Statistical Mechanics and its Applications*, vol. 240, pp. 68–83, jun 1997.

[108] K. H. Kwon and B. Y. Park, "Lyapunov exponent and the solid-fluid phase transition," *Journal of Chemical Physics*, vol. 107, pp. 5171–5178, oct 1997.

[109] S. K. Nayak, P. Jena, K. D. Ball, and R. S. Berry, "Dynamics and instabilities near the glass transition: From clusters to crystals," *Journal of Chemical Physics*, vol. 108, pp. 234–239, jan 1998.

[110] H. A. Posch and W. G. Hoover, "Lyapunov instability of dense Lennard-Jones fluids," *Physical Review A*, vol. 38, pp. 473–482, jul 1988.

[111] P. Gaspard and G. Nicolis, "Transport properties, Lyapunov exponents, and entropy per unit time," *Physical Review Letters*, vol. 65, pp. 1693–1696, oct 1990.

[112] D. J. Evans, E. G. Cohen, and G. P. Morriss, "Viscosity of a simple fluid from its maximal Lyapunov exponents," *Physical Review A*, vol. 42, pp. 5990–5997, nov 1990.

[113] G. E. Norman and V. V. Stegailov, "Stochastic theory of the classical molecular dynamics method," *Mathematical Models and Computer Simulations*, vol. 5, pp. 305–333, jul 2013.

[114] L. A. Bunimovich and Y. G. Sinai, "Markov Partitions for dispersed billiards," *Communications in Mathematical Physics*, vol. 78, pp. 247–280, dec 1980.

[115] H. A. Posch and W. G. Hoover, "Equilibrium and nonequilibrium Lyapunov spectra for dense fluids and solids," *Physical Review A*, vol. 39, pp. 2175–2188, feb 1989.

[116] P. Butera and G. Caravati, "Phase transitions and Lyapunov characteristic exponents," *Physical Review A*, vol. 36, pp. 962–964, jul 1987.

[117] G. M. Tanner, A. Bhattacharya, S. K. Nayak, and S. D. Mahanti, "Dynamics of melting argon clusters," *Physical Review E*, vol. 55, pp. 322–328, jan 1997.

[118] J. Barré and T. Dauxois, "Lyapunov exponents as a dynamical indicator of a phase transition," *EPL (Europhysics Letters)*, vol. 55, no. 2, p. 164, 2001.

[119] M. Colonna and A. Bonasera, "Lyapunov exponents in unstable systems," *Physical Review E - Statistical Physics, Plasmas, Fluids, and Related Interdisciplinary Topics*, vol. 60, pp. 444–448, jul 1999.

[120] W. Nan, W. Xi-Zhen, L. Zhu-Xia, W. Ning, Z. Yi-Zhong, and S. Xiu-Quan, "Behavior of the Lyapunov Exponent and Phase Transition in Nuclei," *Chinese Physics Letters*, vol. 17, no. 10, p. 711, 2000.

[121] M. Foroutan, A. Hossein Jalili, and Z. Nikouei, " Determination of the Maximal Lyapunov Exponent through the Effective Potential Energy: Exact Phase Transition Temperature of Few Particle System CF 4 ," *Journal of the Physical Society of Japan*, vol. 78, p. 124003, dec 2009.

[122] S. Blundell and K. M. Blundell, *Concepts in thermal physics*. Oxford University Press, 2010.

[123] Y. Zhang, A. Otani, and E. J. Maginn, "Reliable Viscosity Calculation from Equilibrium Molecular Dynamics Simulations: A Time Decomposition Method," *Journal of Chemical Theory and Computation*, vol. 11, pp. 3537–3546, aug 2015.

[124] I.-C. Yeh and H. Gerhard, "System-Size Dependence of Diffusion Coefficients and Viscosities from Molecular Dynamics Simulations with Periodic Boundary Conditions," *Journal of Physical Chemistry B*, vol. 108, pp. 15873–15879, oct 2004.

[125] E. H. Abramson, "Melting curves of argon and methane," *http://dx.doi.org/10.1080/08957959.2011.629617*, vol. 31, pp. 549–554, dec 2011.

[126] I. H. Bell, R. Messerly, M. Thol, L. Costigliola, and J. C. Dyre, "Modified Entropy Scaling of the Transport Properties of the Lennard-Jones Fluid," *The Journal of Physical Chemistry B*, vol. 123, pp. 6345–6363, jun 2019.

[127] B. Jakobsen, T. Hecksher, T. Christensen, N. B. Olsen, J. C. Dyre, and K. Niss, "Communication: Identical temperature dependence of the time scales of several linear-response functions of two glass-forming liquids," *Journal of Chemical Physics*, vol. 136, p. 081102, feb 2012.

[128] T. Iwashita, D. M. Nicholson, and T. Egami, "Elementary excitations and crossover phenomenon in liquids," *Physical Review Letters*, vol. 110, p. 205504, may 2013.

[129] R. Zwanzig and R. D. Mountain, "High-frequency elastic moduli of simple fluids," *The Journal of Chemical Physics*, vol. 43, pp. 4464–4471, dec 1965.

[130] A. Zaccone, "Relaxation and vibrational properties in metal alloys and other disordered systems," *Journal of Physics Condensed Matter*, vol. 32, p. 203001, may 2020.

[131] S. Hosokawa, M. Inui, Y. Kajihara, K. Matsuda, T. Ichitsubo, W. C. Pilgrim, H. Sinn, L. E. González, D. J. González, S. Tsutsui, and A. Q. Baron, "Transverse acoustic excitations in liquid Ga," *Physical Review Letters*, vol. 102, p. 105502, mar 2009.

[132] S. Hosokawa, S. Munejiri, M. Inui, Y. Kajihara, W. C. Pilgrim, Y. Ohmasa, S. Tsutsui, A. Q. Baron, F. Shimojo, and K. Hoshino, "Transverse excitations in liquid Sn," *Journal of Physics Condensed Matter*, vol. 25, p. 112101, mar 2013.

[133] S. Hosokawa, M. Inui, Y. Kajihara, S. Tsutsui, and A. Q. Baron, "Transverse excitations in liquid Fe, Cu and Zn," in *Journal of Physics Condensed Matter*, vol. 27, p. 194104, Institute of Physics Publishing, may 2015.

[134] A. Jain and A. J. H. McGaughey, "Thermal transport by phonons and electrons in aluminum, silver, and gold from first principles," *Physical Review B*, vol. 93, p. 081206, feb 2016.

[135] B. Rufflé, G. Guimbretière, E. Courtens, R. Vacher, and G. Monaco, "Glass-Specific Behavior in the Damping of Acousticlike Vibrations," *Physical Review Letters*, vol. 96, p. 045502, jan 2006.

[136] K. Trachenko and V. V. Brazhkin, "Minimal quantum viscosity from fundamental physical constants," *Science Advances*, vol. 6, p. eaba3747, apr 2020.

[137] Y. D. Fomin, V. N. Ryzhov, E. N. Tsiok, J. E. Proctor, C. Prescher, V. B. Prakapenka, K. Trachenko, and V. V. Brazhkin, "Dynamics, thermodynamics and structure of liquids and supercritical fluids: Crossover at the Frenkel line," *Journal of Physics Condensed Matter*, vol. 30, p. 134003, mar 2018.

[138] N. P. Kryuchkov, L. A. Mistryukova, V. V. Brazhkin, and S. O. Yurchenko, "Excitation spectra in fluids: How to analyze them properly," *Scientific Reports*, vol. 9, p. 10483, dec 2019.

[139] T. J. Yoon, M. Y. Ha, E. A. Lazar, W. B. Lee, and Y. W. Lee, "Topological Characterization of Rigid-Nonrigid Transition across the Frenkel Line," *Journal of Physical Chemistry Letters*, vol. 9, pp. 6524–6528, nov 2018.

[140] E. Braun, S. M. Moosavi, and B. Smit, "Anomalous Effects of Velocity Rescaling Algorithms: The Flying Ice Cube Effect Revisited," *Journal of Chemical Theory and Computation*, vol. 14, pp. 5262–5272, oct 2018.

[141] C. N. Yang and T. D. Lee, "Statistical Theory of Equations of State and Phase Transitions. I. Theory of Condensation," *Physical Review*, vol. 87, p. 404, aug 1952.

[142] A. Rahman, "Correlations in the motion of atoms in liquid argon," *Physical Review*, vol. 136, p. A405, oct 1964.

[143] Y. Hiwatari, H. Matsuda, T. Ogawa, N. Ogita, and A. Ueda, "Molecular Dynamics Studies on the Soft-Core Model," *Progress of Theoretical Physics*, vol. 52, pp. 1105–1123, oct 1974.

[144] H. Endo, Y. Endo, and N. Ogita, "Resolution of the velocity autocorrelation function in fluids at various density states," *The Journal of Chemical Physics*, vol. 77, pp. 5184–5190, nov 1982.